

# A Precision Measurement of Neutral Pion Lifetime

by

Yang Zhang

Department of Physics  
Duke University

Date: \_\_\_\_\_

Approved:

\_\_\_\_\_  
Haiyan Gao, Supervisor

\_\_\_\_\_  
Albert M Chang

\_\_\_\_\_  
Alfred T Goshaw

\_\_\_\_\_  
Thomas C Mehen

\_\_\_\_\_  
Maiken Mikkelsen

Dissertation submitted in partial fulfillment of the requirements for the degree of  
Doctor of Philosophy in the Department of Physics  
in the Graduate School of Duke University  
2018

# ABSTRACT

## A Precision Measurement of Neutral Pion Lifetime

by

Yang Zhang

Department of Physics  
Duke University

Date: \_\_\_\_\_

Approved:

\_\_\_\_\_  
Haiyan Gao, Supervisor

\_\_\_\_\_  
Albert M Chang

\_\_\_\_\_  
Alfred T Goshaw

\_\_\_\_\_  
Thomas C Mehen

\_\_\_\_\_  
Maiken Mikkelsen

An abstract of a dissertation submitted in partial fulfillment of the requirements for  
the degree of Doctor of Philosophy in the Department of Physics  
in the Graduate School of Duke University  
2018



Copyright © 2018 by Yang Zhang  
All rights reserved except the rights granted by the  
Creative Commons Attribution-Noncommercial Licence

# Abstract

The neutral pion decays via chiral anomaly and this process historically led to the discovery of the chiral anomaly. The  $\pi^0$  decay width is among the most precise predictions of quantum chromodynamics (QCD) at low energy. However, the current experimental results are not commensurate with theoretical predictions. The Particle Data Group (PDG) average of the experimental results is  $7.63 \pm 0.16$  eV, which is consistent with the chiral anomaly prediction ( $7.725 \pm 0.044$  eV). Recent theoretical calculations based on the sum rule and chiral perturbation theories (ChPT) show an increase of 3.0%-4.5% to the chiral anomaly prediction with 1% precision. As a result, a precise measurement of the neutral pion decay width would be one of the most stringent tests of low energy QCD. PrimEx-II experiment measured the neutral pion decay width via the Primakoff effect using two targets, silicon and  $^{12}\text{C}$ . The  $\pi^0$  decay width was extracted by fitting the measured cross sections using recently updated theoretical models for the process. The resulting total  $\pi^0$  decay width is  $7.82 \pm 0.05(\text{stat}) \pm 0.10(\text{syst})$  eV. With a total uncertainty of 1.8%, this result is the most precise experimental estimation. The PrimEx-II result lies within  $0.8 \sigma$  above the chiral anomaly prediction, one  $\sigma$  below the sum rule prediction, and  $1.8 \sigma$  below the ChPT calculations. This result is in better agreement with the chiral anomaly prediction.

To my wife Min Huang

# Contents

<b>Abstract</b>	<b>iv</b>
<b>List of Tables</b>	<b>x</b>
<b>List of Figures</b>	<b>xi</b>
<b>Acknowledgements</b>	<b>xv</b>
<b>1 Introduction and Physics Motivation</b>	<b>1</b>
1.1 Introduction . . . . .	1
1.2 Physics Motivation . . . . .	5
<b>2 Previous Experiments and Results</b>	<b>13</b>
2.1 Overview . . . . .	13
2.2 The Primakoff Method . . . . .	13
2.3 Direct Method . . . . .	16
2.4 Collider Measurement . . . . .	17
<b>3 The PrimEx Experiment</b>	<b>20</b>
3.1 Overview . . . . .	20
3.2 Thomas Jefferson National Accelerator Facility . . . . .	20
3.3 Experimental Setup . . . . .	21
3.4 Hall B Photon Tagger . . . . .	23
3.5 Targets Thickness Measurement . . . . .	25
3.6 The Total Absorption Counter and Absolute Photon Flux Tagging Ratio	27

3.7	The Pair Spectrometer and the Relative Flux Tagging Ratio . . . . .	29
3.8	Charged Particle Veto Counters . . . . .	32
3.9	PrimEx Hybrid Calorimeter (HYCAL) and “Snake Scan” Calibration Runs . . . . .	32
3.10	Beam Position Monitors, Superharp Scans and The Photon Beam Monitor . . . . .	38
3.11	A summary of PrimEx-II Improvement . . . . .	42
<b>4</b>	<b>Data Analysis</b>	<b>45</b>
4.1	Overview . . . . .	45
4.2	Data Source and Run Numbers Used . . . . .	47
4.2.1	Event Preselection: Skim Files . . . . .	47
4.2.2	Single Arm Compton Scattering Analysis . . . . .	48
4.3	Detector Software Calibration and Alignment . . . . .	50
4.3.1	Tagger TDC Alignment . . . . .	50
4.3.2	The HYCAL Cluster Reconstruction Algorithm . . . . .	52
4.3.3	HYCAL Energy Software Calibration . . . . .	53
4.3.4	HYCAL Coordinate Alignment . . . . .	57
4.3.5	HYCAL Trigger Timing Alignment . . . . .	60
4.4	Tagged Photon Flux Determination . . . . .	61
4.4.1	Tagged Electron Accounting . . . . .	61
4.4.2	Beam Trip Accounting . . . . .	65
4.4.3	Summary . . . . .	66
4.5	Event Selection . . . . .	67
4.6	Yield Extraction . . . . .	70
4.6.1	The “Hybrid Mass” . . . . .	70
4.6.2	Accidental Sidebands Subtraction and Tdiff Cut efficiency . .	73

4.6.3	The “Hybrid Mass” Fitting and the $\pi^0$ Yields Determination .	75
4.6.4	“Best Tdiff” Correction . . . . .	77
4.6.5	Extracted yields of $\pi^0 \rightarrow \gamma\gamma$ coherent photoproduction . . . .	79
4.7	Theoretical Description of Forward Photoproduction of $\pi^0$ . . . . .	80
4.8	Experimental Acceptance and Angular Resolution . . . . .	82
4.9	$\pi^0$ Yields Fitting . . . . .	85
<b>5</b>	<b>Results and Conclusions</b>	<b>92</b>
5.1	Branching Ratio . . . . .	92
5.2	Uncertainties from Target Measurement . . . . .	93
5.3	Uncertainties from Yield Extraction . . . . .	93
5.3.1	Uncertainties from Single $\gamma$ Energy Cut . . . . .	93
5.3.2	Uncertainties from $\pi^0$ Energy Cut . . . . .	93
5.3.3	Decay Width Sensitivity to Tdiff Cut . . . . .	95
5.3.4	“Hybrid Mass” Fitting Uncertainties . . . . .	96
5.3.5	Comparison of Yields with Different Binnings . . . . .	98
5.3.6	Realistic Monte Carlo . . . . .	100
5.4	Decay Width Sensitivity to $\omega$ background subtraction . . . . .	101
5.5	Decay Width Sensitivity to $\pi^0$ Angular Resolution . . . . .	102
5.6	Uncertainties from HYCAL Acceptance . . . . .	102
5.6.1	Decay Width Sensitivity to HYCAL Coordinates Misalignment	103
5.6.2	Decay Width Sensitivity to HYCAL $z$ Position . . . . .	105
5.7	Systematic Uncertainties Due to Photon Beam . . . . .	107
5.7.1	Decay Width Sensitivity to the Photon Beam Energy . . . . .	108
5.7.2	Decay Width Sensitivity to the Beam Width . . . . .	108
5.7.3	Decay Width Sensitivity to Beam Direction . . . . .	108

5.8	Different Nuclear Density Models . . . . .	109
5.9	Systematic Uncertainties . . . . .	112
5.10	$\pi^0$ Decay Width . . . . .	112
5.11	Summary and Outlook . . . . .	113
	<b>Bibliography</b>	<b>116</b>
	<b>Biography</b>	<b>119</b>

# List of Tables

3.1	Target properties of PRIMEX-II . . . . .	27
3.2	List of analyzed TAC runs and their parameters [25] . . . . .	30
4.1	The constant factors used in the fitting to the $\pi^0$ photoproduction yields. . . . .	85
4.2	$\pi^0$ decay width obtained from silicon and carbon targets . . . . .	86
5.1	$\pi^0$ decay width obtained from silicon and carbon targets with different angular bins. . . . .	100
5.2	Systematic uncertainties of $\pi^0$ decay width due to uncertainties from the $\omega$ background . . . . .	101
5.3	Systematic uncertainties of $\pi^0$ decay width due to HYCAL misalignment	105
5.4	Systematic uncertainties of $\pi^0$ decay width due to the uncertainty of the beam direction . . . . .	109
5.5	Uncertainties of $\pi^0$ decay width. . . . .	112
5.6	$\pi^0$ decay width obtained from silicon and carbon targets . . . . .	113



# List of Figures

1.1	Strong interaction coupling constant . . . . .	2
1.2	Experimental measurements of $\pi^0$ decay width . . . . .	4
1.3	The diagram of $\pi^0$ decay through chiral anomaly . . . . .	6
1.4	The triangle Feynman diagrams . . . . .	6
1.5	The theoretical predictions of $\pi^0$ decay width . . . . .	11
1.6	Experimental knowledge and theoretical predictions of $\pi^0$ decay width	12
2.1	Feynman diagrams of Primakoff process and $\pi^0 \rightarrow \gamma\gamma$ decay . . . . .	14
2.2	A schematic figure for the $\pi^0$ photoproduction on a Carbon targets with elastic cut . . . . .	15
2.3	Schematic experimental setup for the direct method . . . . .	18
2.4	Spectra of pions produced at $0^\circ$ by 450 GeV/c incident protons at CERN SPS . . . . .	19
3.1	The Thomas Jefferson National Accelerator Facility . . . . .	21
3.2	PrimEx-II experimental setup . . . . .	22
3.3	Overall geometry of the Hall B photon tagger . . . . .	24
3.4	Polished surface of a Silicon wafer used in the PRIMEX II experiment	26
3.5	A schematic figure showing the PrimEx-II carbon target . . . . .	27
3.6	Absolute tagging ratio and beam current . . . . .	31
3.7	Vertical veto counters . . . . .	33
3.8	Virtual map of HYCAL with corresponding number of each crystal .	34

3.9	A photo of the HYCAL installed in the test lab . . . . .	35
3.10	A photo of the lead glass crystal and PbWO <sub>4</sub> crystal used in the PrimEx experiment . . . . .	36
3.11	A PbWO <sub>4</sub> crystal module sample . . . . .	36
3.12	The temperature stability of the PbWO <sub>4</sub> during a 12 hour period . .	37
3.13	The HYCAL and its chassis sitting on the HYCAL Transporter . . .	38
3.14	The calibration snake scan scheme . . . . .	39
3.15	The HYCAL energy resolution . . . . .	39
3.16	Photon beam profile . . . . .	40
3.17	Electron beam profile . . . . .	41
3.18	Photon position beam monitor . . . . .	41
3.19	Beam current vs. event number . . . . .	42
3.20	Photon beam X position . . . . .	43
3.21	Photon beam Y position . . . . .	44
4.1	Elasticity for single arm compton events . . . . .	50
4.2	Single arm compton events over time . . . . .	51
4.3	HYCAL clusters generated from Monte Carlo events by the “island” algorithm . . . . .	54
4.4	HYCAL gain factor calibration . . . . .	55
4.5	Calibration constant vs. module Id for both crystal and glass for the second snake run. . . . .	55
4.6	$\gamma\gamma$ invariant mass spectrum on a single HYCAL module . . . . .	57
4.7	The $m_{\gamma\gamma}$ before and after the iterative calibration procedure . . . . .	58
4.8	Calibration constant vs. module number . . . . .	59
4.9	Calibration constant distribution for all modules . . . . .	59
4.10	The distribution of $\theta_x$ and $\theta_y$ for one run group . . . . .	60

4.11	Number of events as a function of Tdiff for the silicon target obtained by the “best Tdiff” method . . . . .	62
4.12	HYCAL ADC signal speed . . . . .	63
4.13	Tdiff with HYCAL timing alignment . . . . .	64
4.14	Timing spectrum for a single T-channel taken with clock triggers . . .	65
4.15	A typical distribution of the $R_{live-time}$ in a run . . . . .	67
4.16	Tagged photon multiplicity for the silicon target . . . . .	68
4.17	$m_{\gamma\gamma}$ with “best Tdiff” and “all Tdiff” . . . . .	69
4.18	$\gamma\gamma$ invariant mass and elasticity . . . . .	71
4.19	Elasticity vs. $\frac{m_{\gamma\gamma}}{m_{\pi^0}}$ . . . . .	72
4.20	The “hybrid mass” distribution for the silicon target in angular bin .	74
4.21	Accidental side band subtraction . . . . .	75
4.22	Hybrid mass signal shape from Monte Carlo . . . . .	76
4.23	Six fitting samples of the “hybrid mass” distribution for the silicon target . . . . .	78
4.24	The “hybrid mass” distributions of the $\pi^0$ candidates with the second “best tdiff” . . . . .	80
4.25	The $\pi^0 \rightarrow \gamma\gamma$ yields . . . . .	87
4.26	The $\pi^0 \rightarrow \gamma\gamma$ yield for the silicon target with all HYCAL acceptance	88
4.27	Acceptance and resolution matrix . . . . .	89
4.28	The HYCAL $\text{PbWO}_4$ acceptance . . . . .	90
4.29	$\pi^0$ yields fitting . . . . .	91
5.1	Single $\gamma$ energy cut systematic uncertainty . . . . .	94
5.2	$\pi^0$ energy cut systematic uncertainty . . . . .	95
5.3	The efficiency of Tdiff cut . . . . .	96
5.4	$\Gamma(\pi^0)$ changes based on different Tdiff cuts . . . . .	97

5.5	The $\Gamma(\pi^0)$ s calculated using different signal extraction methods for the silicon target . . . . .	98
5.6	The $\Gamma(\pi^0)$ s calculated using different signal extraction methods for the carbon target . . . . .	99
5.7	$\pi^0$ yield extracted with $0.015^\circ$ angular bin for silicon. . . . .	100
5.8	$\pi^0$ yield extracted with $0.02^\circ$ angular bin for silicon. . . . .	101
5.9	$\pi^0$ yield extracted with $0.03^\circ$ angular bin for silicon. . . . .	102
5.10	$\pi^0$ yield extracted with $0.015^\circ$ angular bin for carbon. . . . .	103
5.11	$\pi^0$ yield extracted with $0.02^\circ$ angular bin for carbon. . . . .	104
5.12	$\pi^0$ yield extracted with $0.03^\circ$ angular bin for carbon. . . . .	105
5.13	$\pi^0$ decay widths from realistic M.C. . . . .	106
5.14	$\Gamma(\pi^0)$ as a function of HYCAL misalignment . . . . .	106
5.15	The $\Gamma(\pi^0)$ as a function of the distance of HYCAL to the target center	107
5.17	Goodness of fits and the decay width's using 3-parameter Fermi nuclear density model . . . . .	110
5.18	Goodness of fits and the decay width's using Fermi-Bessel nuclear density model . . . . .	111
5.16	$\Gamma(\pi^0)$ as a function of beam angle . . . . .	114
5.19	$\pi^0$ decay widths . . . . .	115

# Acknowledgements

It has been a long journey being a graduate student at Duke and pursuing the PhD degree. At this moment, I would like to express my sincere appreciation to a lot of people who helped me in these years.

First and foremost, my deepest gratitude goes to my advisor Haiyan Gao for her support and guidance. I appreciate and admire her efforts to communicate with students closely. And after the initial guidance, she always let me independently think and conduct the research work, and of course gave advice whenever needed. This helped me grow with critical thinking and problem solving abilities, which would always benefit me. I'm also thankful for her help in correcting the draft of this thesis.

I'd like to thank my collaborator Ilya Larin at Jefferson Lab. In the third year, I moved to Jefferson Lab and joined the PrimEx-II collaboration. Ilya is an experienced researcher who participated in the preparation, data taking and data analysis of both PrimEx-I and PrimEx-II. His knowledge and enthusiasm on nuclear physics are amazing. He helped me get started with the data analysis and was always there for questions. His rigorous attitude towards the analysis results has been an excellent training to me.

The PrimEx-II collaboration has been a great group to work with. I'd like to thank the spokespeople Ashot Gasparian, Rory Miskimen, Dan Dale, Mark Ito, Liping Gan, for their scientific vision and efforts to realize this experiment. I learned a lot from their professional examples. Thanks to Professor Aron Bernstein, who

guided me through many difficult problems. Thanks to, Pawel Ambrozewicz, Jing Feng, Sergey Gevorgyan, David Lawrence, Lingling Ma, Victor Tarasov and Li Ye, whom I worked with on the the analysis on a daily basis. They inspired and helped me through countless discussions and conversations.

In the fourth year, I moved to UVa briefly to work on the GEM production for the PRad experiment with the UVa GEM team. I am grateful to Professor Nilanga Liyanage for introducing to me the field of gaseous detectors, and guiding me through the GEM detector production procedure.

I am lucky to be a member of the medium energy group at Duke. When I first entered this field, Wangzhi Zheng guided and worked with me on the first project. I am grateful to his help of introducing the physics and analysis skills to me, and answering my questions patiently. I learned a lot from him. I want to acknowledge all the current and past members of the MEP group who had helped and inspired me. I also want to thank all my friends at Duke and Jefferson Lab for the joyous time we shared.

Last but not least, I'd like to thank my parents, whose unconditional love and constant support could never be matched with any word. I also want to thank my wife Min Huang for being my best friend and love of my life, and for letting me become a better me.

# Introduction and Physics Motivation

## 1.1 Introduction

The strong interaction is responsible for 99% of all visible matter in the universe. Quantum Chromodynamics (QCD), which treats quarks and gluons as the fundamental degrees of freedom, is regarded as the accepted description of strong interactions. The gluons carry color charges and work as the mediators of the strong force, and also interact with themselves. This special feature leads to two important aspects of QCD: asymptotic freedom and color confinement.

Color confinement describes the phenomenon that quarks and gluons are bound into colorless hadrons and can not be observed directly. The asymptotic freedom describes the feature that the coupling between two color objects is weaker at higher energy (shorter distance), and stronger at lower energy (longer distance). Fig. 1.1 shows the strong interaction coupling constant  $\alpha_s$  as a function of the 4-momentum transfer  $Q$ . The  $\alpha_s$  approaches zero at large  $Q$ , where quarks/gluons behave like free particles. In this circumstance, perturbative calculations can be used to predict experimental observables. However, at low energy, perturbative calculations are not

applicable due to the fact that  $\alpha_s$  is large and the relevant degrees of freedom are color neutral hadrons, not quarks and gluons. Lattice calculations and Chiral Perturbation Theory (ChPT) are two important theoretical methods used in the low energy QCD. The  $\pi^0$  decay width is particularly important since it is arguably the most precisely calculated quantity in low energy QCD.

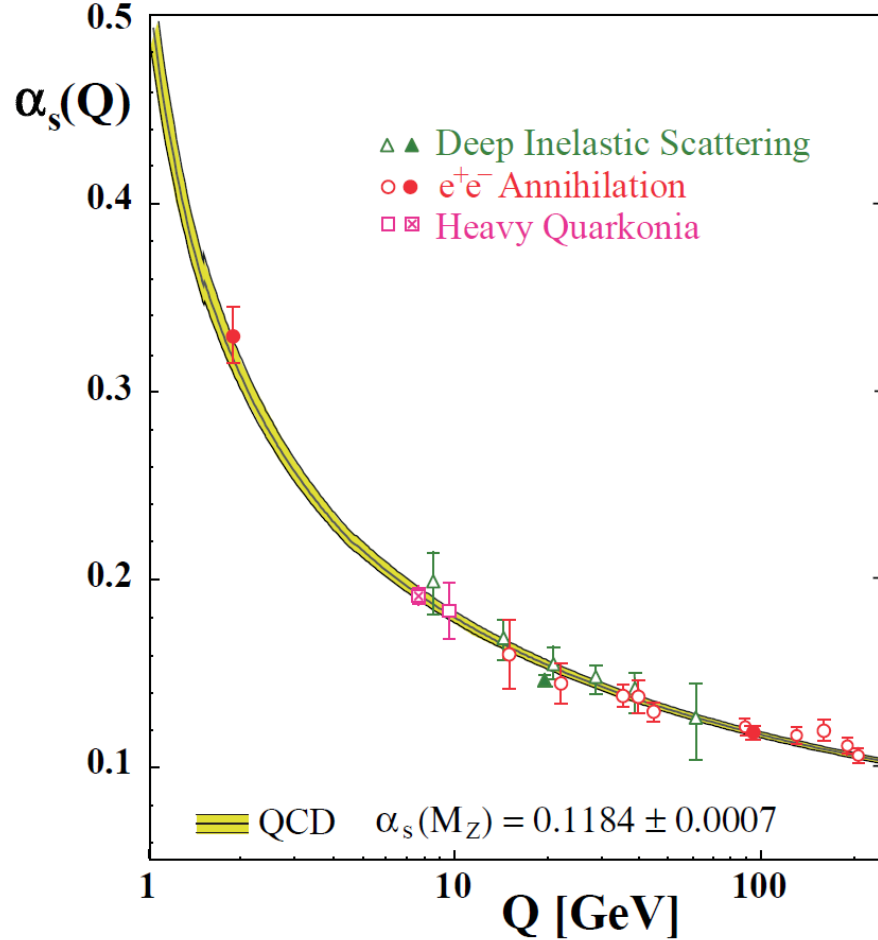


FIGURE 1.1: The strong interaction coupling constant, measured from Deep Inelastic Scattering,  $e^+e^-$  annihilation, and heavy Quarkonia, is plotted as a function of the 4-momentum transfer  $Q$ .

The  $\pi^0 \rightarrow \gamma\gamma$  decay proceeds primarily via the chiral anomaly, which is another important aspect of QCD. An anomaly occurs when the symmetry of a theory's classical Lagrangian fails to be the symmetry of the full quantum theory. The chiral



symmetry exists in the classical Lagrangian of QCD in the chiral limit (vanishing light quark masses). If one considers the light quarks, u and d, the massless approximation is appropriate. The chiral symmetry is spontaneously broken in the quantum field theory. The  $\pi^0$  decay width is predicted to be  $7.725 \pm 0.044$  eV via the chiral anomaly in the chiral limit at the leading order (LO). Recent theoretical calculations in chiral perturbation theory (ChPT) at next-to-leading order and next-to-next-leading order (NLO and NNLO) predict a small, 4.5% increase to the decay width predicted by the chiral anomaly [1, 2, 3]. All these calculations are at 1% level precision. However, the experimental situation on the  $\pi^0$  decay width is very different. To improve the experimental situation, PrimEx-I [4] and PrimEx-II experiments were carried out in 2004 and 2010, which will be discussed in details in the following chapters. Before PrimEx-I, the average experimental value of the  $\pi^0$  decay width given by the Particle Data Group (PDG) was  $7.74 \pm 0.55$  eV [5]. This value was the average of four experiments with much larger dispersions among both the decay widths and their quoted experimental uncertainties. The most precise measurement prior to PrimEx-I was made by Atherton *et al* with a 3.1% total uncertainty [6]. Clearly, an experiment with a better precision is needed. The  $\pi^0$  decay width measured by PrimEx-I was  $7.82 \pm 0.14 \pm 0.17$  eV, with a total uncertainty of 2.8% [4]. The PrimEx-I result improved the PDG average by a factor of 1.5. The current experimental average from the PDG is  $7.63 \pm 0.16$  eV [7]. It is the average of the five experimental results. Four of them are dedicated measurements of the  $\pi^0$  decay width. These are the 1974 Cornell Primakoff measurement [8] giving the  $\pi^0$  decay width of  $8.02 \pm 0.42$  eV, the 1985 CERN direct measurement of the decay width at  $7.34 \pm 0.18 \pm 0.11$  eV [6], the 1988 DESY  $e^+e^-$  experiment giving the decay width of  $7.7 \pm 0.5 \pm 0.5$  eV [9], and the PrimEx-I experiment [4]. The last experiment [10] measured the pion weak form factor, and the  $\pi^0$  decay width was obtained via the conserved-vector-current relation between the  $\pi^0$  decay width and the vector form factor  $F_V$ . The quoted result

is  $7.74 \pm 1.02$  eV. I will not discuss this experiment due to its large uncertainties. The results of the other four experiments together with the theoretical predictions are summarized in Fig. 1.2.

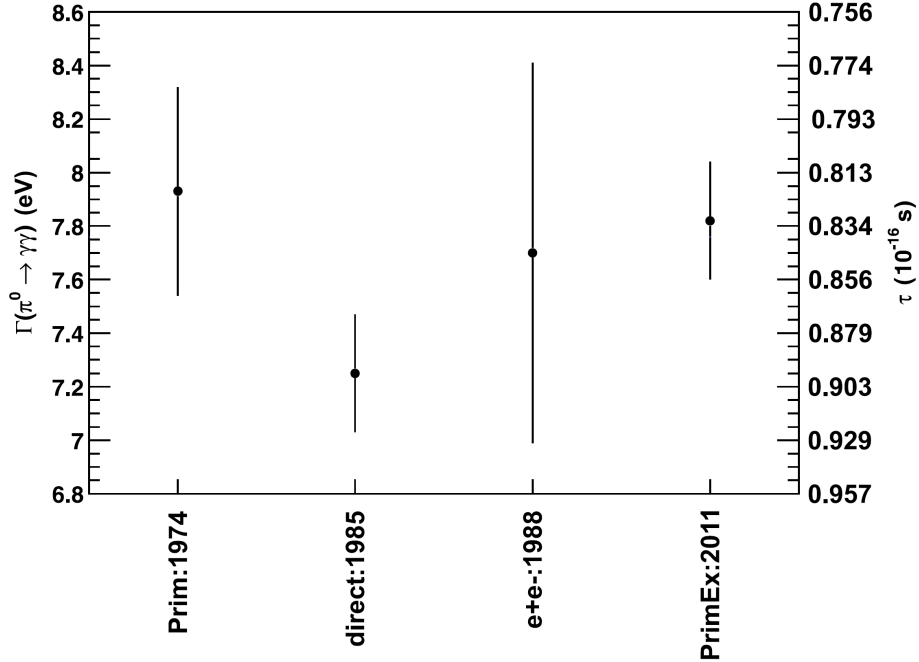


FIGURE 1.2: Experimental measurements of  $\pi^0$  decay width. The four experiments are the 1974 Cornell Primakoff measurement [8], the 1985 CERN direct measurement [6], the 1988 DESY  $e^+e^-$  experiment [9], and the PrimEx-I experiment [4].

In summary, three of the four experiments mentioned above are in agreement with the LO anomaly prediction and the higher order chiral perturbation theory calculations. However, they don't have sufficient accuracy to demonstrate the 4.5% increase predicted by the recent theoretical calculations. In addition, the difference between the results of the two most accurate experiments, the 1985 direct measurement at CERN [6], and the PrimEx-I experiment [4] is 0.57 eV, which is about 7.5%. Clearly, although the experimental situation was improved after PrimEx-I, another experiment with higher accuracy is still needed.

PrimEx-II is another Primakoff type of measurement similar to PrimEx-I. The

Primakoff effect is particularly advantageous because the  $\pi^0$  decay width is proportional to the Primakoff cross section. The energy and timing of the incoming photon is tagged by the a photon tagging facility. The  $\pi^0$  is created by the interaction between this real photon and a virtual photon in the target. It then quickly decays into two  $\gamma$ 's, which were detected by a hybrid calorimeter (HYCAL). The kinematics of the  $\pi^0$  can be reconstructed and a differential cross section can be extracted. The goal of PrimEx-II is to measure the decay width to a precision of less than 2.0%.

## 1.2 Physics Motivation

The two-photon decay mode of  $\pi^0$  proceeds through chiral anomaly, which is demonstrated in Fig 1.3. This process historically led to the discovery of chiral anomaly and also provides a test of it. The chiral anomaly is of pure quantum mechanical origin. In order to demonstrate this, consider the Lagrangian of simple massless spinor field carrying charge  $e$  coupled to the electromagnetic field:

$$\mathcal{L} = \bar{\psi}(i\not{\partial} - e\not{A})\psi - \frac{1}{4}F_{\mu\nu}F^{\mu\nu}. \quad (1.1)$$

The Lagrangian is invariant under transformations  $\psi \rightarrow e^{i\theta}\psi$  and  $\bar{\psi} \rightarrow e^{i\theta}\bar{\psi}$ , leading to conserved vector currents  $J^\mu = \bar{\psi}\gamma^\mu\psi$  and the conserved axial current  $J_5^\mu = \bar{\psi}\gamma^\mu\gamma^5\psi$ , respectively.

Now in quantum theory, consider the amplitude  $\langle 0|T J_5^\lambda(0)J^\mu(x_1)J^\nu(x_2)|0\rangle$ . Its Fourier transform is given by two “triangle” diagrams in Fig. 1.4, which gives

$$\Delta^{\lambda\mu\nu}(k_1, k_2) = (-1)i^3 \int \frac{d^4p}{(2\pi)^4} \text{tr}(\gamma^\lambda\gamma^5 \frac{1}{\not{p} - \not{q}} \gamma^\nu \frac{1}{\not{p} - \not{k}_1} \gamma^\mu \frac{1}{\not{p}} + \gamma^\lambda\gamma^5 \frac{1}{\not{p} - \not{q}} \gamma^\mu \frac{1}{\not{p} - \not{k}_2} \gamma^\nu \frac{1}{\not{p}}), \quad (1.2)$$

where  $q = k_1 + k_2$  is the momentum carried by the axial current. Classically the two

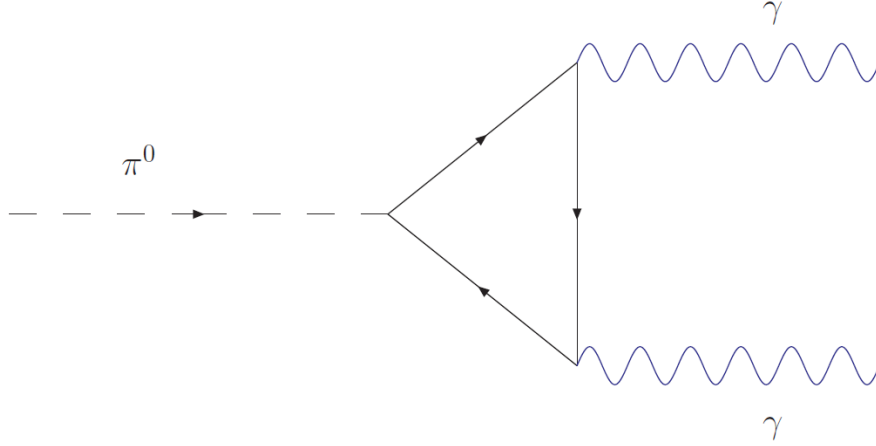


FIGURE 1.3: The diagram of  $\pi^0$  decay through chiral anomaly.

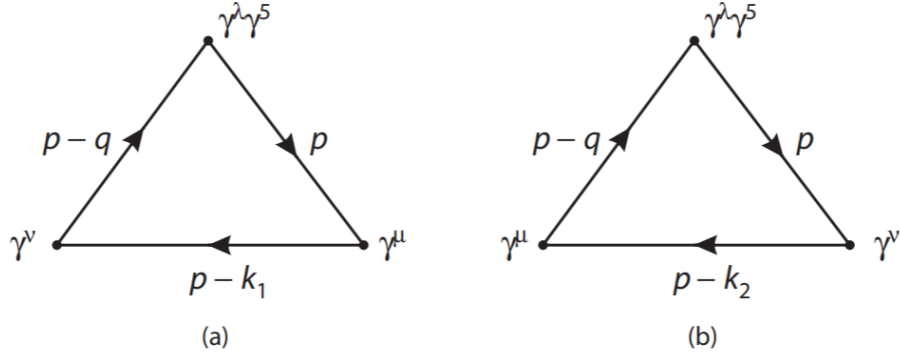


FIGURE 1.4: The triangle Feynman diagrams for the amplitude  $\langle 0 | T J_5^\lambda(0) J^\mu(x_1) J^\nu(x_2) | 0 \rangle$ .

aforementioned symmetries imply  $\partial_\mu J^\mu = 0$  and  $\partial_\mu J_5^\mu = 0$ , or  $k_{1\mu,2\nu} \Delta^{\lambda\mu\nu} = 0$  and  $q_\lambda \Delta^{\lambda\mu\nu} = 0$ .

In order to validate these relations in the quantum theory, one will need to calculate the integral in equation 1.2. Contracting equation 1.2 with  $k_{1\mu}$ , and replacing  $k'_1$  with  $\not{p} - (\not{p} - \not{k}'_1)$  in the first term, with  $(\not{p} - \not{k}'_2) - (\not{p} - \not{q})$  in the second term, one obtains:

$$k_{1\mu} \Delta^{\lambda\mu\nu}(k_1, k_2) = i \int \frac{d^4 p}{(2\pi)^4} \text{tr} \left( \gamma^\lambda \gamma^5 \frac{1}{\not{p} - \not{q}} \gamma^\nu \frac{1}{\not{p} - \not{k}'_1} - \gamma^\lambda \gamma^5 \frac{1}{\not{p} - \not{k}'_2} \gamma^\nu \frac{1}{\not{p}} \right). \quad (1.3)$$

If one writes the integrand in the first term in Eq.( 1.3) as  $f(p)$ , then the second term can be written as  $f(p + k_1)$ . Using Taylor's theorem:

$$\int \frac{d^4 p}{(2\pi)^4} f(p + k_1) = \int \frac{d^4 p}{(2\pi)^4} (f(p) + k_1^\mu \partial_\mu f(p)). \quad (1.4)$$

Using Gauss's theorem, one has:

$$k_{1\mu} \Delta^{\lambda\mu\nu}(k_1, k_2) = -\frac{i}{(2\pi)^4} \lim_{p \rightarrow \infty} i k_1^\mu \frac{p_\mu}{p} f(p) S_3, \quad (1.5)$$

where  $S_3 = 2\pi^2 p^3$  is the area of the 4-dimensional spherical surface. Plugging

$$\begin{aligned} f(p) &= \text{tr}(\gamma^\lambda \gamma^5 \frac{1}{\not{p} - \not{q}} \gamma^\nu \frac{1}{\not{p} - \not{k}_1}) \\ &= \frac{\gamma^5 (\not{p} - \not{q}) \gamma^\nu (\not{p} - \not{k}_1) \gamma^\lambda}{(p - q)^2 (p - k_1)^2} \\ &= \frac{4i\epsilon^{\tau\nu\sigma\lambda} (q_\tau p_\sigma + q_\tau k_{1\sigma})}{(p - q)^2 (p - k_1)^2}, \end{aligned} \quad (1.6)$$

into equation 1.4, one obtains:

$$\begin{aligned} k_{1\mu} \Delta^{\lambda\mu\nu}(k_1, k_2) &= \frac{i}{(2\pi)^4} \lim_{p \rightarrow \infty} i(-k_1)^\mu \frac{p_\mu}{p} \frac{4i\epsilon^{\tau\nu\sigma\lambda} q_\tau p_\sigma}{p^4} (2\pi^2 p^3) \\ &= \frac{i}{8\pi^2} \epsilon^{\tau\nu\sigma\lambda} k_{1\tau} k_{2\sigma}. \end{aligned} \quad (1.7)$$

Similarly, one finds  $k_{2\nu} \Delta^{\lambda\mu\nu}(k_1, k_2) = -\frac{i}{8\pi^2} \epsilon^{\tau\nu\sigma\lambda} k_{1\tau} k_{2\sigma}$ , and  $q_\lambda \Delta^{\lambda\mu\nu}(k_1, k_2) = \frac{i}{4\pi^2} \epsilon^{\mu\nu\lambda\sigma} k_{1\lambda} k_{2\sigma}$ . The violation of the vector current conservation is disastrous and would have serious consequences for photon interactions. The problem arises from the linear divergence of integration 1.2. As a result, integration 1.2 is not well defined. To solve this issue and restore current vector reservation, one can alter the integration 1.2 via shifting the integration variable by an 4-vector  $a$  so that  $k_{1\mu, 2\nu} \Delta^{\lambda\mu\nu}(a, k_1, k_2) = 0$ . First compute the difference  $\Delta^{\lambda\mu\nu}(a, k_1, k_2) - \Delta^{\lambda\mu\nu}(k_1, k_2)$

using similar method above. In this case,

$$\begin{aligned}
f(p) &= \lim_{p \rightarrow \infty} \text{tr}(\gamma^\lambda \gamma^5 \frac{1}{\not{p} - \not{q}} \gamma^\nu \frac{1}{\not{p} - \not{k}_1} \gamma^\mu \frac{1}{\not{p}}) \\
&= \lim_{p \rightarrow \infty} \frac{\text{tr}(\gamma^\lambda \gamma^5 \not{p} \gamma^\nu \not{p} \gamma^\mu \not{p})}{p^6} \\
&= \frac{2p^\mu \text{tr}(\gamma^\lambda \gamma^5 \not{p} \gamma^\nu \not{p}) - p^2 \text{tr}(\gamma^\lambda \gamma^5 \not{p} \gamma^\nu \gamma^\mu)}{p^6} \\
&= \frac{4ip^2 p_\sigma \epsilon^{\sigma\nu\mu\lambda}}{p^6}.
\end{aligned} \tag{1.8}$$

The difference between  $\Delta^{\lambda\mu\nu}(a, k_1, k_2)$  and  $\Delta^{\lambda\mu\nu}(k_1, k_2)$  can be obtained via Gauss's theorem:

$$\Delta^{\lambda\mu\nu}(a, k_1, k_2) - \Delta^{\lambda\mu\nu}(k_1, k_2) = \frac{4i}{8\pi^2} \lim_{p \rightarrow \infty} a^\omega \frac{p_\omega p_\sigma}{p^2} \epsilon^{\sigma\nu\mu\lambda} + \mu, k_1 \leftrightarrow \nu, k_2. \tag{1.9}$$

Since  $k_1$  and  $k_2$  are independent, one can represent the 4-vector  $a$  as  $\alpha(k_1 + k_2) + \beta(k_1 - k_2)$ . Plugging it into equation 1.9, one has:

$$\Delta^{\lambda\mu\nu}(a, k_1, k_2) = \Delta^{\lambda\mu\nu}(k_1, k_2) + \frac{i\beta}{4\pi^2} \epsilon^{\lambda\mu\nu\sigma} (k_1 - k_2)_\sigma. \tag{1.10}$$

In order to make  $k_{1\mu, 2\nu} \Delta^{\lambda\mu\nu}(a, k_1, k_2) = 0$ ,  $\beta = -\frac{1}{2}$ . To calculate  $q_\lambda \Delta^{\lambda\mu\nu}(a, k_1, k_2)$ , one only needs to calculate

$$q_\lambda \Delta^{\lambda\mu\nu}(a, k_1, k_2) = q_\lambda \Delta^{\lambda\mu\nu}(k_1, k_2) + \frac{i}{4\pi^2} \epsilon^{\mu\nu\lambda\sigma} k_{1\lambda} k_{2\sigma}. \tag{1.11}$$

Since  $q_\lambda \Delta^{\lambda\mu\nu}(k_1, k_2) = \frac{i}{4\pi^2} \epsilon^{\mu\nu\lambda\sigma} k_{1\lambda} k_{2\sigma}$ , finally:

$$q_\lambda \Delta^{\lambda\mu\nu}(a, k_1, k_2) = \frac{i}{2\pi^2} \epsilon^{\mu\nu\lambda\sigma} k_{1\lambda} k_{2\sigma}. \tag{1.12}$$

The axial current is not conserved and the chiral symmetry is broken. For more detailed derivation, please refer to [11, 12, 13]. The amplitude  $\langle 0 | T J_5^\lambda(0) J^\mu(x_1) J^\nu(x_2) | 0 \rangle$

can be seen as the matrix element of the axial current between the vacuum and a two-photon state. The matrix element contributes to a process in which a  $\pi^0$  is first created by the axial current and then decays into two photons, and the  $\pi^0$  decay amplitude is directly linked to equation 1.12. The  $\pi^0$  decay amplitude vanishes in chiral limit if one assumes the conservation of the axial current. Since the  $\pi^0$  decays into two photons and  $\pi^0$  mass is very small (chiral limit is “almost” right), historically the  $\pi^0$  decay process provides the first indication of the non-conservation of the axial current. The  $\pi^0$  two-photon decay amplitude predicted by chiral anomaly in the chiral limit assumption is [12]:

$$\frac{e^2}{4\pi^2 F_\pi} \epsilon_{\mu\nu\tau\sigma} k_1^\mu k_2^\nu \epsilon_1^\tau \epsilon_2^{*\sigma}, \quad (1.13)$$

where  $\epsilon_1$  and  $\epsilon_2$  are the photon polarizations, and  $F_\pi = 92.21 \pm 0.02 \pm 0.14$  MeV is the pion decay constant and can be measured via  $\pi^+ \rightarrow \mu^+ \nu_\mu$  [14]. This gives the decay rate:

$$\Gamma(\pi^0 \rightarrow \gamma\gamma) = \frac{\alpha^2 m_\pi^3}{64\pi^3 F_\pi^2}, \quad (1.14)$$

where  $\alpha$  is the fine structure constant, and  $m_\pi$  is the mass of the  $\pi^0$ . The predicted  $\pi^0$  decay width is  $7.76 \pm 0.04$  eV, which is in agreement with the currently accepted value,  $7.74 \pm 0.46$  eV [7].

However, the above prediction is incomplete because the chiral limit, in which the u, d quarks are massless, doesn’t represent the real world. The masses of u, d quarks are not zero, but rather  $m_u \sim 4$  MeV and  $m_d \sim 7$  MeV. More importantly, the light quarks are nondegenerate, and the  $\pi^0$  is mixed with other isospin zero mesons,  $\eta$  and  $\eta'$  [2]. In recent years, QCD corrections to the chiral anomaly prediction for the  $\pi^0$  decay width were estimated by a number of groups. The work of Goity *et al.* [2] involved a next-to-leading order (NLO) calculation in chiral perturbation theory, which estimated a  $\pi^0$  decay width of  $8.10 \pm 0.08$  eV. This calculation was at the

1% level and predicted an increase of about 4.5% from the chiral anomaly prediction. Another NLO calculation in chiral perturbation theory was carried out by Ananthanarayan and Moussallam [1], and their result was  $8.06 \pm 0.06$  eV. In 2009 Kampf and Moussallam [3] performed a next-to-next-to-leading (NNLO) calculation, which yielded a result of  $8.09 \pm 0.11$  eV. All these three results were in excellent agreement with each other. A sum rule estimation by Ioffe and Oganesian [15] including only the  $\pi^0$  and  $\eta^0$  mixing yielded a result of  $7.93 \pm 0.12$  eV. The fact that this result is about 2% lower than the other results due to their neglect of the  $\eta - \eta'$  mixing effect. The first three theoretical results are plotted in Fig. 1.5, and the average of these results is plotted against the experimental results in Fig. 1.6. Compared to the experimental results, these theoretical results show only 1% uncertainty and excellent agreement among themselves, which predict a 4.5% increase from the chiral anomaly prediction. On the experimental side, although the situation was improved after the PrimEx-I experiment, the data do not have a sufficient accuracy to confirm or refute the increase of  $\pi^0$  decay width as predicted. The theoretical value of the  $\pi^0$  two-photon decay width is among the most precise predictions of QCD. A precision measurement of  $\pi^0$  decay width is a fundamental test of low energy QCD and chiral perturbation theory. Therefore, it is important to carry out another measurement with a better precision.



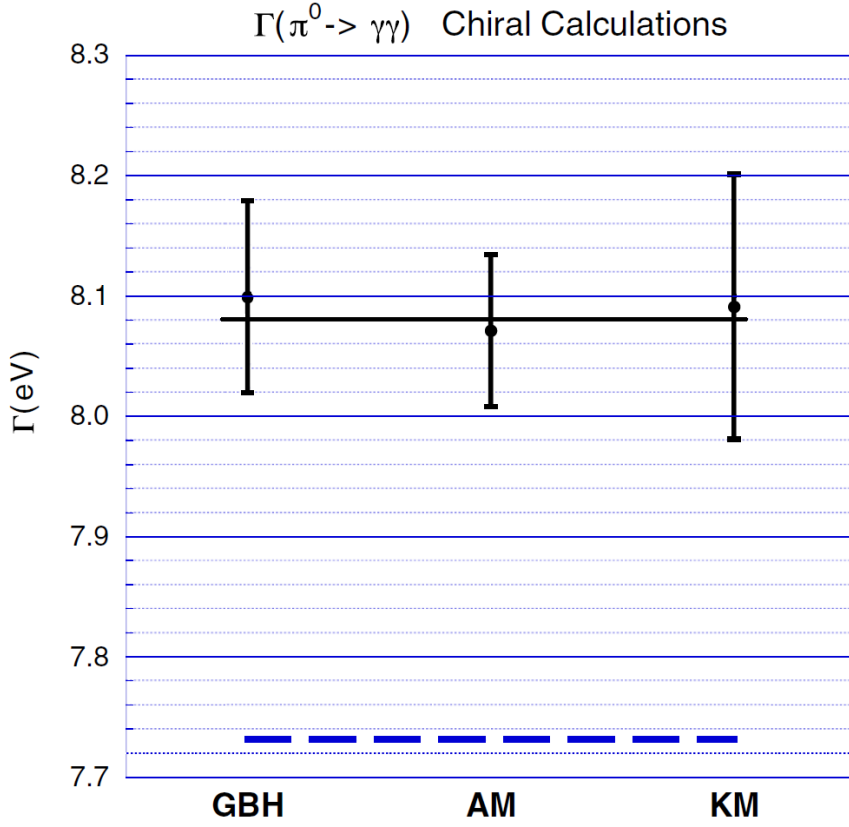


FIGURE 1.5: The theoretical predictions of  $\pi^0$  decay width. The lower long dashed line is the LO chiral anomaly prediction [12]. The upper solid line is the average of the higher order (NLO and NNLO) Chiral perturbation theory predictions [1, 2, 3], and the dashed lines show the estimated 1% uncertainty. The three theoretical predictions are from Goity *et al* [2], Ananthanarayan and Moussallam [3], and Kampf and Moussallam [3]. The results are  $8.10 \pm 0.08$  eV,  $8.06 \pm 0.06$  eV, and  $8.09 \pm 0.11$  eV, respectively.

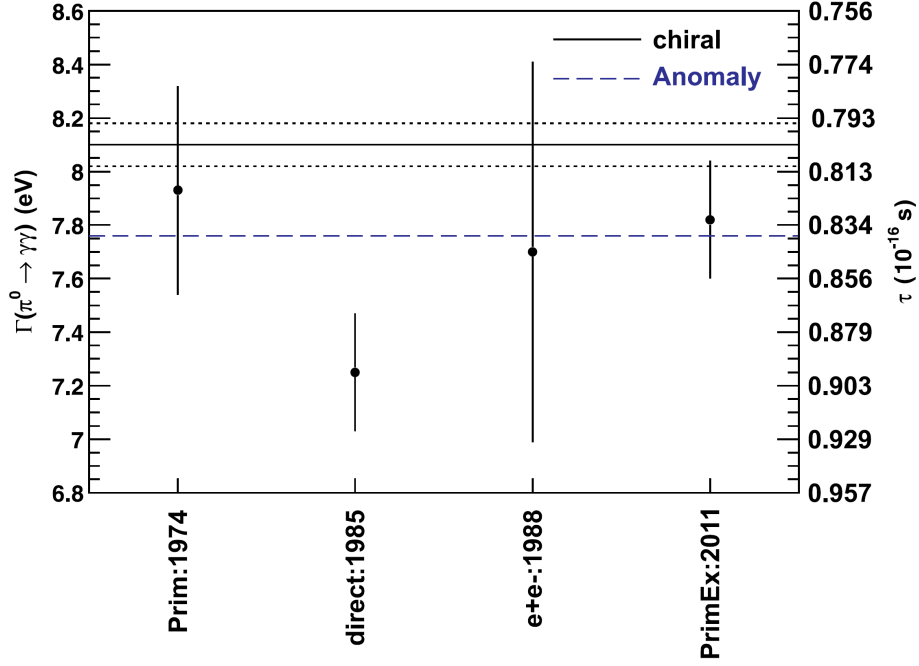


FIGURE 1.6: Experimental knowledge and theoretical predictions of  $\pi^0$  decay width. The lower dashed line is the LO chiral anomaly prediction [12]. The upper solid line is the average of the higher order (NLO and NNLO) Chiral perturbation theory predictions [1, 2, 3], and the dotted lines show the estimated 1% uncertainty. The four experiments are the 1974 Cornell Primakoff measurement [8], the 1985 CERN direct measurement [6], the 1988 DESY  $e^+e^-$  experiment [9], and the PrimEx-I experiment [4].

# 2

## Previous Experiments and Results

### 2.1 Overview

In general, there are three types of methods to measure the  $\pi^0$  lifetime, the direct method, the collider method, and the Primakoff effect. In this chapter, an overview of each method and the associated experiments will be presented.

### 2.2 The Primakoff Method

The Primakoff effect refers to the photoproduction of  $\pi^0$  in the Coulomb field of a nucleus as shown in Fig. 2.1(a). This idea was published by Primakoff in 1951 [16]. This effect can be seen as the inverse process of pion two-photon decay, shown in Fig. 2.1(b). The only difference is that in the Primakoff process a real photon is replaced by a virtual photon with non-zero mass. Since the momentum transfer is around 100 MeV, at high energy the change to the vertex factor due to this is negligible. Like the  $\pi^0$  two-photon decay process, the cross section of the Primakoff process is directly proportional to the  $\pi^0$  decay width, i.e., the reciprocal of the  $\pi^0$

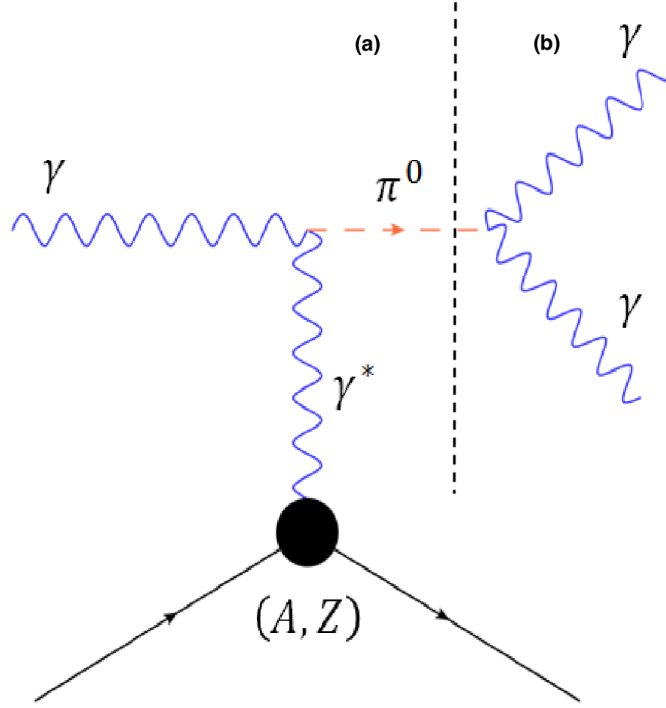


FIGURE 2.1: (a) The Feynman diagram for the Primakoff effect and the  $\pi^0 \rightarrow \gamma\gamma$  channel. A  $\pi^0$  is produced from the interaction between the real incoming photon and the virtual photon associated with electromagnetic field of the nucleus. (b) The  $\pi^0$  decays into two  $\gamma$ s. These two processes can be seen as reverse processes.

lifetime. The Primakoff cross section  $\frac{d\sigma_{Pr}}{d\Omega}$  can be written as [14]:

$$\frac{d\sigma_{Pr}}{d\Omega} = \Gamma_{\gamma\gamma} \frac{8\alpha Z^2}{m_{\pi^0}^3} \frac{\beta^3 E^4}{Q^4} |F_{e.m.}(Q)|^2 \sin^2(\theta_\pi),$$

where  $\Gamma_{\gamma\gamma}$  is the  $\pi^0$  decay width,  $Z$  is the atomic number of the target atom,  $m_{\pi^0}$ ,  $\beta$ ,  $\theta_\pi$  are the mass, velocity and production angle of the  $\pi^0$ ,  $E$  is the incoming photon energy,  $Q$  is the momentum transfer to the nucleus, and  $F_{e.m.}(Q)$  is the nuclear electromagnetic form factor of the target nucleus.

The difficulty of the experiment arises from the need to separate the Primakoff cross section from the nuclear photoproduction cross section. They are mixed at forward angles and interfere with an unknown phase. However, the distinct features

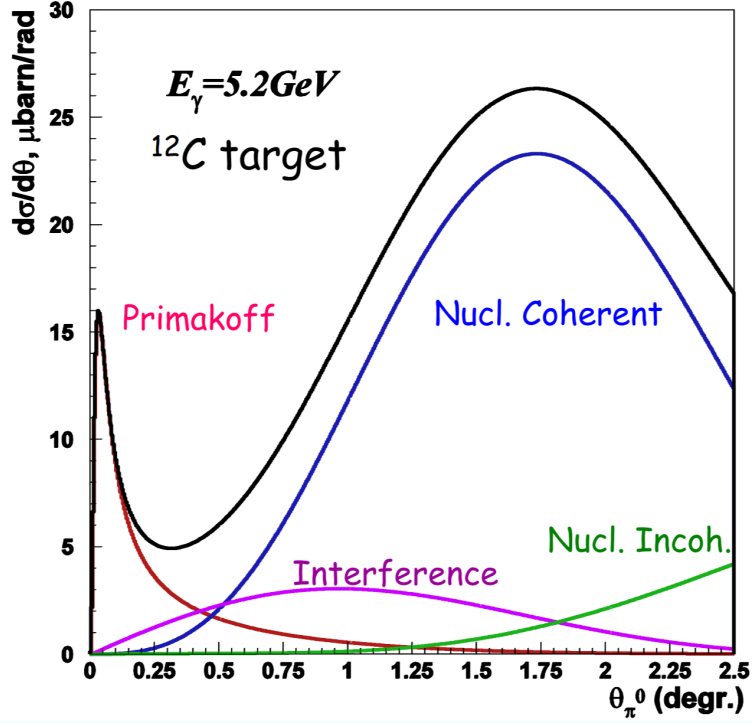


FIGURE 2.2: A schematic figure for the  $\pi^0$  photonproduction on a carbon targets with elastic cut. The incoherent process is suppressed due to this cut. The Primakoff cross section peaked at about  $0.1^\circ$ , while the nuclear coherent process grows slowly at forward angles. The interference between these two processes can also be seen.

of the Primakoff cross section make the separation possible. First, the Primakoff cross section is sharply peaked at a small angle  $\theta_{\pi^0} \approx m_{\pi^0}^2/2E_{\pi^0}^2$ . At 5 GeV this angle is about  $0.1^\circ$ . The Primakoff peak then drops fast to zero. To the contrary, the nuclear coherent photoproduction cross section increases slowly from  $\theta = 0^\circ$ . A schematic drawing of these two cross sections are shown in Fig. 2.2. Second, the Primakoff cross section is proportional to  $Z^2$  and  $E^4$ , so a relatively high  $Z$  nuclei target and high beam energy can help with the separation.

The Primakoff effect is a very common method that was used in the past by a number of experiments to measure the  $\pi^0$  lifetime. The very first two measurements with reasonable precision were performed by a DESY collaboration in 1965 [17] and

1969 [14]. The first attempt was at incident photon energies of 0.95 GeV and 1 GeV, and it measured a value of  $9.02 \pm 0.95$  eV. The second attempt measured a width of  $11.7 \pm 1.2$  eV at incident photon energy of 2.0 GeV. In the same year, another experiment at Tomsk [18] used a 1.1 GeV photon beam and measured a value of  $7.32 \pm 0.5$  eV. In 1974, using much higher incident photon energies of 4.4 GeV and 6.6 GeV, Browman *et al* from Cornell University measured the decay width of  $8.02 \pm 0.42$  eV [8].

It is worth noting that all the above mentioned experiments used conventional lead glass calorimeters and untagged bremsstrahlung photon beams. The precision of their results were limited by the detector resolution and beam energy resolution. The PrimEx-I experiment carried out in Jefferson Lab Hall B in 2004 took advantage of a high resolution electromagnetic calorimeter (HYCAL) and the Hall B photon tagging facility and achieved the best precision up-to-date. The obtained result is  $7.82 \pm 0.14 \pm 0.17$  eV [4] with only 2.8% uncertainty. In order to reduce the uncertainty to less than 2%, the PrimEx-II experiment was performed in 2010. The improvement of PrimEx-II over PrimEx-I will be discussed in chapter 3. The results from the Cornell experiment and PrimEx-I are selected in the current PDG value [7]. More details regarding the Primakoff method and the PrimEx experiments will be discussed in the following chapters.

## 2.3 Direct Method

Direct method obtains the  $\pi^0$  decay width by measuring the mean decay length. Since  $\pi^0$  has an extremely short lifetime ( $\tau \sim 10^{-16}$  s), one must take advantage of the relativistic time dilation to get the  $\pi^0$  to live long enough in the lab frame. A good understanding of the  $\pi^0$  spectrum is also required in order to obtain the lifetime with good precision. The first experiment of this kind was carried out at CERN PS in 1963 [19]. The precision was 17%. An improved version was performed at CERN

SPS in 1985 [6] at a higher energy. In this experiment, a 450 GeV proton beam was used to create the  $\pi^0$ s on a target consisting of two 70  $\mu\text{m}$  thick tungsten foils in parallel. The experimental set up is shown schematically in Fig. 2.3. The  $\pi^0$ s are produced in the first foil, and the second foil converts photons from  $\pi^0$  decay into electron positron pairs. At small distance, a fraction of the  $\pi^0$ s decay beyond the second foil, while at a large distance, all  $\pi^0$ s decay before reaching the second foil. The rate of positrons depends on the separations between the two foils. The experiment measured positrons at 150 GeV, which set a threshold for the  $\pi^0$  energy. By measuring the positron rate with different foil separations from 5  $\mu\text{m}$  to 250  $\mu\text{m}$ , the group was able to extract the mean decay length  $\lambda$ . The decay width obtained from this experiment was  $7.34 \pm 0.18 \pm 0.14$  eV. This was the most precise measurement of the  $\pi^0$  decay width before PrimEx-I. The main contribution to the systematic uncertainty came from the determination of the  $\pi^0$  momentum distribution, which was taken as the average of  $\pi^+$  and  $\pi^-$  momentum distributions. The pion energy spectra from the experiment is shown in Fig. 2.4. The  $\pi^0$  energy spectra was calculated based on the  $\pi^+$  and  $\pi^-$  spectra. The result from this measurement is included in the current PDG average [7].

## 2.4 Collider Measurement

A collider measurement of the  $\pi^0$  lifetime is also included in the current PDG average. It was performed by a group from DESY [9] using the Crystal Ball detector in the DORIS II storage ring. The Crystal Ball detector was made of a large array of NaI(Tl) crystals covering 93% of the solid angle [20]. The  $\pi^0$ s were created via electron positron collisions ( $e^+e^- \rightarrow e^+e^-\gamma^*\gamma^* \rightarrow e^+e^-\pi^0$ ) and the energy and angle of the decay photons were detected. Invariant mass cuts were used to separate  $\pi^0$ s from  $\eta$  and  $\eta'$ . Similar to the Primakoff effect, where  $\pi^0$ s were created via  $\gamma\gamma^*$  scattering, the cross-section of this process is also proportional to the two-photon de-

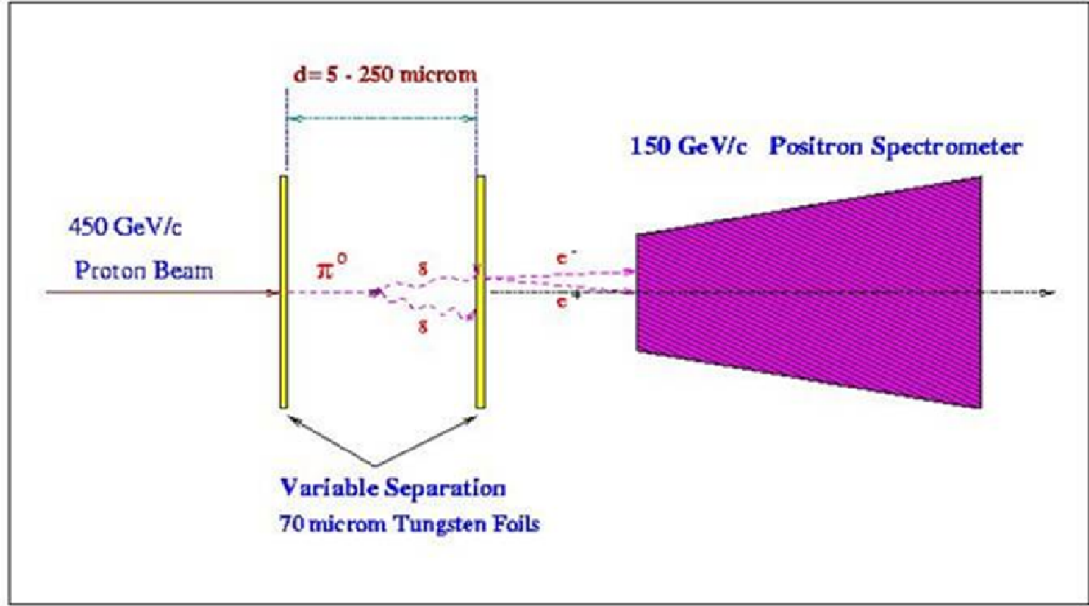


FIGURE 2.3: Schematic arrangement for the experiment to measure the  $\pi^0$  lifetime directly at CERN SPS in 1985 [6]. The  $\pi^0$ s were created by a 450 GeV proton beam incident on the first foil of two parallel tungsten foils. The second foil converted the decay  $\gamma$ s into  $e^+e^-$  pairs. The  $\pi^0$  decay rate changes in the same way as the rate of  $e^+$  when varying the distance between the two foils. The  $\pi^0$  mean decay length can be deduced and therefore the lifetime given the kinematic energy.

cay width of  $\pi^0$ . The backgrounds were studied by separate measurements and also suppressed by limiting the total transverse momenta of the produced mesons. The collider experiment uses the primary beam, and unlike other types of measurement, it only involves electromagnetic process so the backgrounds are relatively clean. The main contribution to the systematic error comes from luminosity normalization, cosmic ray, detector efficiencies and residual gas in the beam pipe. The Crystal Ball collaboration reported a result of  $7.7 \pm 0.5 \pm 0.5$  eV, which is consistent with the prediction of axial anomaly [20].



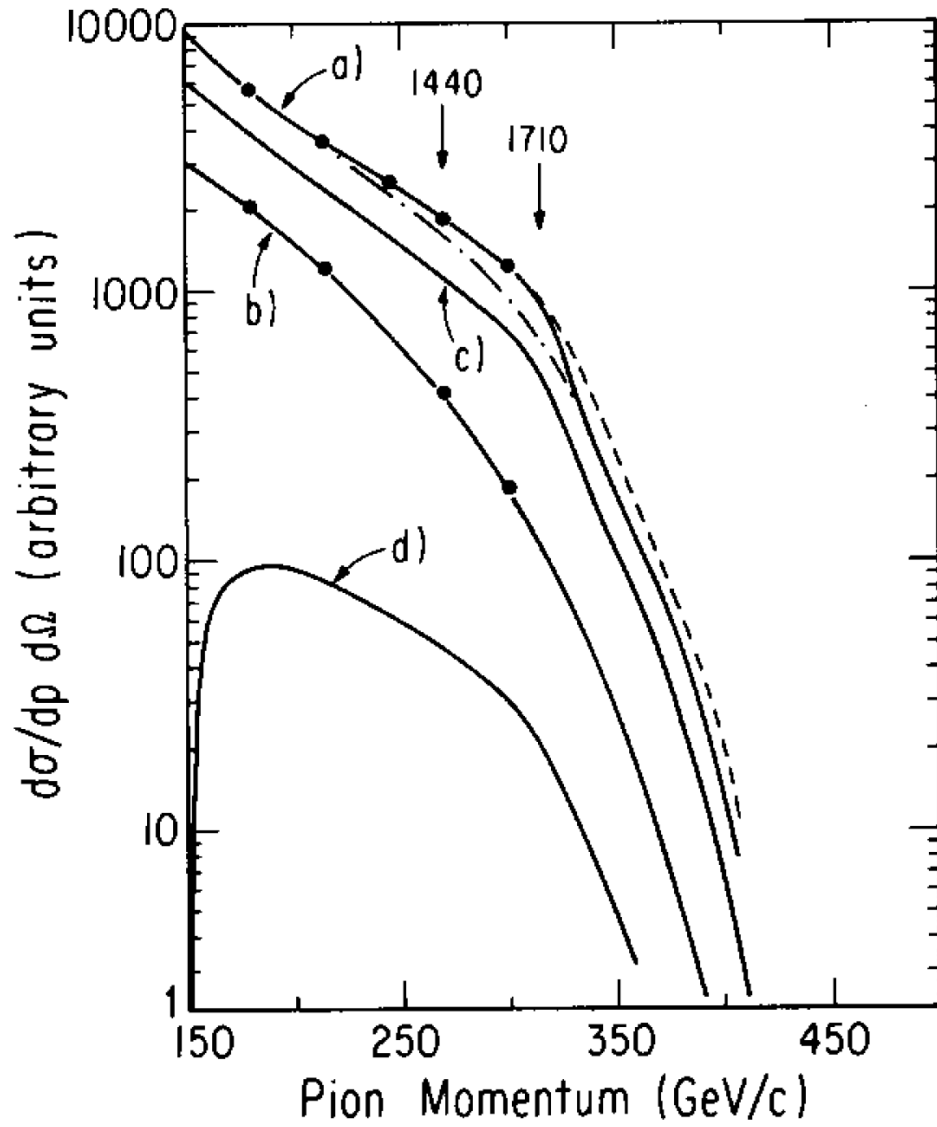


FIGURE 2.4: Spectra of pions produced at  $0^\circ$  by 450 GeV/c incident protons at CERN SPS [6]. The solid curves are the spectra used in the analysis. The solid circles are measured points. (a)  $\pi^+$  production spectrum; (b)  $\pi^-$  spectrum. (c)  $\pi^0$  spectrum calculated as the average from  $\pi^+$  and  $\pi^-$  spectra. (d)  $\pi^0$  spectrum that produces 150 GeV positrons. The dot-dash curve and the dash curve are variations of  $\pi^+$  spectrum used to estimate the systematic error.

## The PrimEx Experiment

### 3.1 Overview

Both PrimEx-I and PrimEx-II experiments were conducted at the Thomas Jefferson National Accelerator Facility (Jefferson Lab) in experimental Hall B. The PrimEx-I experiment was carried out in 2004 and its result was published 2011 [4]. The PrimEx-I experiment achieved a total uncertainty of 2.8% and was the most precise measurement of  $\pi^0$  decay width. In order to reach the ultimate goal of less than 2%, an improved version of the PrimEx-I, the PrimEx-II experiment was performed in 2010. In this chapter, the setup of PrimEx-II experiment and its improvement from PrimEx-I will be discussed in this chapter.

### 3.2 Thomas Jefferson National Accelerator Facility

Thomas Jefferson National Accelerator Facility is a U.S. Department of Energy national facility located in Newport News, Virginia. In its 6 GeV era, it consisted of a state of the art continuous wave electron beam accelerator facility (CEBAF), and three experimental halls (A,B, and C). The electron accelerator has one polarized

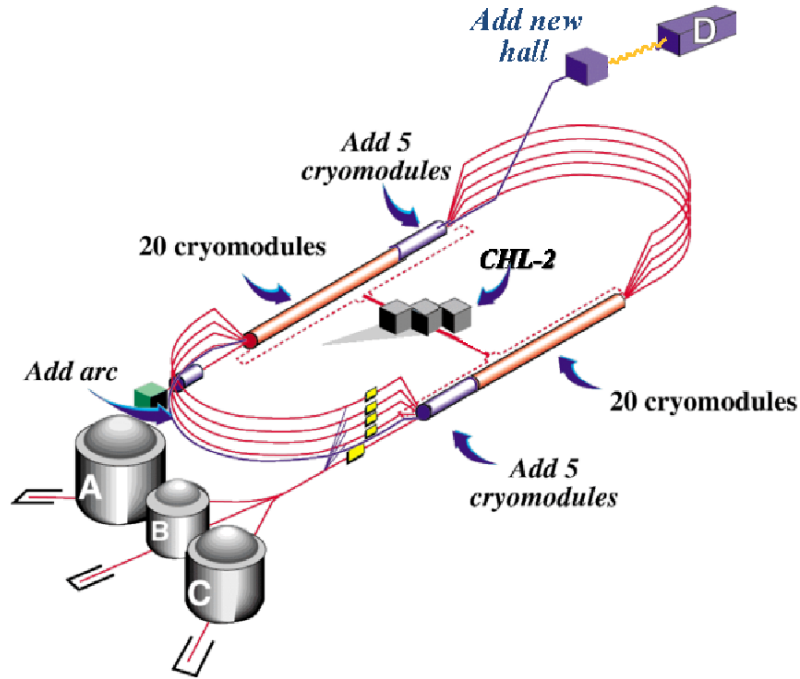


FIGURE 3.1: A schematic plot for the layout of the CEBAF and the experimental halls for the Thomas Jefferson National Accelerator Facility [21]. Both PrimEx-I and PrimEx-II experiments were performed in Hall B.

source, two super-conducting linear accelerator (linac), and two re-circulation arcs. Currently, JLab has just completed the 12 GeV upgrade. A new hall (Hall D), 10 cryomodules (5 for each linac), and two magnetic arcs have been added, as shown in Fig. 3.1.

### 3.3 Experimental Setup

The primary experimental equipment of PrimEx includes the Hall B photon tagger for the tagged photon beam, 10% radiation length solid targets (silicon and  $^{12}\text{C}$  for PrimEx-II,  $^{12}\text{C}$  and  $^{208}\text{Pb}$  for PrimEx-I), a pair spectrometer located downstream of the target, a high resolution hybrid calorimeter (HYCAL), and a plastic scintil-

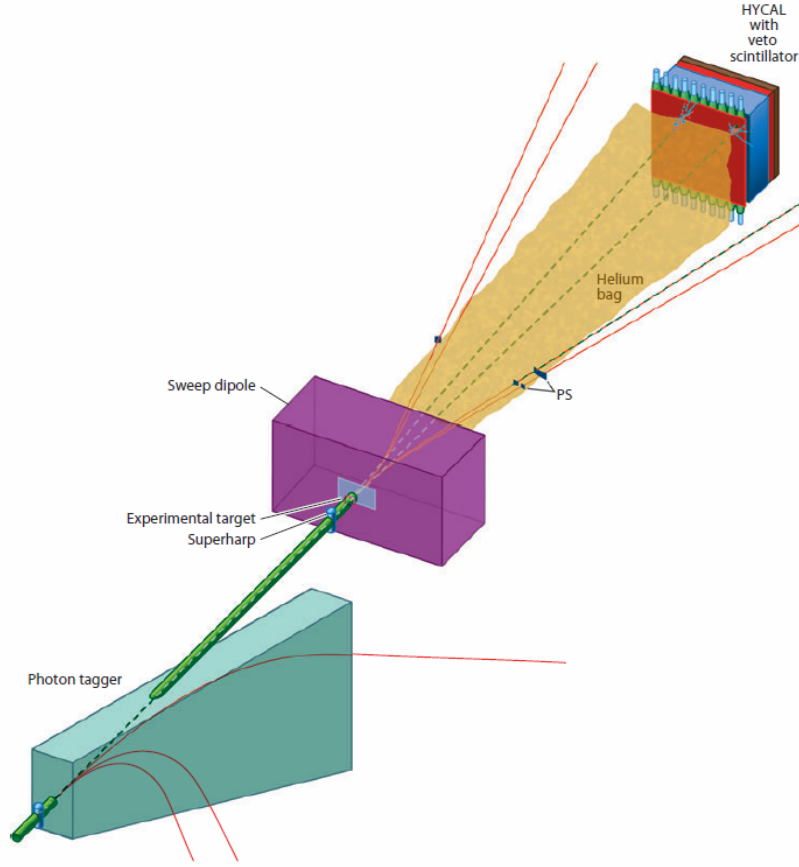


FIGURE 3.2: A schematic drawing for the experimental setup. The Hall B photon tagger, experimental targets, pair spectrometer, HYCAL and charged particle veto are shown. Also can be seen are the radiator, the superharp, the dipole magnet and the helium bag. The vacuum box, beam profile monitors (BPM) and photon beam position monitor are not shown.

lator charged particle veto in front of HYCAL. The experimental setup is shown schematically in Fig. 3.2.

The photon beam is created by placing a thin gold radiator ( $1 \times 10^{-4}$  radiation length) in the electron beam line, causing electrons to bremsstrahlung. The beam photon energy and timing are recorded by the photon tagger. These tagged photons produce the  $\pi^0$ s inside the target, and  $\pi^0$ s decay into two photons. The beam-line section upstream of the pair spectrometer is in the vacuum chamber. The decayed

photons first travel through the vacuum chamber, then inside the helium bag and eventually incident onto the HYCAL, where their energy and timing are recorded. The charged particles are deflected by a dipole magnet downstream of the target. Any residual charged particles will be excluded by the veto detector in the data analysis stage. The kinematic and timing information of the beam photon and decay photon is used for  $\pi^0$  reconstruction. The pair spectrometer is used to monitor the beam stability and calculate the relative beam flux tagging ratio by recording the intensity of pair production inside the target. The details of the major equipments will be discussed in the next few sections. A total absorption counter behind the HYCAL is used to measure the absolute flux tagging ratio in multiple intervals of the experiment.

Two beam position monitors (BPM's) for the electron beam are placed along the accelerator and Hall B enclosure, providing the electron beam position and profile information up to the radiator in tagger. There are also superharp scans (SHS's) located between the tagger and the target to monitor the electron and photon beam position and profile near the target. The photon beam position monitor (pbp) is placed behind the HYCAL in the beam path. Together these monitors offer a complete understanding of and help to correct any systematic shifts in the photon beam position and profile.

### 3.4 Hall B Photon Tagger

Before the 12 GeV upgrade, the Thomas Jefferson National Accelerator Facility can deliver an electron beam up to 6.1 GeV. The Hall B tagging system provides tagged photons in multi GeV energy range (20% to 95% of  $E_0$ ) with high energy resolutions ( $\simeq 0.1\% E_\gamma$ ). The PrimEx experiments only used the higher end of the energy spectrum since the Primakoff cross section is proportional to  $E_\gamma^4$ . The energy range for PrimEx-I was 4.89 GeV to 5.50 GeV, and the energy range for PrimEx-

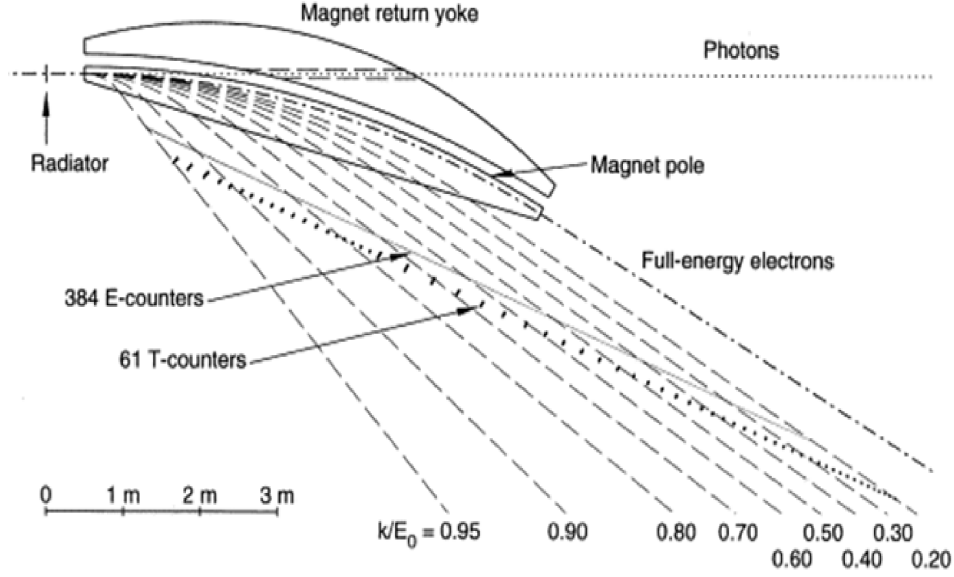


FIGURE 3.3: Overall geometry of the Hall B photon tagger. The tagger consists of a dipole magnet with a hodoscope containing two planar arrays of partially overlapping plastic scintillators in the focal plane. 384 E-counters and 61 T-counters are installed in the tagger. The tagger is able to provide a tagged photon beam with  $\simeq 0.1\% E_{\text{gamma}}$  energy resolution and less than 300 ps timing resolution. [22]

II was 4.20 GeV to 5.3 GeV. The energy range was increased in the PrimEx-II to improve the total event statistics. The tagged photon beam provided by the Hall B photon tagger is the major advantage of the PrimEx experiments over the previous Primakoff type of measurements.

The electron beam with incident energy  $E_0$  is “decelerated” by a thin high Z radiator and produces an energetic bremsstrahlung photon in front of the tagger. The post bremsstrahlung electron with energy  $E_e$  is bent subsequently by the tagger magnet. Most beam electrons do not interact with the radiator and are directed into the beam dump by the magnetic field. Those electrons that interacted with the radiator are bent to the E-counter and T-counter planes to determine the energy and timing information.

The geometry of the system is shown in Fig. 3.3. The tagger consists of a dipole

magnet with a hodoscope containing two planar arrays of plastic scintillators in the focal plane. The E-counters are scintillators in the first layer. In order to achieve high energy resolution, there are 384 of them, narrow in width, and each counter optically overlaps with its adjacent counters by  $1/3$  of its width to create 767 separate photon energy bins. A single energy bin represents approximately an energy interval of 0.3% of the beam energy. The second layer consists of 61 “T Counters”, lying 20 cm behind the E-counter plane. These are wider and thicker scintillators designed to output pulse shapes which provides precise timing information. The widths of the T-counter are varied to compensate the  $1/E_\gamma$  trend of the bremsstrahlung cross section so that the rates are roughly constant across all the counters. Each counter has a few mm overlap with its neighbors to make sure that no electrons escape through the gaps undetected, forming 121 channels. The designed timing resolution is 300 ps, and the best resolution achieved by the T-counter plane is 110 ps. More details can be found in [22]. The PrimEx-II used 18 T-counters and 180 E-channels in total, covering the higher end of the tagged photon beam spectrum.

### 3.5 Targets Thickness Measurement

PrimEx-I used a carbon and a lead target, both with thicknesses corresponding to  $\sim 5\%$  radiation length. The targets in PrimEx-II are silicon and carbon, and their thicknesses equal to  $\sim 10\%$  and  $\sim 8\%$  radiation length respectively. The silicon is a more balanced target than the carbon and the lead targets used in PrimEx-I. The Primakoff peak from the silicon target is more pronounced than the carbon target due to the higher atomic number, while not too high so that the cross section for the coherent process is not suppressed, as in the case of the lead target. This helps in the extraction of the Primakoff cross section. The statistics of the PrimEx-II is also increased by the use of the thicker targets.

The silicon target is made of 10 semiconductor wafers stacked together. Fig. 3.4

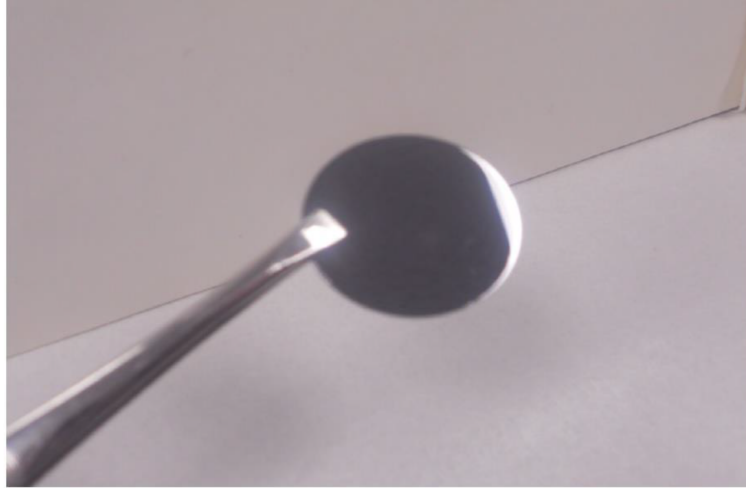


FIGURE 3.4: Polished surface of a Silicon wafer used in the PRIMEX II experiment.

shows one silicon wafer. The silicon target has the natural isotopic abundance (92.23%  $^{28}\text{Si}$ , 4.67%  $^{29}\text{Si}$ , 3.1%  $^{30}\text{Si}$ ). The diameter of the wafer is 1", and the thickness is 1 mm. These wafers are doped with phosphorus. However, the number density of the phosphorus is about 9 orders of magnitude smaller compared with silicon.

The carbon target is made of two blocks as shown in Fig. 3.5. Block #1 is "normal" graphite, and the block #2 used the highly ordered pyrolytic graphite (HOPG). The HOPG has low porosity compared with the "normal" graphite.

In the PrimEx experiments the  $\pi^0$  decay width is proportional to the Primakoff differential cross section. Therefore it is important to achieve high accuracy in the target measurement. The fractional uncertainty for the silicon target measurement is 0.35%. The fractional uncertainty for the carbon target measurement is 0.02%. The measurement of the silicon and the carbon targets can be found in [23] and [24]. We list the result of the measurement in table 3.1.



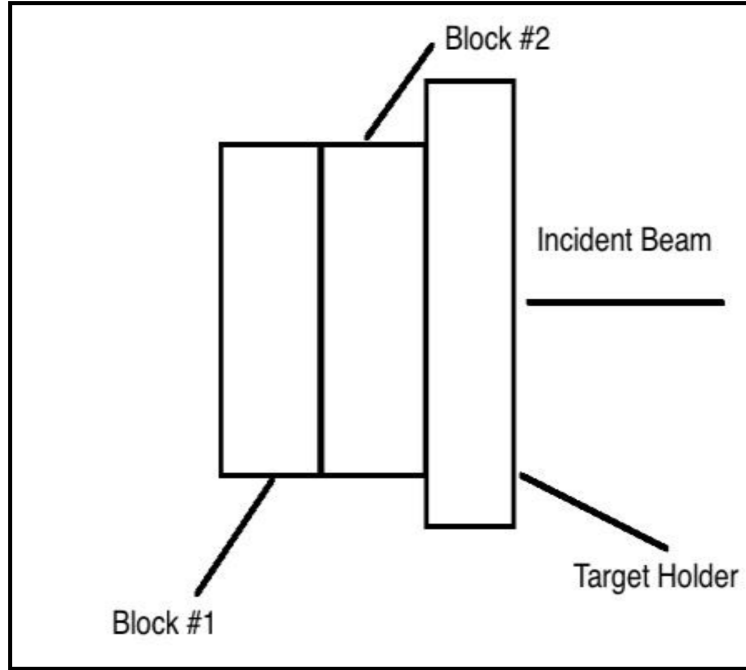


FIGURE 3.5: A schematic figure showing the PrimEx-II carbon target, which consists of two blocks of carbon graphite produced by different methods, taped together using Mylar tape.

Table 3.1: Target properties of PRIMEX-II

Target	Density $\rho \pm \Delta\rho$ (g/cm <sup>3</sup> )	Thickness $t \pm \Delta t$ (cm)	$N_t = \frac{\rho t}{M} \times N_A$ (10 <sup>-3</sup> /mbarn)	$\frac{\Delta N_t}{N_t}, (\%)$
Silicon	$2.316 \pm 0.008$	$1.0015 \pm 0.0003$	0.04973456	0.35
<sup>12</sup> C	$\rho t = 3.5304 \pm 0.007 (g/cm^2)$		0.17700914	0.02

### 3.6 The Total Absorption Counter and Absolute Photon Flux Tagging Ratio

The tagged photon flux at the target is an important factor in determining the cross section of the  $\pi^0$  photoproduction. A naive assumption, that the number of the tagged photons flux on the target is equal to the nubmer of hits on the tagging counters is not correct, and a few effects contribute to this. First, a bremsstrahlung photon can be produced and absorbed before reaching the target, but the post

bremsstrahlung electron is detected. Second, the Møller scattering in the radiator or the tagger produces an electron on the tagging counters without an accompanying photon. Third, extra hits can be registered in the tagging counters due to room background.

In order to solve this, a total absorption counter (TAC) is designed to measure the absolute tagging ratio, which represents the above mentioned effects. The absolute tagging ratio is defined as

$$R_{absolute}^i = \frac{N_{\gamma,i}^{tagged}(calibration)}{N_e^i(calibration)}, \quad (3.1)$$

for a given T or E channel  $i$ , where  $N_e^i$  is the number of detected electrons from that channel. The absolute tagging ratio is always smaller than one, due to the effects described above. The photon flux can be obtained by counting the detected bremsstrahlung electrons in the E or T channel:

$$N_{\gamma,i}^{tagged}(production) = N_e^i(production) \times R_{absolute}^i. \quad (3.2)$$

The total absorption counter is made by lead glass ( $20 \times 20 \times 40cm^3$ ). One 5 inch diameter Hamamatsu Photo Multiplier Tube (PMT) is attached to it. Because lead glass is susceptible to radiation damage, the TAC can only work under low beam currents. For PrimEx-II the beam current was lowered to  $50 - 70pA$  in the TAC run, while in the  $\pi^0$ production run the beam current was from 85 nA to 100 nA. And in the TAC run the target was removed so the beam photon can directly travel to the TAC. The tagger and TAC events rates were low under low beam currents, and under this condition the TAC efficiency is considered to be 100%. During the PrimEx-II experiment about 20 dedicated TAC runs were performed periodically to determine the absolute tagging ratio. Each run has from 1 to 10 million events statistics, some of them have targets in to measure the total absorption of the target. During the

experiment the TAC was damaged at one time and replaced. Below is a table 3.2 including the absolute tagging ratio for a few T-counters [25].

The absolute tagging ratio was proved to be insensitive to the beam intensity during PrimEx-I. The absolute tagging ratio was measured at different beam currents between 40 to 120 pA and no systematical beam current dependence was found as shown in Fig. 3.6 [26].

### 3.7 The Pair Spectrometer and the Relative Flux Tagging Ratio

Because the TAC can only work under low beam currents, the pair spectrometer was used instead to monitor the photon flux stability in the production runs with high beam currents. The PrimEx target works as a  $e^+e^-$  source for this purpose. The dipole magnet was turned on during the production runs, sweeping the  $e^+$ s and  $e^-$ s into the pair spectrometer. The pair spectrometer consists of two symmetrical arms, and each arm has two rows of scintillators. There are 8 scintillators in each row, with the ones in the front thinner than the ones in the back to minimize the change in the  $e^+$  or  $e^-$  trajectories. The widths of the scintillators are designed in such a way that one front scintillator matches with three back scintillators. A pair spectrometer event is defined by matching the  $e^+$  and  $e^-$  trajectories. In the analysis, each valid event requires a 4 fold timing coincidence from the left front, left back, right front and right back scintillators. This arrangement greatly reduces the accidental counts. The ratio between the number of  $e^+e^-$  pairs and the number of tagger photons is called relative photon tagging ratio, whose stability represents the photon flux stability.

However, in PrimEx-II many of the scintillators didn't work properly and were excluded from the data analysis. The resulted relative flux tagging ratio is not reliable. Instead, the number of elastic  $\pi^0$ s is used to monitor the flux stability. This analysis will be discuss in the next chapter.

Table 3.2: List of analyzed TAC runs and their parameters [25]

Run	Target	Beam current, [pA]	Statistics, $\times 10^6$ events	TAC module	T-counters opened	Comment	Tagging Ratio for certain T-counters, <sup>●</sup> [%]		
							T1	T10	T18
64711	—	70	1.2	old	19	—	86.08(7)	95.23(3)	96.60(2)
64744	—	70	3.7	old	19	bad voltage left-16	86.14(11)	95.32(3)	96.65(3)
64745	—	70	1.1	old	19	left-16 HV 1970, hall-A off	86.34(7)	95.67(2)	96.85(2)
64746	—	70	low	old	19	hall-A, hall-C off			
64748	—	70	junk	old	19	hall-A, hall-C off			
64848	—	70	1.6	old	19	~~~~	86.41(7)	95.50(2)	96.78(2)
64899	—	70	3.7	old	19	~~~~	86.22(4)	95.46(2)	96.79(1)
64903	Si	70	2.9	old	19	—	79.90(10)	88.55(6)	89.60(5)
64904	Si	70	1.7	old	19	—	79.97(9)	88.59(5)	89.56(4)
64995	—	50?	11.3	old	61	hall-A off, beam current increased in the middle	87.80(15)	96.03(5)	97.34(3)
64996	—	110?	3.8	old	61	hall-A off, <u>TAC 5 cm lower</u>	87.08(13)	95.91(4)	97.46(3)
64997	—	60?	10	old	61	HV 1900V	86.95(10)	95.92(3)	97.35(2)
65022	—	100	4.2	new	61	HV 1700V, ADC overflow	86.61(18)	95.12(5)	96.65(4)
65023	—	100	2.4	new	61	HV 1610V	87.31(19)	95.67(6)	96.81(4)
65025	—	100	10.5	new	61	~~~~	86.83(10)	95.89(3)	96.81(3)
65026	C	100	25	new	61	—	82.29(8)	90.74(4)	92.02(3)
65060	—	100	1.3	new	19	hall-A $3\mu\text{A}$ , hall-C $50\mu\text{A}$	86.36(7)	95.35(4)	96.80(3)
65061	C	100	1.4	new	19	—	80.79(15)	89.60(8)	90.78(8)
65063	Si	100	1.7	new	19	hall-A $3\mu\text{A}$ , ~~~~	80.16(10)	89.44(5)	90.52(4)
65064	—	100	0.9	new	19	hall-A off, hall-C $50\mu\text{A}$	85.79(10)	94.87(4)	96.41(3)
65098	—	100	5.7	new	38	hall-A $3\mu\text{A}$ , hall-C off	86.49(8)	95.83(3)	96.87(3)
65099	—	100	4.5	new	38	hall-A off, hall-C off	86.53(8)	95.52(3)	97.03(2)
65100	C	100	2.1	new	19	e+e- run with TAC	82.42(24)	91.27(13)	91.70(12)
65101	C	250	4.1	new	19	e+e- run with TAC	82.29(8)	90.89(6)	92.03(5)
65102	Si	250	4	new	19	e+e- run with TAC	81.48(8)	90.02(5)	90.95(5)
65103	—	250	1.1	new	19	e+e- run with TAC	86.23(11)	95.54(5)	96.65(4)
65104	Si	250	10.5	new	19	—	81.13(5)	89.68(4)	90.81(3)
65106	—	250	1.8	new	19	—	86.38(8)	95.53(4)	96.66(3)

<sup>●</sup> Errors on last digit(s) are given in brackets: 90.00(12) means  $90.00 \pm 0.12$ .

Values for runs with target were highlighted

~~~~ stands for unstable DAQ livetime

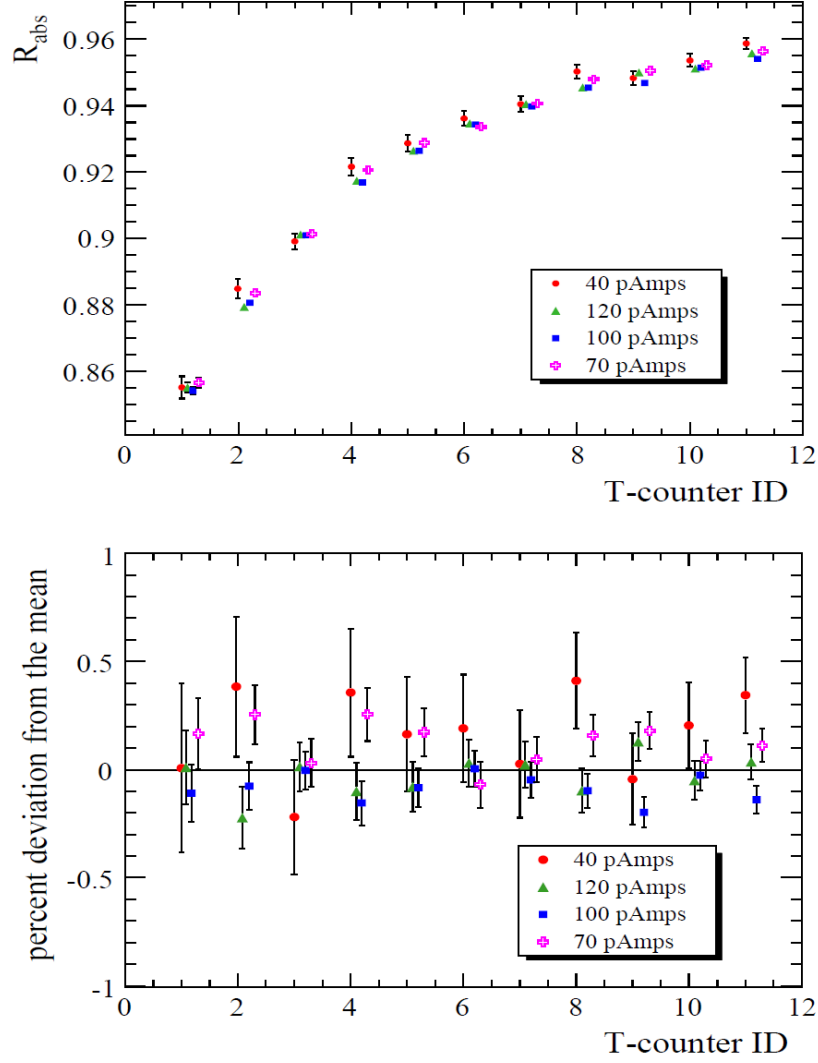


FIGURE 3.6: Top: absolute tagging ratio measured with different beam currents plotted as a function of the T-counter number. Bottom: The percent deviations for the absolute tagging ratio measured at different beam currents.

### 3.8 Charged Particle Veto Counters

The charged particle veto counters are used to filter any charged particles that may hit on HYCAL in the offline data analysis. A single veto counter is  $10 \times 0.5 \times 120 \text{ cm}^3$  and is made of organically doped scintillating plastic. Two Photonis XP2262/B PMT are attached to both ends. In PrimEx-I, 12 veto counters were placed side by side vertically as shown in Fig. 3.7. To enhance light collection, each counter is wrapped by a  $100 \mu\text{m}$  B1059B uncoated TYVEK and two layers of black Tedlar to achieve optical isolation. Due to the higher rate in PrimEx-II, additional 10 veto counters were added horizontal to form another veto plane. The 5 mm thickness of the veto counters is about 1.2% radiation length. The veto counter is made thin to minimize photon conversion. In PrimEx-II, the photon conversion is about 2%.

### 3.9 PrimEx Hybrid Calorimeter (HYCAL) and “Snake Scan” Calibration Runs

In PrimEx experiment, the  $\pi^0$ s are identified via the detection of their two decay photons in the calorimeter, and the  $\pi^0$  production angle and invariant mass are strongly dependent on an accurate determination of the positions and energies of the two decay gammas. To achieve a high precision measurement of the energy and direction of the  $\pi^0$ , the PrimEx collaboration developed a hybrid calorimeter (HYCAL).

The HYCAL consists of 1152 lead tungstate ( $\text{PbWO}_4$ ) scintillation crystals and 576 lead glass ( $\text{PbO}$ ) Cherenkov counters, all coupled with photomultiplier tubes (PMT). A map of HYCAL with the corresponding number id of each crystal is shown in Fig. 3.8. And Fig. 3.9 shows the HYCAL detector when it was installed in the test lab. The 1152  $\text{PbWO}_4$  detectors are arranged in a  $34 \times 34$  matrix in the center, and the lead glass crystals are divided into four  $24 \times 4$  groups, placed around

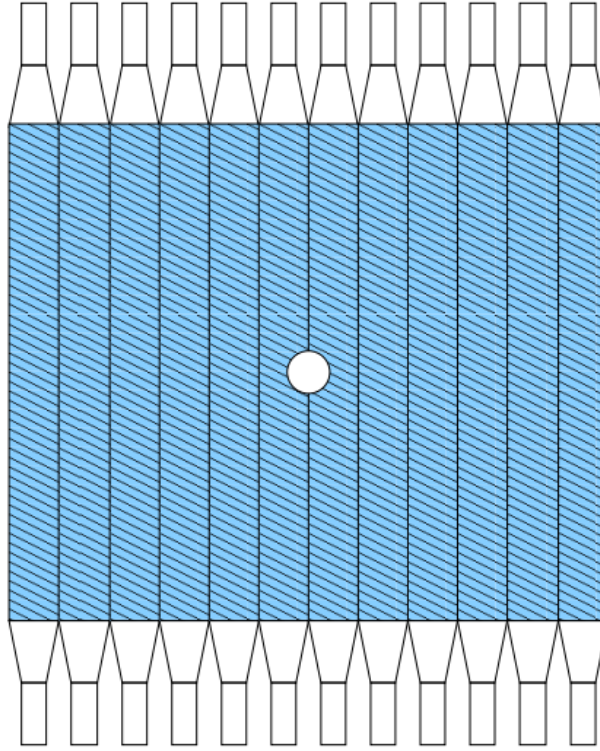


FIGURE 3.7: Twelve veto counters placed vertically side by side to form the veto plane. Two Photonis XP2262/B PMT are attached to the both ends of every counter. The hole in the center is for the photon beam to pass through.

the  $\text{PbWO}_4$ . The center of the HYCAL is a  $4\text{cm} \times 4\text{cm}$  hole (4 modules) to allow the photon beam to pass through. The whole HYCAL is about  $120\text{cm} \times 120\text{cm}$ , and the  $\text{PbWO}_4$  covers about  $70\text{cm} \times 70\text{cm}$  center area.

The  $\text{PbWO}_4$  is a very dense crystal ( $\rho = 8.28 \text{ g/cm}^3$ ), and has a very small radiation length ( $\chi_0 = 0.89 \text{ cm}$ ), and a small Molière radius ( $R_M = 2.0 \text{ cm}$ ). It also has the quality of fast scintillation. The lead glass is cheap and easy to handle and is a widely used Cherenkov calorimeter for decades in high energy physics. It is less dense ( $3.85 \text{ g/cm}^3$ ) and has a larger radiation length ( $\chi_0 = 2.7 \text{ cm}$ ). The  $\text{PbWO}_4$  crystal has much better energy resolution than the lead glass due to its higher light yield, since in Cherenkov calorimeter only shower tracks with  $v > c/n$  produce a detectable

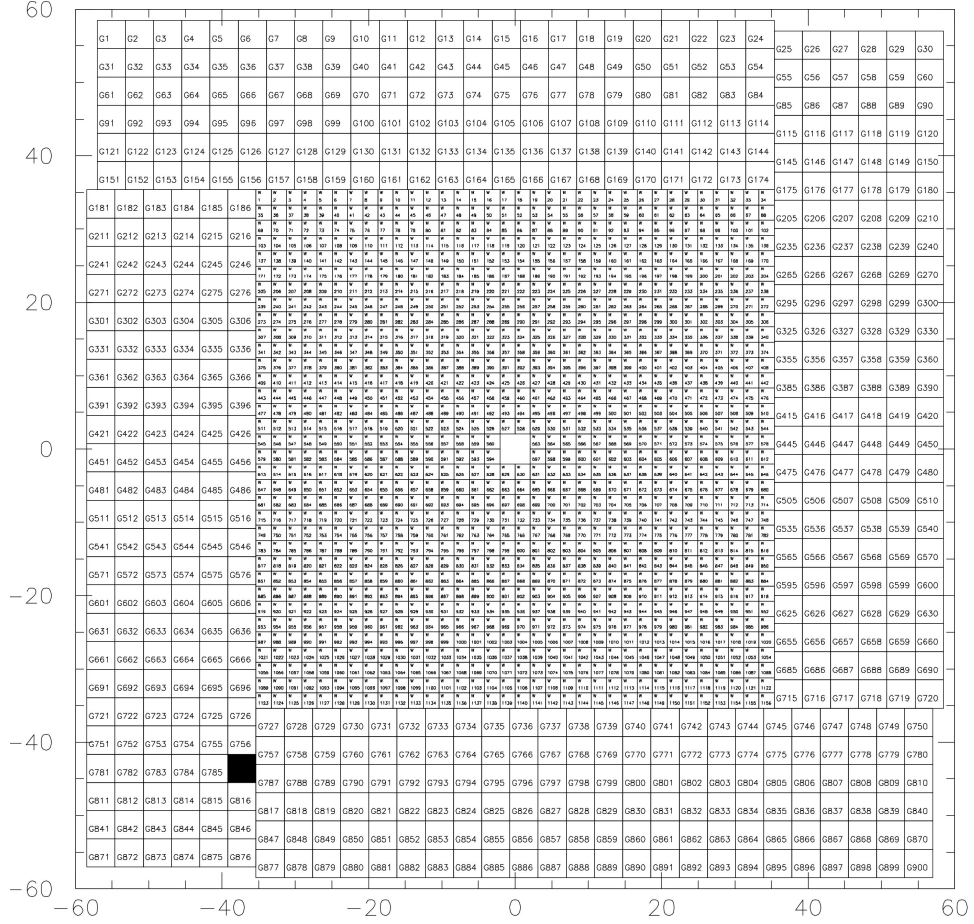


FIGURE 3.8: Virtual map of HYCAL with corresponding number of each crystal.

signal. Another drawback of the lead glass is the poor radiation resistance. The use of the  $\text{PbWO}_4$  modules greatly improves the energy and coordinate resolution of the HYCAL. The  $\text{PbWO}_4$  and lead glass crystal modules are shown in Fig. 3.10. The dimension of  $\text{PbWO}_4$  crystal module is  $2.05\text{cm} \times 2.05\text{cm} \times 18\text{cm}$  ( $20\chi_0$ ), and each lead glass module is  $3.8\text{cm} \times 3.8\text{cm} \times 45\text{cm}$  ( $12\chi_0$ ). Both crystal modules are made in such a size that the energy of one decay photon is mostly deposited into a single module. The  $\text{PbWO}_4$  crystal module is wrapped in  $100\text{ }\mu\text{m}$  TYVEK foil for individual optical isolation. The Hamamatsu R4125A PMT is used in the  $\text{PbWO}_4$  crystal module. It is connected mechanically to the crystal by a small brass faceplate and



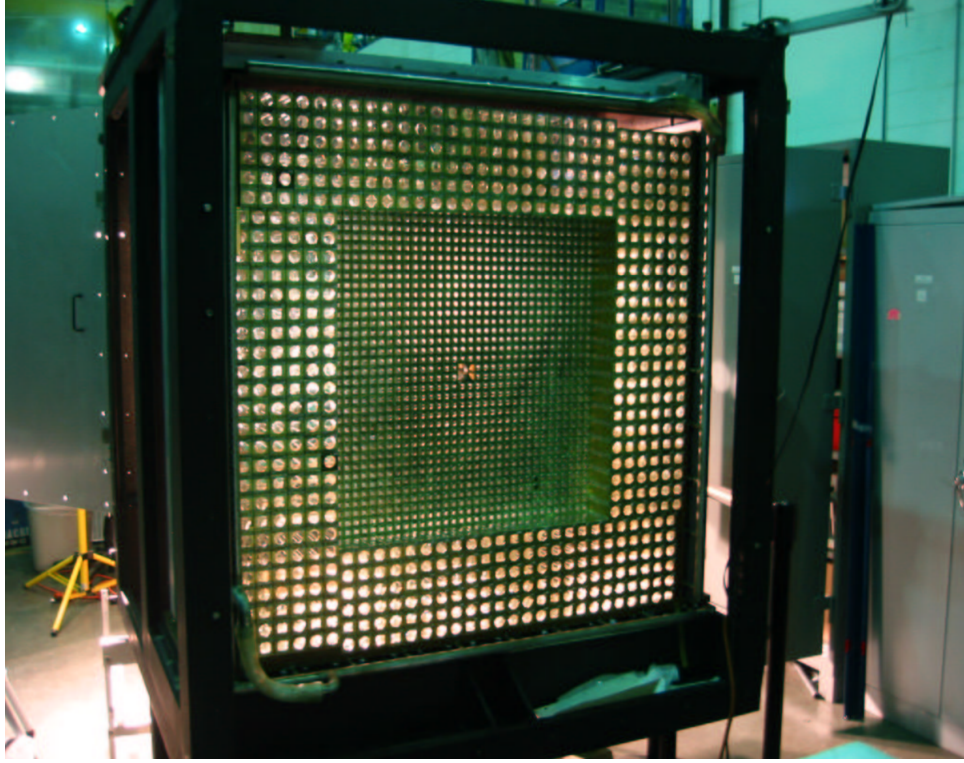


FIGURE 3.9: A photo of the HYCAL installed in the test lab. The  $\text{PbWO}_4$  crystal assembly can be seen placed further downstream (10 cm) with regard to the lead glass crystals to optimize energy sharing and minimize leakage.

thin brass strips along the edge of the crystal with optical grease. The final assembled  $\text{PbWO}_4$  crystal module is shown in Fig. 3.11. The lead glass crystal is wrapped in a  $24\mu\text{m}$  aluminized Mylar foil and each module is connected to the Russian made FEU-84-3 PMT in a similar fashion like the  $\text{PbWO}_4$ .

The light yield of  $\text{PbWO}_4$  crystal is inversely dependent on the temperature ( $\sim -2\%/^\circ\text{C}$  at room temperature). The crystal assembly is thermally isolated by water cooled copper plates on all four sides. The temperature was monitored by six temperature sensors during the beam test. The HYCAL crystal modules are maintained at a constant temperature of  $\sim 5^\circ$  as shown in Fig. 3.12.

Before and after the  $\pi^0$  production run, the HYCAL energy calibration was performed by the so called “snake scans”. The HYCAL was placed on the HYCAL

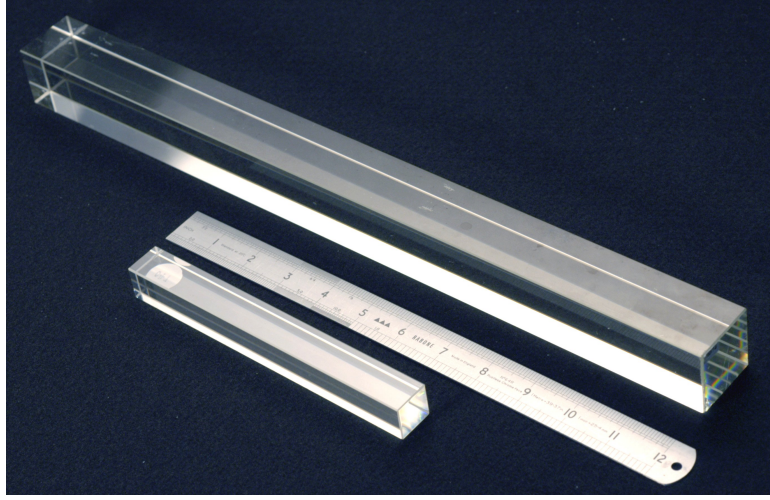


FIGURE 3.10: A photo of the lead glass crystal and  $\text{PbWO}_4$  crystal used in the PrimEx experiment. The lead glass crystal module is  $4\text{cm} \times 4\text{cm} \times 40\text{cm}$ , and the  $\text{PbWO}_4$  is  $2\text{cm} \times 2\text{cm} \times 15\text{cm}$ .

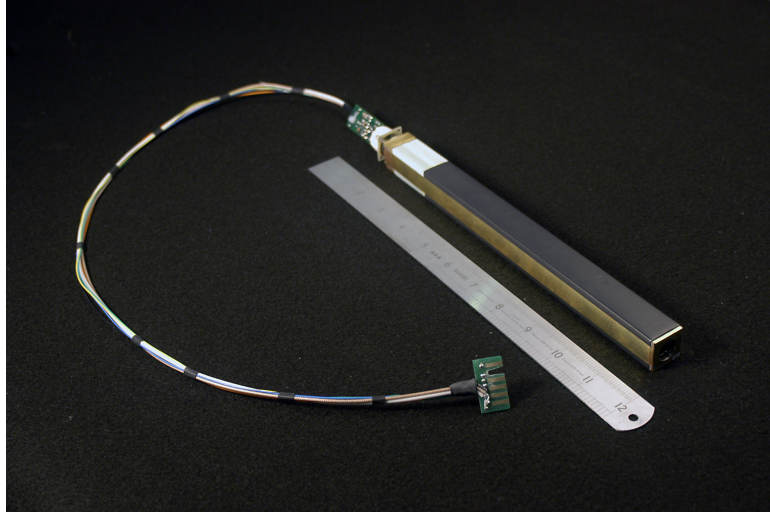


FIGURE 3.11: A  $\text{PbWO}_4$  crystal module sample. The  $\text{PbWO}_4$  crystal module is wrapped in  $100\ \mu\text{m}$  TYVEK foil for individual optical isolation. The Hamamatsu R4125A PMT is used in the  $\text{PbWO}_4$  crystal module. It is connected mechanically to the crystal by a small brass faceplate and thin brass strips along the edge of the crystal with optical grease.

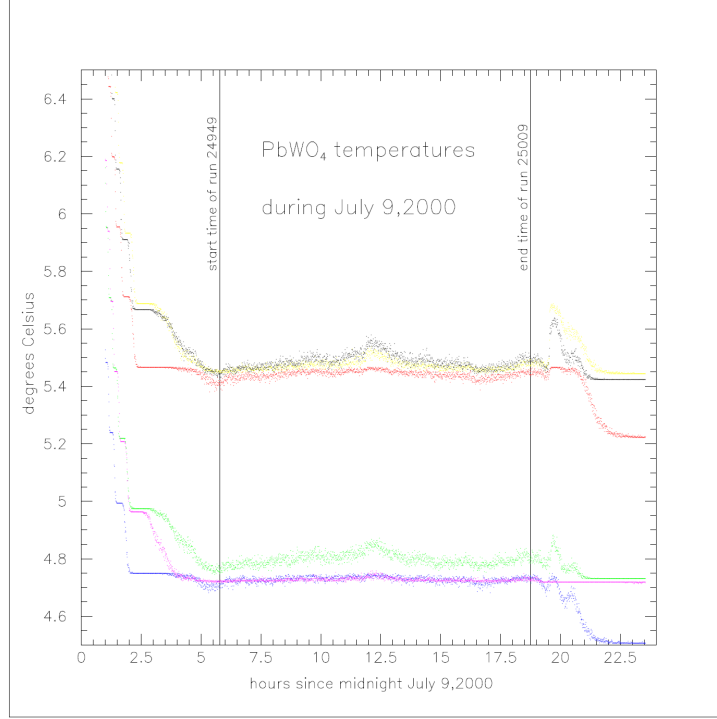


FIGURE 3.12: The temperature stability of the  $\text{PbWO}_4$  during a 12 hour period. [27]

Transporter as shown in Fig. 3.13. Powered by a 2-D step motor, the HYCAL was moved at a constant speed ( $\sim 2$  mm/s) with a low intensity ( $\sim 100$  pA) photon beam hitting on the surface. The “snake scan” starts at the center of one module, and the HYCAL was moved horizontally through the photon beam by the transporter until the end of the row. The HYCAL would then be moved vertically to allow the next row to be scanned as shown in Fig. 3.14. The  $\text{PbWO}_4$  modules and the glass modules were scanned separately, and there were dedicated scans over the transitional region. During this process the HYCAL PMT high voltages were adjusted so the output signals from the PMTs were roughly equal for the same beam energy. Later during the data analysis, the snake scan data were used to tune the HYCAL gain factor to get the correct energy. Another method to calibrate the gain factor takes advantage of the knowledge of the  $\pi^0$  mass. The HYCAL energy calibration process

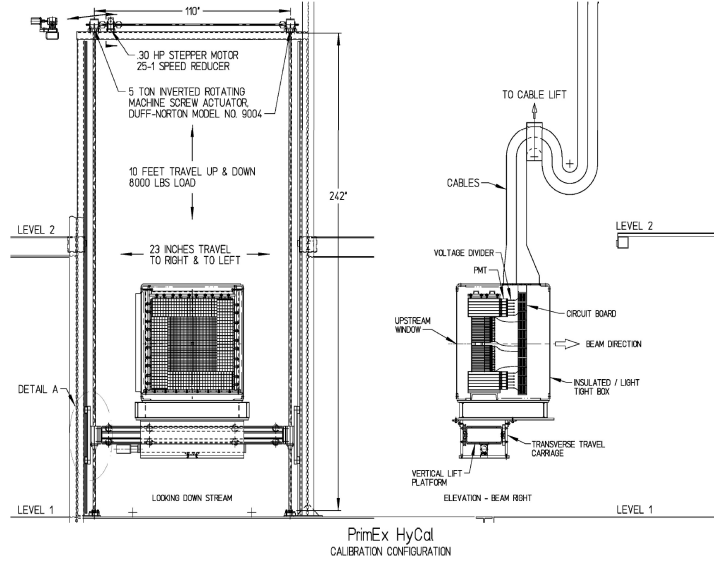


FIGURE 3.13: The HYCAL and its chassis sitting on the HYCAL Transponder.

will be further discussed in the next chapter. Finally, the HYCAL energy resolution is measured in the snake run to be less than 2% for the PrimEx energy range as shown in Fig. 3.15.

### 3.10 Beam Position Monitors, Superharp Scans and The Photon Beam Monitor

Two beam position monitors (BPM's) are placed along the accelerator and the Hall B enclosure. They are used to monitor the electron beam position beam entering the Hall B tagger.

The superharp scan is located in front of the Primakoff target to provide the photon beam position and profile at the target. It consists of a fork with three tungsten wires controlled by a stepper motor. The fork and the tungsten wires are placed in such a way that when moving the three wires across the beam, the beam profile along the horizontal and vertical directions can be depicted by measuring the  $e^+e^-$  pair production down stream in the pair spectrometer. A typical photon beam

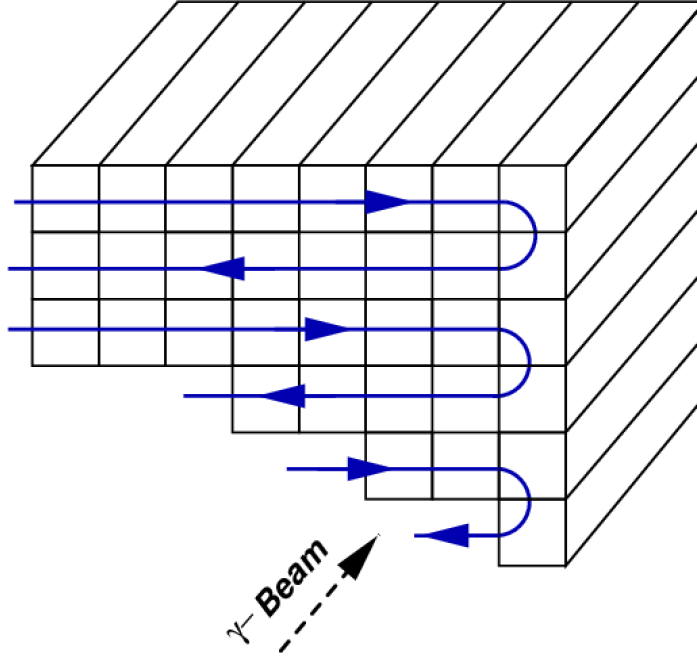


FIGURE 3.14: The calibration snake scan scheme.

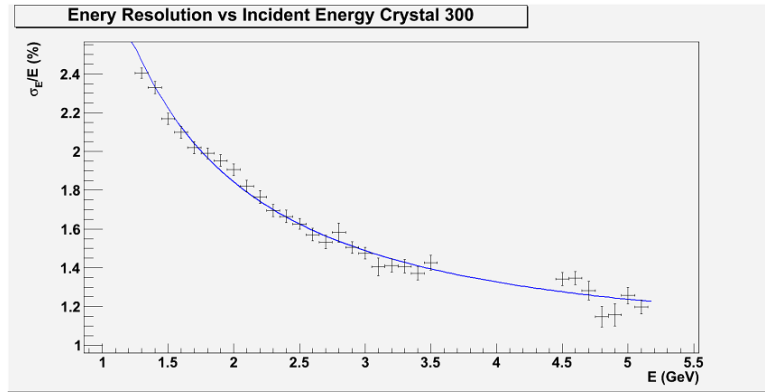


FIGURE 3.15: The HYCAL energy resolution obtained for the  $\text{PbWO}_4$  crystal module #300 during the “snake scan”.

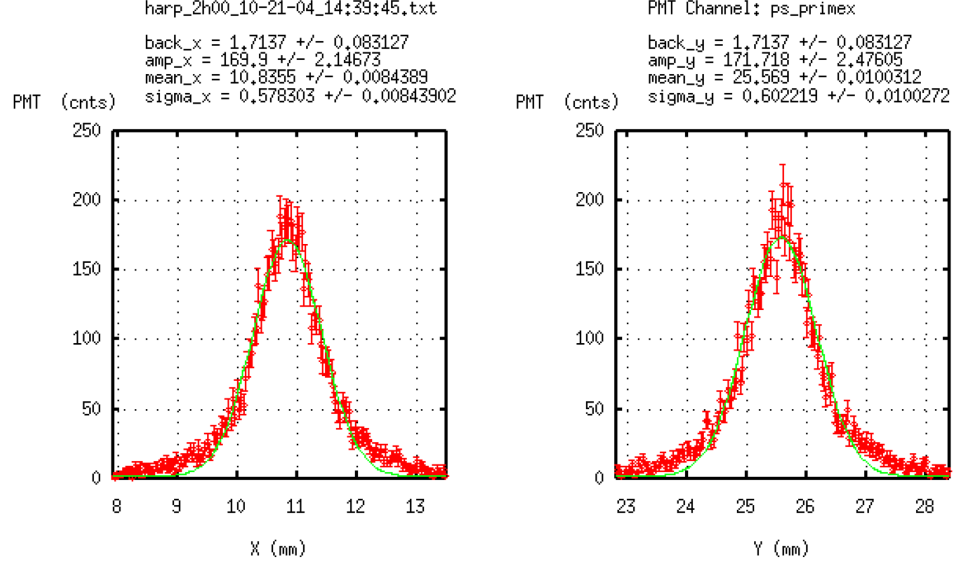


FIGURE 3.16: A typical photon beam profile from the superharp scan.

profile obtained by the superharp scan is shown in Fig. 3.16.

Electron beam scans are also done via a device similar to the superharp, but with thinner wires. A typical electron beam profile obtained by the harp scan is shown in Fig. 3.17.

The photon beam position monitor is located behind the HYCAL in the beam path. The photon beam position monitor consists of two nearly identical planes of scintillating plastic fibers, with 61 fibers in one plane along the X direction, and 62 fibers in the other plane along the Y direction. All the fibers are clad in a light reflection sheath. A photo of one of the two detector planes is shown in Fig. 3.18.

During the PrimEx-II experiment the pair spectrometer results were not reliable. Fortunately, the BPM's and the photon beam position monitor worked properly. The signals of both detectors were collected via the EPICS (Experimental Physics and Industrial Control System) interface during active beam condition at 30 s intervals. Coupled together, the BPM's and the photon beam position monitor provided real time beam position and profile information, defining the beam path from the tagger



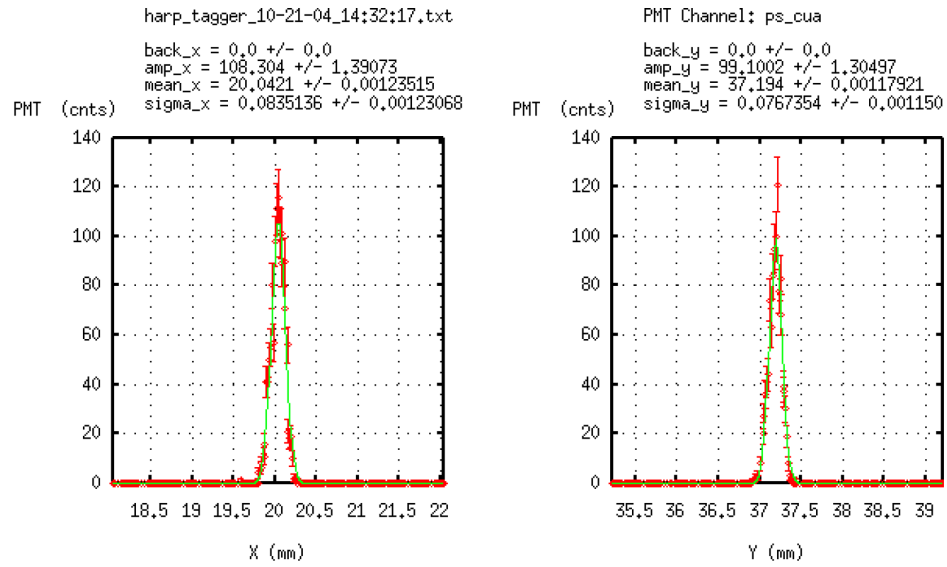


FIGURE 3.17: A typical electron beam profile from the superharp scan.

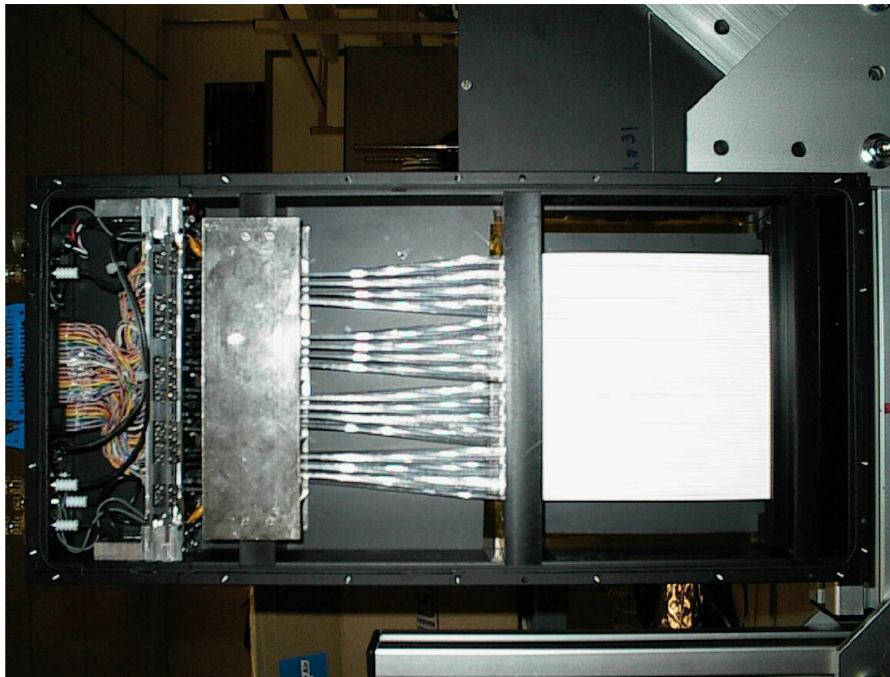


FIGURE 3.18: One plane of the photon position beam monitor. In the photo the electronics (left), light guides (center) and fibers (right) are shown.

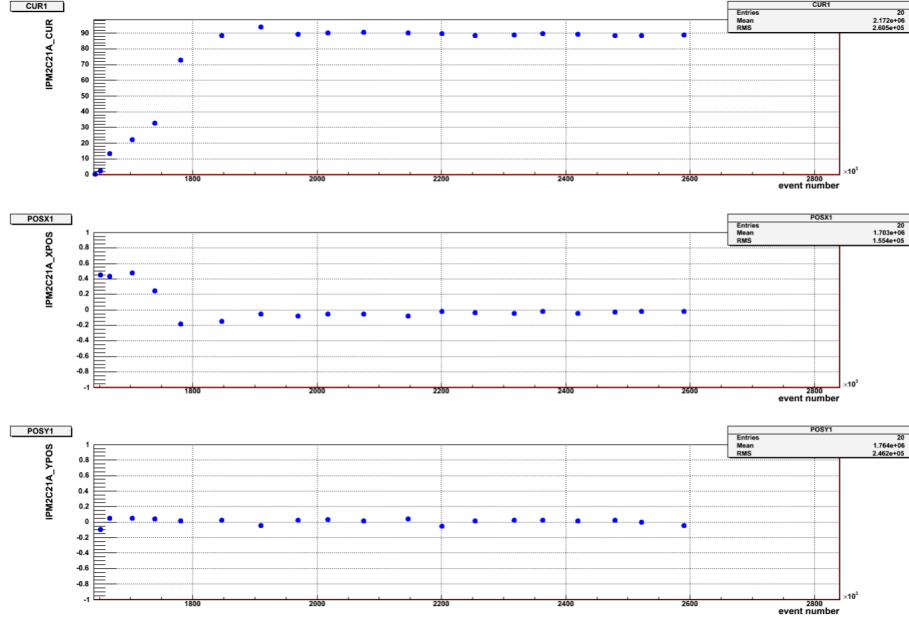


FIGURE 3.19: Beam current (top), X (middle) and Y(bottom) positions in BPM versus event number.

to the HYCAL. These beam parameters are later stored in a data base and used for beam flux analysis and to exclude problematic events . Fig. 3.19 shows the beam current, x position, y position in nA and mm at one time of the experiment. Fig. 3.20 and Fig. 3.21 show the photon beam x and y positions from the photon beam position monitor during the silicon run. From Fig. 3.21 one can see the photon beam position changed abruptly at one point during the silicon run. This is confirmed in the single arm compton study and will be discussed in the next chapter. For more details regarding the BPM's and photon beam monitor data, please refer to [28].

### 3.11 A summary of PrimEx-II Improvement

In order to achieve better precision than PrimEx-I, a few changes and improvements were implemented by the PrimEx-II collaboration. First and foremost is the design change that increased the event statistics. As was discussed in section 3.5, PrimEx-



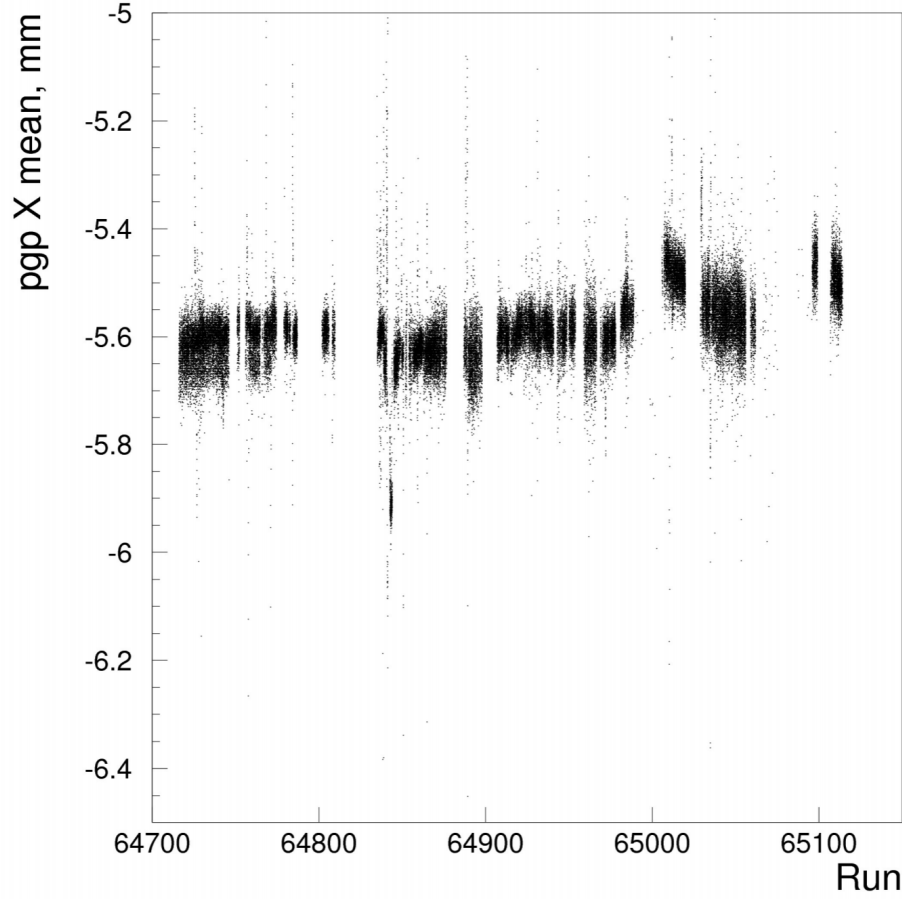


FIGURE 3.20: Photon beam X position from photon beam position monitor downstream HYCAL.

II used a silicon target with a 10% radiation length and a carbon target with a 8% radiation length, while in PrimEx-I both the carbon and lead targets were 5%. The photon beam energy interval was also increased by 1.5 times. In order to adapt to the higher rates, the capability of the DAQ system was improved from 2 kHz to 5 kHz. As a result, the number of the elastic  $\pi^0$  events from the PrimEx-II main target silicon is two times as many as that from the PrimEx-I main target carbon, while the carbon runs have the same number of events. The statistic error is roughly reduced by 1.5 times. Second, in order to reduce the systematic error, more empty runs were taken to help remove the background. The PID system was also improved by adding

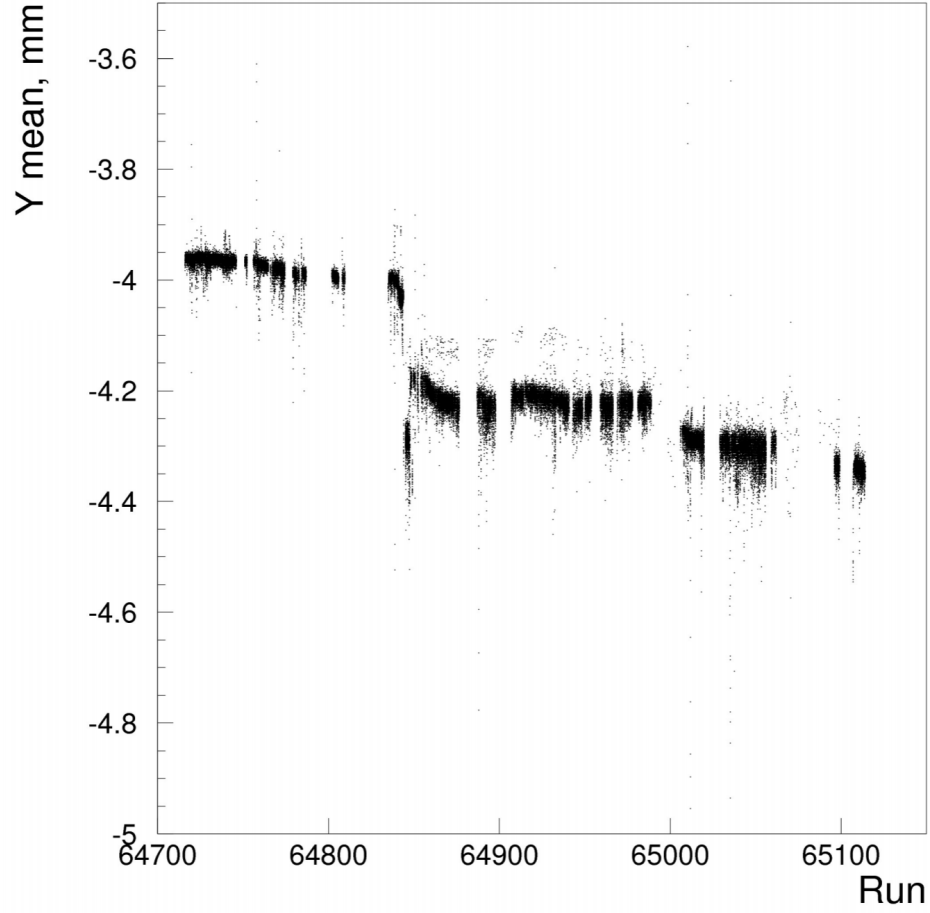


FIGURE 3.21: Photon beam Y position from photon beam position monitor downstream HYCAL.

the horizontal veto counters. Also the beam line was upgraded with stronger magnets so that the beam halo interaction with the beam pipe was further suppressed. Due to these changes, the PrimEx-II was able to achieve a precision of less than 2%. The data analysis and the results will be discussed in chapter 4 and chapter 5.

## Data Analysis

### 4.1 Overview

As discussed before, in order to measure the  $\pi^0$  decay width, the Primakoff type of experiment basically measures the cross section of the coherent  $\pi^0$  photoproduction on a solid target. The experimental cross section for  $\pi^0$  photoproduction is given by the following expression:

$$\frac{d\sigma}{d\theta} = \frac{dY_{\pi^0}^{tagged}}{N_{\gamma}^{tagged} \cdot \epsilon(\theta, E) \cdot t \cdot d\theta}, \quad (4.1)$$

where  $d\theta$  is the differential  $\pi^0$  production angle,  $dY_{\pi^0}^{tagged}$  is the yield of the tagged  $\pi^0$  within  $d\theta$ ,  $t$  is the target thickness,  $\epsilon(\theta, E)$  is a factor accounting for the geometrical acceptance and energy dependent detection efficiency, and  $N_{\gamma}^{tagged}$  is the number of tagged photon flux. Because the  $\pi^0$  photoproduction is azimuthally symmetrical, the denominator in the differential cross section is the polar angle  $\theta$  instead of a solid angle element  $d\Omega$ . The energy dependence is integrated over due to the limited event statistics. The calculation of the above mentioned variables will be discussed in the following sections.

Two quantities will be frequently used in this chapter. The first one is the two photon invariant mass  $m_{\gamma\gamma}$ , which equals the  $\pi^0$  mass. This quantity can be calculated from the momenta of the two decay photons,  $\vec{p}_1$  and  $\vec{p}_2$ . The energy of a photon equals the magnitude of its momentum since photons are massless. As introduced in section 3.9, the energies and positions of the decay photons can be measured by the HYCAL. The  $m_{\gamma\gamma}$  can be written in the expression of energies and HYCAL coordinates:

$$\begin{aligned}
m_{\gamma\gamma} &= \sqrt{(E_1 + E_2)^2 - (\vec{p}_1^2 + \vec{p}_2^2)} \\
&= \sqrt{2E_1E_2 - 2\vec{p}_1 \cdot \vec{p}_2} \\
&= \sqrt{2E_1E_2(1 - \frac{x_1x_2}{r_1r_2} - \frac{y_1y_2}{r_1r_2} - \frac{z^2}{r_1r_2})},
\end{aligned} \tag{4.2}$$

where  $E_1$  and  $E_2$  are the measured energies, and  $x_1, x_2, y_1, y_2$  are the HYCAL coordinates for the two decay photons. The variable  $z$  is the distance between the center of the HYCAL and the target. It is given by the survey. Variables  $r_1$  and  $r_2$  are the distance between the target and the HYCAL clusters, and they can be expressed as:

$$r_i = \sqrt{x_i^2 + y_i^2 + z^2}. \tag{4.3}$$

The second quantity is the elasticity of the two decay photons. The total energy of the two decay photons are the same as the  $\pi^0$ . Since we are only interested in the coherent  $\pi^0$  photoproduction process, the total energy of the  $\pi^0$  can be considered to be the same as the energy of the incoming photon within the detector resolution (the recoil energy of the nucleus is about 100 MeV). As a result, the ratio of the total energy of the decay photon and the energy of the incoming photon is about 1. This ratio can be used to exclude accidental events. In the analysis it is defined as:

$$elasticity = \frac{E_1 + E_2}{E_\gamma}. \tag{4.4}$$

## 4.2 Data Source and Run Numbers Used

All the run information of PrimEx-II can be found in the PrimEx log book [29]. For each run, the start and end time, the beam current, trigger rate, DAQ rate, converter status, radiator and target type, TAC detector status, and the data quality were recorded. The PrimEx-II run numbers are from 64281 through 65127. They are the first “snake scan”, from run 64281 to run 64424, the silicon production run from run 64716 to 64988, the carbon production run from 65006 to 65112, and the second “snake run” from run 65116 to run 65127. There were also periodic TAC runs to measure the “absolute tagging ratio” throughout the whole experiment, 14 empty target runs after the silicon production runs and 16 empty target runs after the carbon production runs for background subtraction, and periodic Compton scattering runs with the dipole magnet turned off to measure the Compton production for both silicon and carbon target. Since the Compton scattering is a well understood process, it is used to verify the value of the systematic uncertainties of the experiment. There were 9 silicon runs that were removed due to unfavorable beam conditions. The run numbers are 64802, 64803, 64804, 64808, 64809, 64839, 64841, 64850 and 64852. These run numbers are confirmed by the analysis of single arm Compton scattering events and the beam position. The details will be discussed later in this chapter. In this analysis, 141 production runs with silicon target and 40 runs with carbon target were used.

### 4.2.1 Event Preselection: Skim Files

Before the data analysis, the experimental data were filtered and skim files were produced to reduce the data size. The cuts used to produce the skim files are: 1) the minimum of HYCAL cluster energy is 0.1 GeV; 2) the minimum  $2\gamma$  invariant mass is 85 MeV.

#### 4.2.2 Single Arm Compton Scattering Analysis

The Compton scattering is used to systematically check the quality and the stability of the  $\pi^0$  data. However, during the  $\pi^0$  production the pair spectrometer magnet was on except for a few dedicated Compton scattering runs, which were taken only for short intervals. One method is to reconstruct the Compton scattering process using the  $\pi^0$  production runs. Since the scattered electrons from the Compton scattering are swept away by the pair spectrometer magnet, only the photons are used in the analysis, therefore this analysis is called single arm Compton scattering analysis.

The HYCAL detector provides the energy  $E'_\gamma$  and the  $x, y$  HYCAL plane coordinates of the scattered photon hits. The incoming photon energy  $E_\gamma$  is given by the tagger. These three kinematic variables satisfy the following equation:

$$E_\gamma = E'_\gamma \frac{m_e}{m_e + E'_\gamma(1 - \cos(\theta))}, \quad (4.5)$$

where  $m_e$  is the electron mass, and  $\theta$  is the polar angle, which can be obtained by:

$$\theta = \arctan\left(\frac{\sqrt{x^2 + y^2}}{z}\right), \quad (4.6)$$

where  $z$  is the distance from the target to the HYCAL  $\text{PbWO}_4$  surface, which is 702 cm for silicon and 701.2 cm for carbon. In this analysis only photons on the crystal modules are used.

Because at least two HYCAL clusters are required per event in the skim file, the raw data files are needed for the single arm Compton analysis. In order to reconstruct a single arm Compton event, one tagged photon and one HYCAL cluster are required. Therefore a single arm Compton scattering event is selected by requiring the coincidence between the HYCAL trigger and the MOR trigger. The MOR trigger is the master OR of all tagger T-counter signals. The HYCAL is triggered whenever the total energy deposition in HYCAL exceeds 2.5 GeV. A coincidence timing win-

dow of  $[-5, 4]$  ns is applied to the time difference between the HYCAL trigger and the MOR trigger so that accidental events are excluded. This timing cut is the so called Tdiff cut, which is also used in the  $\pi^0$  event selection. There is also a cut of 3.0 GeV on the scattered photon energy.

After all these selection procedures, there can still be multiple tagged photons and HYCAL clusters left in a single event. In this case all the tagged photon and HYCAL cluster pairs are taken into account in the analysis. For each pair, the incoming photon energy  $E_{\gamma,rec}$  can be reconstructed from the energy and polar angle of the scattered photon following equation 4.5. The difference  $\Delta E = E_{\gamma} - E_{\gamma,rec}$  will have a peak around zero as shown in Fig. 4.1. In order to measure the number of the Compton events, a fit is applied to the distribution of  $\Delta E$ . The fitting function used in the analysis is a double gaussian function plus a third order polynomial. The number of the Compton events is estimated by calculating the area under the fitted double gaussian peak. The number of single arm Compton events is then scaled by the relative flux for each run (the flux in the first run is set to be one). Although unsophisticated, this estimation successfully pointed out the instable runs. Fig. 4.2 shows the scaled single arm Compton scattering events yield for the silicon target runs. There are two sets of energy cuts used. The blue points show the study with energy cut  $E_{cluster} > 3.0 GeV$ , and the red points show the study with a tighter energy cut  $3.0 GeV < E_{cluster} < 4.0 GeV$ . Both studies show relative flat regions except for the runs in the middle from 64830 to 64852. These runs are cut off from the  $\pi^0$  analysis for the silicon target.

This finding is supported by the recorded beam position from the photon beam position monitor as shown in Fig. 3.21 [28]. As we can see, the beam position stayed stable for most of the time except for the same problematic run period, where the position changed rapidly in the y direction.

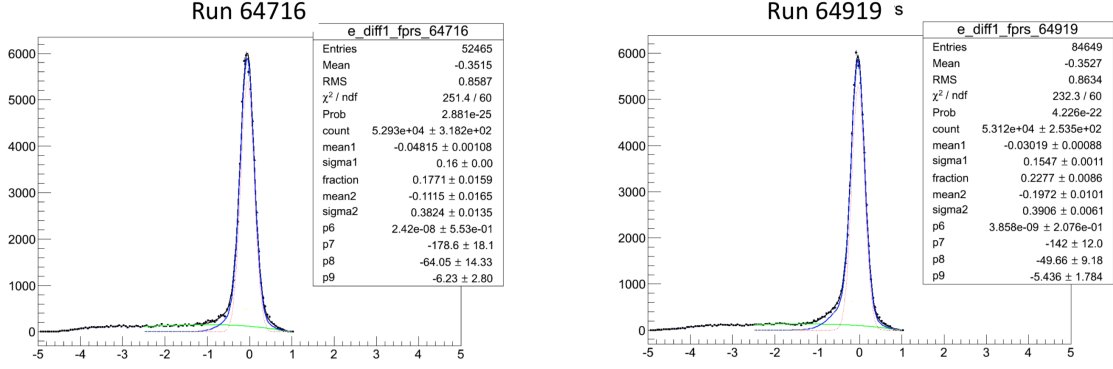


FIGURE 4.1: The difference between tagger photon energy  $E_\gamma$  and the reconstructed incoming photon energy  $E_{\gamma,rec}$  from single arm Compton scattering in two production runs 64716 and 64919. The peak is about zero. A fit is applied to the distribution using a double gaussian function and a third order polynomial. The solid blue curve is the double gaussian function, and the dotted blue curve shows the major gaussian shape. The green curve shows the background fitting. The solid black curve is the total fitting. The double gaussian function is set up in such a way that the first fitting parameter is the integration of the number of events under the peak. From these two figures we can read that for run 64716 there are 52930 events, and for run 64919 there are 53120 events.

## 4.3 Detector Software Calibration and Alignment

### 4.3.1 Tagger TDC Alignment

The design of the Hall B photon tagger was introduced in section 3.4. In this section the tagger TDC alignment process will be discussed.

The tagger has 61 T-counters and 384 E-counters. Each T-counter is a 2 cm thick plastic scintillator read out with two PMT's connected to both sides. Geometrically there are a few milimeters overlap between adjacent T-Counters to ensure there are no gaps. Each T-Counter is further separated into three T-Channels, the left channel, the center channel and the right channel, utilizing the coincidence between overlapping counters. This makes in total 121 T-Channels. The PrimEx-II experiment only used the first 20 T-counters and the first 103 E-Counters. However, the T-counter 19 and 20 were dead during the experiment so only the first 18 T-counters were used



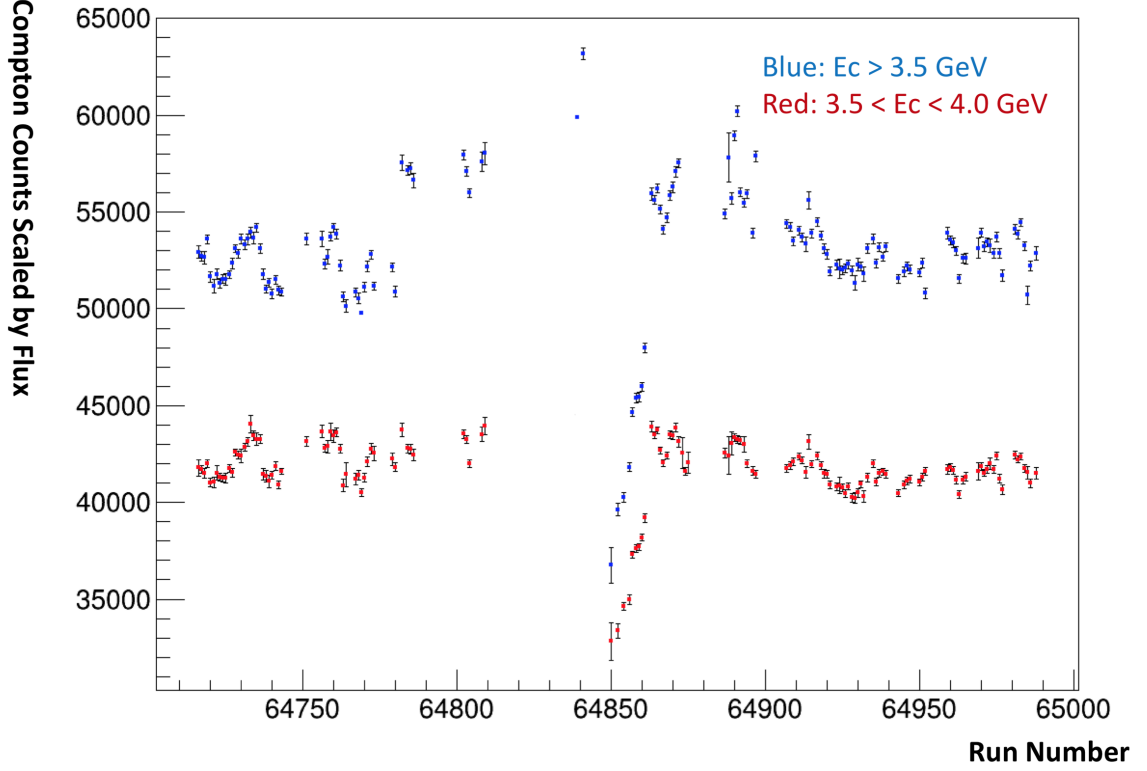


FIGURE 4.2: The number of the single arm Compton scattering events scaled by the relative flux for each run (the flux in the first run is set to be one) as a function of run number for silicon target. There are two sets of energy cuts used. The blue points show the study with energy cut  $E_{cluster} > 3.0 \text{ GeV}$ , and the red points show the study with a tighter energy cut  $3.0 \text{ GeV} < E_{cluster} < 4 \text{ GeV}$ . Both studies show relative flat regions except for the runs in the middle.

in the analysis.

The offset for the tagger TDC needs to be calibrated so that adjacent T-channels can provide consistent timing when a single photon passes through them. For TDC alignment purpose the “snake scan” data is used, and only MOR trigger is used to select events. Two offsets are assigned to each T-Counter,  $T_{left}$  and  $T_{right}$ . There are two steps for the TDC alignment. In the first step, the time difference between the left and right TDC’s for the same T-Counter,  $\Delta_{LR}$ , is obtained by finding its peak

position. The relation between  $T_{left}$  and  $T_{right}$  is determined as:

$$T_{left} = T_{right} + \Delta_{LR}. \quad (4.7)$$

In the second step, adjacent T-Counter timings are compared. The timing of T-Counter  $i$ ,  $T_i$  is defined as the average of its left and right TDC values. Two adjacent T-counter  $i$  and  $i + 1$  should always give consistent timing, *i.e.*,  $T_i = T_{i+1}$ , when a post bremsstrahlung electron passes through the overlapping area between them.

This chains the TDC offset of all T-Counters together. In the alignment process, the  $T_1$  is set to zero, and all the following T-Counter timings are also aligned to zero by applying the corresponding offsets. If we write the offset for the  $i^{th}$  counter to be  $\Delta_i$ , then  $T_{left}$  and  $T_{right}$  are:

$$T_{left} = -\Delta_i + \frac{\Delta_{LR}}{2}, \quad (4.8)$$

$$T_{right} = -\Delta_i - \frac{\Delta_{LR}}{2}. \quad (4.9)$$

A collection of offsets are calculated similarly for all the E-counters in order to maintain consistent timings against corresponding T-counters. Unlike T-counter, an E-counter requires a single offset constant since it only connects to one TDC.

The alignment offsets for tagger TDC are calculated run by run through run 64704 to 65127 to ensure the timing stability through the whole experimental data set. During this study multiple dead TDC channels were found and excluded from the analysis. The TDC alignment offsets and status tables were added to the PrimEx calibration database. For more details on TDC alignment, please refer to [30].

#### 4.3.2 The HYCAL Cluster Reconstruction Algorithm

The HYCAL is the calorimeter used in the PrimEx experiments. A detailed introduction of this calorimeter was presented in section 3.9. Although the majority of

the energy of a photon is deposited inside a single HYCAL module, the surrounding HYCAL modules will most likely still be fired. The collection of these HYCAL hits from a single photon is called a HYCAL cluster. The HYCAL clusters are reconstructed using the so called island clustering algorithm. This new algorithm is developed for PrimEx-II to accommodate the higher event rates. In PrimEx-I, the clustering algorithm is the 5x5 algorithm, which first looks for the maximum energy deposition cell, and then declares all 5x5 area around belonging to one cluster. The island algorithm is more sophisticated. It first finds all the “raw” clusters as connected areas, *i.e.*, the “islands”, and then attempts to split each “raw” cluster into multiple smaller ones based on the distribution of energy deposition. More precisely, the algorithm finds all the local maxima and splits the deposited energy among them using statistical techniques. One such “raw” cluster can be reconstructed up to 12 HYCAL clusters. The algorithm effectively distinguishes closely neighbored HYCAL hits as shown in Fig. 4.3. For more details, please refer to [31].

#### *4.3.3 HYCAL Energy Software Calibration*

The decay photon energy is one of the most important factors to determine the  $\pi^0$  kinematics and the invariant mass. The HYCAL energy calibration will affect the precision of the photon energy determination. The calibration is proceeded in two steps. First, the “snake run” data were used to calculate an initial gain factor for each HYCAL module. Two separate groups of calibration runs were carried out before and after the experiment. Second, after the initial HYCAL gain factor is obtained, the two  $\gamma$  invariant mass is used to further improve the HYCAL gain factor.

##### *HYCAL Energy Calibration Using “Snake Run” data*

As discussed in section 3.9, in the “snake run” the beam photons are directly incident on to the HYCAL module. Because only a single HYCAL cluster is formed and

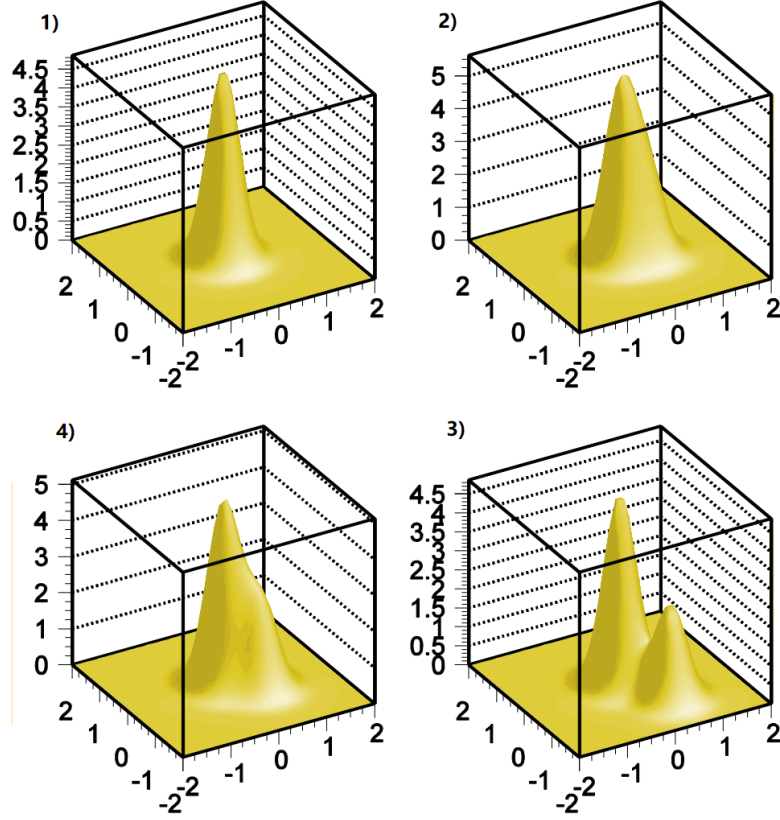


FIGURE 4.3: Monte Carlo simulated HYCAL hits energy deposition applied with the “island” algorithm. From the top left figure and clockwise: 1) A single cluster; 2) Two clusters but can’t be separated; 3) Two clusters do not produce two maxima but can be distinguished; 4) Two clusters produce two maxima and are both identified.

almost all the energy is deposited into its central module, *i.e.*, the module with the most energy deposition within a cluster, the gain factor of this module is adjusted so that the cluster energy equals the beam energy. The gain factor is defined as:

$$corr_{snake} = \frac{E_{beam}}{E_{cluster}}. \quad (4.10)$$

Since a HYCAL cluster spreads across multiple HYCAL modules, adjusting the gain factor of one module has the potential to affect the gain factors of the surrounding modules. This effect makes it necessary to iterate through the same procedure multiple times until the gain factors of all the HYCAL modules stabilize. Typically, the

gain factors converge after 4 to 5 iterations as shown in Fig. 4.4. In the analysis 10 iterations were performed on all HYCAL modules. The gain factor obtained from the second “snake run” is shown in Fig. 4.5. These gain factors are used as the starting points for the next calibration step.

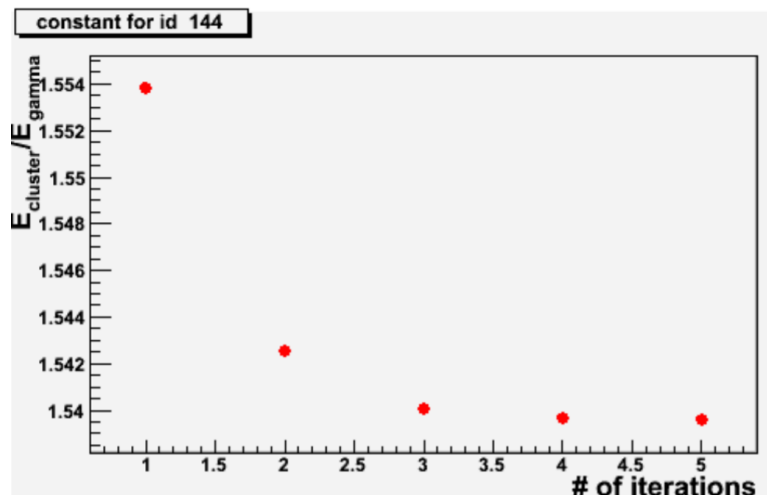


FIGURE 4.4: Change of gain factor of HYCAL module Id 144 over five iterations.

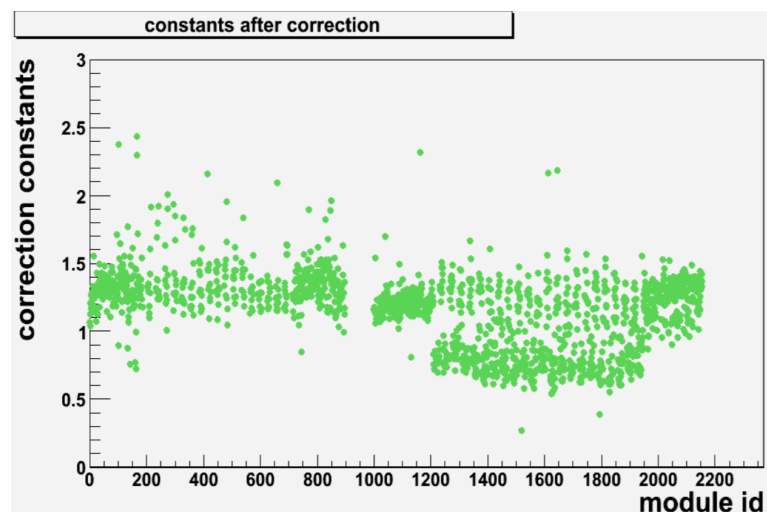


FIGURE 4.5: Calibration constant vs. module Id for both crystal and glass for the second snake run.

### *HYCAL Energy Calibration with $\pi^0 \rightarrow \gamma\gamma$ Decay*

Since the two “snake runs” were performed about one month apart, it is necessary to employ a different method to monitor the variations of the HYCAL gain factors over time. A light monitoring system (LMS) was built for this purpose. It was designed to shine light onto the HYCAL modules for a short time at the beginning of each run and record their responses. Unfortunately, this system couldn’t provide a sub-percent level accuracy. To solve this issue, a software calibration method was carried out using the  $\pi^0$  production data. Basically this method adjusts the gain factors of the HYCAL modules so that the two  $\gamma$  invariant mass  $m_{\gamma\gamma}$  matches the  $\pi^0$  mass. This calibration can be carried out run by run and will directly improve the resolution of the  $m_{\gamma\gamma}$ .

In this calibration step, the coincidence between the MOR trigger and the HYCAL trigger is required to reduce the accidental background. All the events with two or more clusters in HYCAL with energies ranging from 0.5 GeV to 8 GeV are selected. The two  $\gamma$  invariant masses are calculated for all possible  $\gamma\gamma$  pairs. The calculation is based on equation 4.2. The  $m_{\gamma\gamma}$  of each pair is then “assigned” to the central module of the cluster with greater energy. In this way an  $m_{\gamma\gamma}$  spectrum is constructed for every HYCAL module. An example is shown in Fig. 4.6. The invariant mass spectrum is then fitted by a function combined of a gaussian peak and a polynomial of second order.

The correction to the gain factor is defined as the ratio between the PDG  $\pi^0$  mass and the reconstructed  $m_{\gamma\gamma}$  from the fitting:

$$corr_{\pi^0} = \frac{m_{\pi^0(PDG)}}{m_{\pi^0(fitted)}}. \quad (4.11)$$

Since adjusting one HYCAL module will affect all other modules, the calibration was repeated for a few iterations. The correction factor for each module varies over time

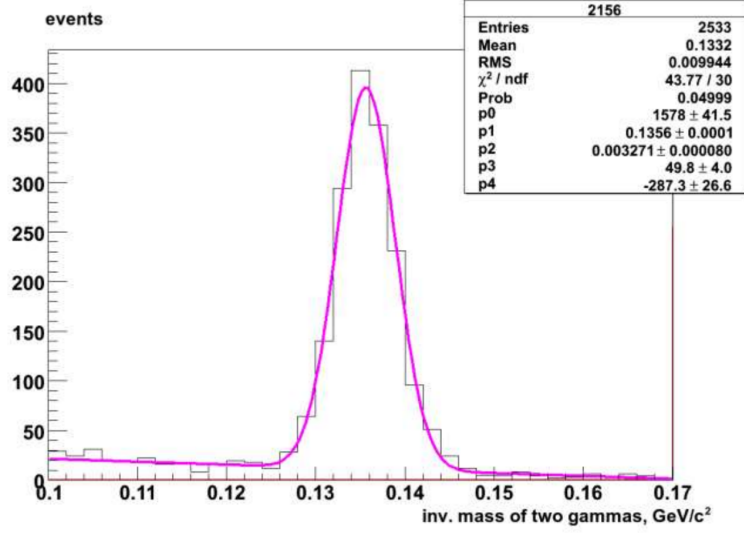


FIGURE 4.6: Example of the  $\pi^0 \rightarrow \gamma\gamma$  spectrum for  $PbWO_4$  module W1156 [32].

and usually converges after 3 to 4 iterations. After about ten iterations no further improvement can be achieved. Fig. 4.7 compares a few  $m_{\gamma\gamma}$  spectra before and after the iterative calibration procedure for different parts of HYCAL. The invariant mass resolution is improved by a factor of 10% - 15%.

The correction factors as a function of module numbers are shown in Fig. 4.8. Fig. 4.9 shows the distribution of the correction factors for all HYCAL modules.

#### 4.3.4 HYCAL Coordinate Alignment

The coordinates of the decay photons can be highly accurately determined by the HYCAL. However, all these coordinates are based on the HYCAL reference system. The alignment between the HYCAL reference system and the beam position is measured by JLab survey group before the experiment. Since the PrimEx-II experiment spanned more than one month, this stability of this alignment needs to be studied in the analysis.

The  $\pi^0$  production data is used in this study. The production angle  $\theta$  is projected

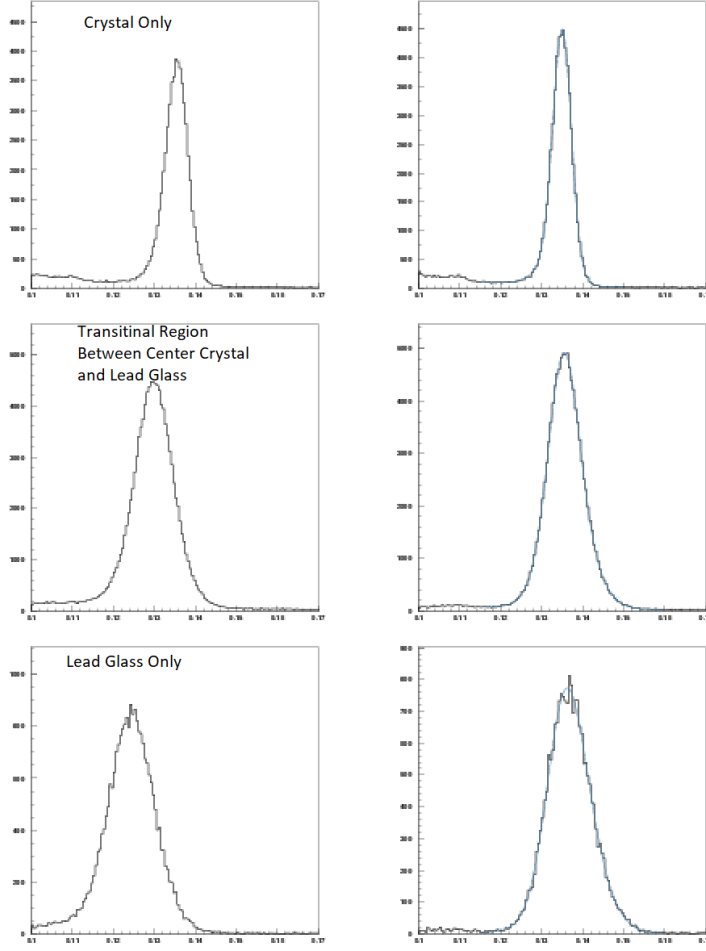


FIGURE 4.7: The  $m_{\gamma\gamma}$  invariant mass before and after the iterative calibration procedure for different parts of the HYCAL. The top plot is for the center  $\text{PbWO}_4$  crystal region, the bottom plot is for the lead glass region, and the middle plot is for the  $\text{PbWO}_4$  crystal modules on the boundary. The invariant mass resolution is improved by a factor of 10% - 15%.

to  $\theta_x$  and  $\theta_y$ :

$$\begin{aligned}
 \theta_{x,y} &= \arcsin\left(\frac{p_{x,y}}{p}\right) \\
 &= \arcsin\left(\frac{\frac{E_1 x_1 (\text{or } E_1 y_1)}{r_1} + \frac{E_2 x_2 (\text{or } E_2 y_2)}{r_2}}{E_1^2 + E_2^2 + 2E_1 E_2 \cos(\theta_{12})}\right),
 \end{aligned} \tag{4.12}$$

where  $r_{1,2} = \sqrt{x_{1,2}^2 + y_{1,2}^2 + z^2}$ . The projected angle  $\theta_{1,2}$  are calculated for every



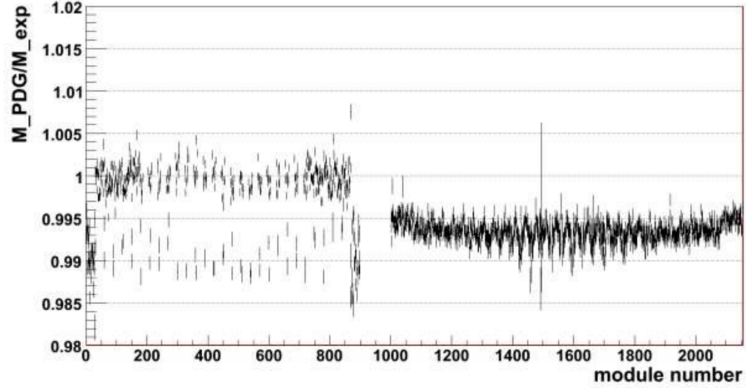


FIGURE 4.8: Calibration constant vs. module number for both crystal and glass using the  $\pi^0 \rightarrow \gamma\gamma$  invariant mass.

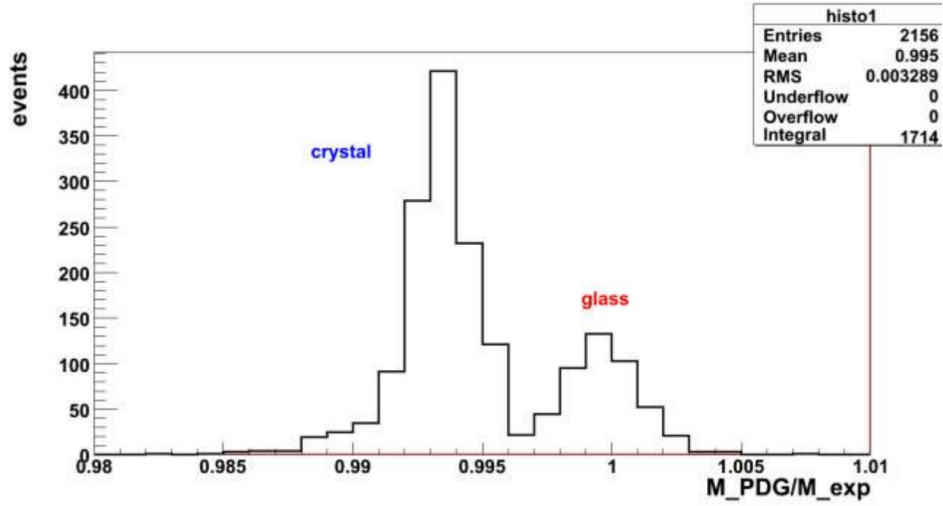


FIGURE 4.9: Calibration constant distribution for all modules.

event and the production runs are splitted into five run groups. Fig. 4.10 shows the distribution of  $\theta_x$  and  $\theta_y$  for one run group. Both  $\theta_x$  and  $\theta_y$  are symmetrical around  $0^\circ$ . The HYCAL misalignment can be calculated from the deviates of  $\theta_{x,y}$  from  $0^\circ$  following:

$$\Delta x, y = \Delta \theta_{x,y} \cdot Z. \quad (4.13)$$

The value of the misalignment  $\Delta x$  and  $\Delta y$  are stored in the PrimEx-II calibration database and used to correct the HYCAL reference system. The maximum misalign-

ment for x coordinate is 0.12 cm, and for y coordinate is -0.028 cm.

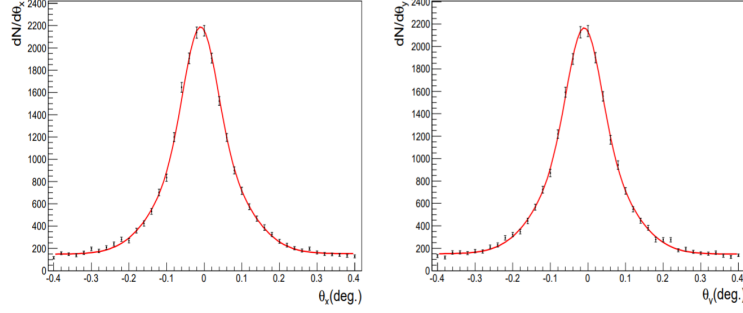


FIGURE 4.10: The distribution of  $\theta_x$  and  $\theta_y$  for one run group. Both  $\theta_x$  and  $\theta_y$  are symmetrical around  $0^\circ$ . The misalignment  $\Delta x$  and  $\Delta y$  are calculated from the peak deviation. [33]

#### 4.3.5 HYCAL Trigger Timing Alignment

The time difference between the signals of the MOR trigger and the HYCAL trigger, or the so called Tdiff, is used as an important parameter in the analysis. A coincidence peak is observed when the number of events is drawn as a function of Tdiff as shown in Fig. 4.11. A cut to this value based on the resolution of the peak is utilized to exclude the off time beam photons. In case of events with beam photon multiplicity, the beam photon with the value of Tdiff closest to the peak position is selected. This is called the “best Tdiff” method. For more details regarding the beam photon multiplicity and the “best Tdiff” method, please refer to section 4.6.2. All in all, improving the precision of the event timing, *i.e.*, Tdiff, is critical for the beam photon selection.

Since the Tdiff defined above is calculated without knowing any of the underlying HYCAL module, adding information from individual HYCAL modules may improve the precision of the Tdiff. One way to achieve this is to use the individual HYCAL TDC. However, a lot of these TDC’s didn’t work properly during the PrimEx-II experiment. An alternative method explores the relation between the signal speed

and the energy deposition of a HYCAL module. As shown in Fig. 4.12, the signal speed is faster with greater energy deposition. The MOR is a faster trigger than the HYCAL trigger, and the HYCAL is triggered whenever the total sum of the energy deposition exceeds 2.5 GeV, therefore the value of the Tdiff largely depends on the speed of the HYCAL module with the largest energy deposition. In order to take advantage of this effect, the Tdiff is “assigned” to the HYCAL module with the greatest energy deposition in an event. As a result, now each HYCAL module has its own Tdiff spectrum, and an alignment offset can be calculated from it.

The  $\pi^0$  analysis will especially benefit from this calibration since we are only interested in the elastic  $\pi^0$  and the decay photons from elastic  $\pi^0$ s tend to have larger energy. In the  $\pi^0$  reconstruction, the value of Tdiff for a  $\pi^0$  candidate is corrected by adding the HYCAL alignment offset of the central module from the HYCAL cluster with higher energy. Fig. 4.13 shows the comparison of the distributions of Tdiff calculated with and without the HYCAL timing alignment for elastic  $\pi^0$ s during the silicon runs. The Tdiff peak resolution is improved from 1.5 - 1.7 ns to 0.8 - 0.95 ns.

## 4.4 Tagged Photon Flux Determination

### 4.4.1 Tagged Electron Accounting

As shown in equation 4.1 in the beginning of this chapter, the normalization of the  $\pi^0$  photoproduction cross section directly depends on the determination of the tagged photon flux on the target. The tagged photon flux on the target can be obtained using equation 3.2. The measurement of the absolute tagging ratio  $R_{absolute}$  is already discussed in section 3.6. In this section the method to determine the number of tagged electrons on a particular E or T channel,  $N_e^i$  will be introduced.

For most experiments at JLab involving tagged photons, the photon rates are usually higher than the capacity of the data acquisition system (DAQ). In the PrimEx-II experiment, the rate of the tagged photons is determined by sampling for a small

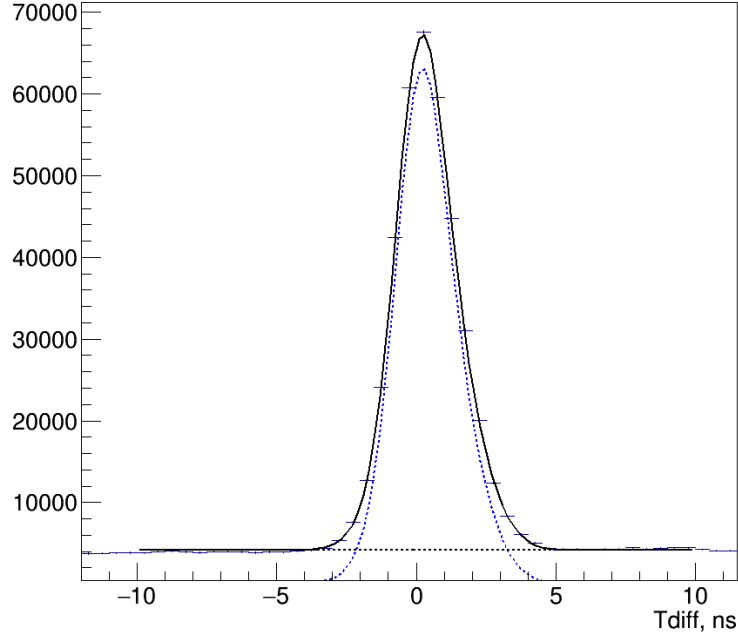


FIGURE 4.11: Number of events as a function of Tdiff for the silicon target obtained by the “best Tdiff” method. The fit to the distribution is performed with a function consisting of a double gaussian and a linear background. The timing resolution is calculated to be 1.2 ns from the fitting parameters.

fraction of time over the whole period of the experiment. This rate can be extrapolated to all time to calculate the total number of the tagged photons, *i.e.*, the flux, in a given data sample. The tagger TDC is used to determine the tagged photon rate. The TDC installed in the tagger during the PrimEx experiments was the LRS1877 type. This is a multiple hit TDC with the capacity of storing up to 16 hits per channel in a LIFO (Last In First Out) mode with a maximum range of 32  $\mu s$ . If the rate is too high, the older hits are overwritten by the more recent ones due to the LIFO limit. In PrimEx the TDC was set to 16  $\mu s$  and 10 hits. For the flux calculation purpose the prescaled clock triggers are used as the TDC common stop because it is not correlated to the beam intensity. Fig. 4.14 shows a typical timing spectrum reconstructed for a single T-channel taken with clock triggers. The drop off of the spectrum at the right tail is due to the TDC LIFO limit. A time window

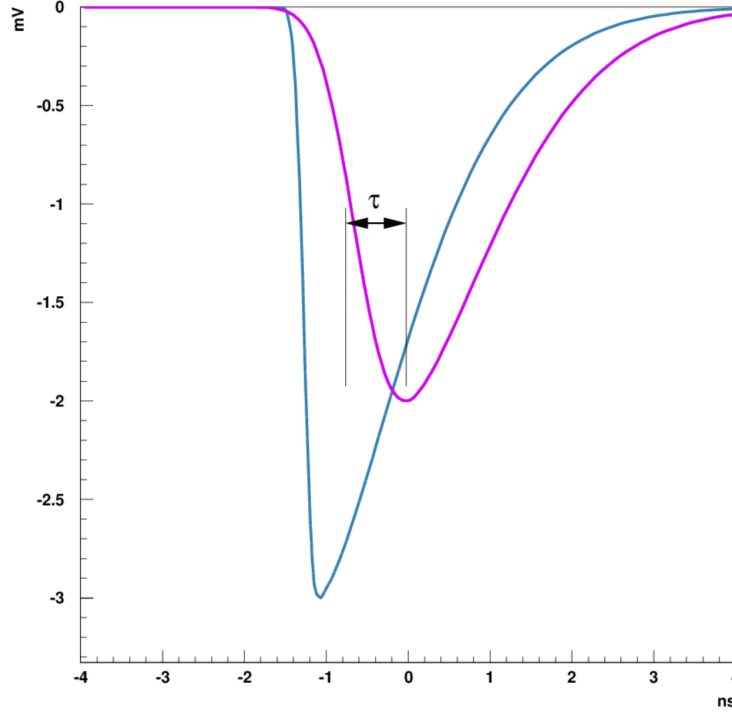


FIGURE 4.12: Two different signals from the same HYCAL module. The signal from greater energy deposition is faster.

$\omega$  is used to count the number of TDC hits. The photon rate can be calculated by:

$$r_i = \frac{n_{e,i}}{\omega \cdot n_{trigger}}, \quad (4.14)$$

where  $r_i$  is the tagged photon rate detected by the  $i^{th}$  T-channel,  $n_{e,i}$  is the number of tagged electrons incident on the T-channel and  $n_{trigger}$  is the number of triggers within the time window  $\omega$ . In PrimEx-II  $\omega = 2\mu s$ .

The JLab DAQ system has two dedicated scalers to measure the live-time of the DAQ. Both scalers are driven by the clock trigger. One of the scalers is live-time gated and the other is not. The live-time of the DAQ system,  $T_{live}$ , can be calculated by:

$$T_{live} = n_{gated} \cdot \beta, \quad (4.15)$$

where  $n_{gated}$  is the number of gated scaler counts and  $\beta = \frac{1}{clock \ frequency}$ . Since we are

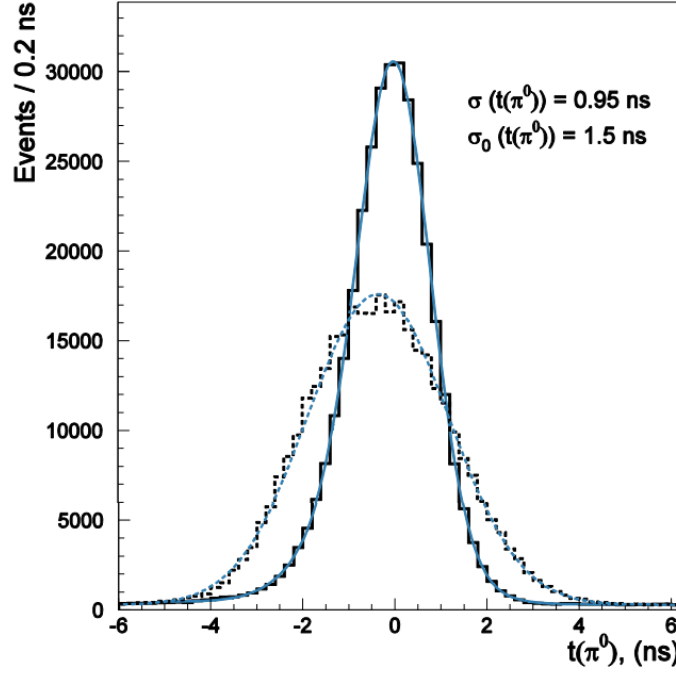


FIGURE 4.13: The comparison of the distributions of Tdiff calculated with and without the HYCAL timing alignment for the silicon target. The Tdiff peak resolution is improved from 1.5 - 1.7 ns to 0.8 - 0.95 ns. The figure is only for elastic  $\pi^0$ s.

only interested in the flux during the DAQ live-time, the total number of electrons incident on the  $i^{th}$  T-channel is:

$$\begin{aligned}
 N_e^i &= r_i \cdot T_{live} \\
 &= \frac{n_{e,i}}{\omega \cdot n_{trigger}} \cdot n_{gated} \cdot \beta.
 \end{aligned} \tag{4.16}$$

According to equation 3.2, the number of tagged photons  $N_{\gamma,i}^{tagged}$  for the  $i^{th}$  T-channel is given by:

$$\begin{aligned}
 N_{\gamma,i}^{tagged} &= N_e^i \cdot R_{absolute}^i \\
 &= \frac{n_{e,i}}{\omega \cdot n_{trigger}} \cdot n_{gated} \cdot \beta \cdot R_{absolute}^i.
 \end{aligned} \tag{4.17}$$

Since the tagged photon rate is sampled at a fixed frequency and has to be

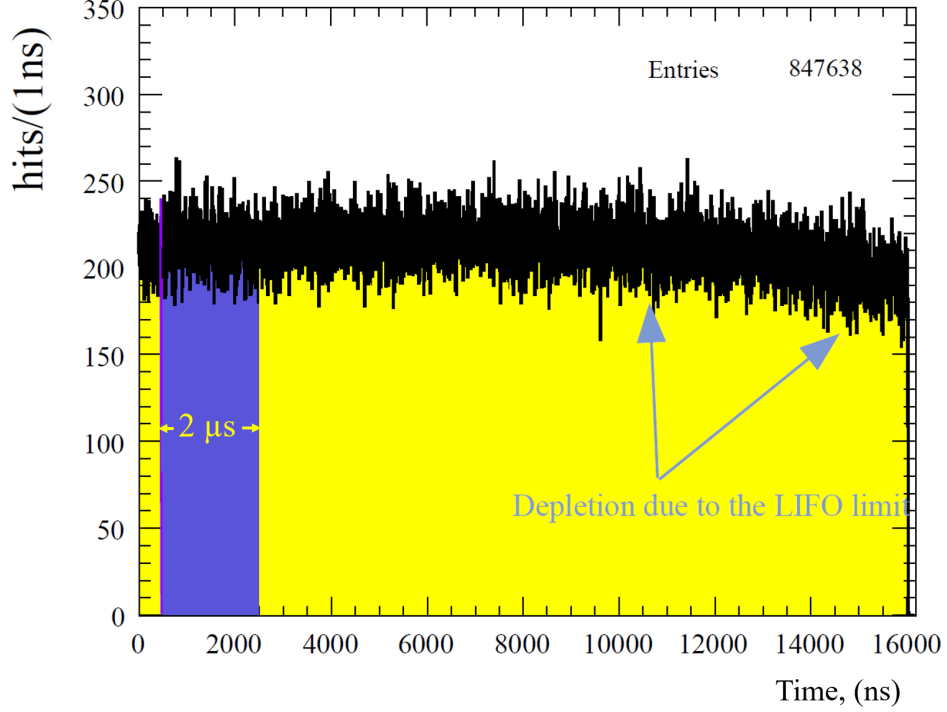


FIGURE 4.14: A typical timing spectrum for a single T-channel taken with clock triggers from the PrimEx experiment. The drop off of the spectrum at the right tail is due to the TDC LIFO limit so that earlier hits are overwritten. The time window  $\omega$  used here is  $7 \mu s$ .

extrapolated to calculate the photon flux for a whole data sample, any abrupt change in the beam current would make the flux calculated unreliable. The uncontrolled variations of the beam current, *i.e.*, beam trips, must be removed. The details of the beam trip accounting will be discussed in section 4.4.2.

#### 4.4.2 Beam Trip Accounting

Any uncontrolled variations of the beam current are called beam trips. As discussed in section 4.4.1, beam trips as well as the  $\pi^0$  events occur in the beam trips must be identified and removed in the data analysis. Because the live-time of the DAQ system is negatively correlated with the beam intensity, the beam trip can be determined by checking the ratio of the live-time and the real time (the fractional live-time). The

JLab DAQ system has two dedicated scalers to measure the live-time of the DAQ. One of the scalers is live-time gated, and the other is free running. Both scalers are driven by the clock trigger. The scalers are read out in every event. The fractional live time for event  $k$  can be obtained by:

$$R_{live-time} = \frac{n_{gated}^k - n_{gated}^{k-1}}{n_{free}^k - n_{free}^{k-1}}, \quad (4.18)$$

where  $n_{gated}^k$  is the readout of the live-time gated scaler at the  $k^{th}$  event, and  $n_{free}^k$  is the readout of the free running scaler at the  $k^{th}$  event. The fractional live-time  $R_{live-time}$  is always smaller than one under normal beam current condition. In the analysis, the  $R_{live-time}$  is calculated for every five second interval. Fig. 4.15 shows a typical distribution of the  $R_{live-time}$  in a production run. The fractional live-time for most of the events are centered around 0.96, with exceptions when beam trips occur. For each run, the  $R_{live-time}$  distribution is fitted with a gaussian function to find the nominal value and the standard deviation  $\sigma$ . Any five second interval with a  $R_{live-time}$  outside of the  $\pm m \cdot \sigma$  is discarded, where  $m$  is a parameter and can be optimized.

#### 4.4.3 Summary

The total number of tagged photons  $N_{\gamma,i}^{tagged}$  for the  $i^{th}$  T-channel can be calculated by summing over all the valid five second intervals:

$$\begin{aligned} N_{\gamma,i}^{tagged} &= \sum_{id} N_{\gamma,i,id}^{tagged} \\ &= R_{absolute}^i \cdot \sum_{id} N_{e,i,id}^{tagged} \\ &= R_{absolute}^i \cdot \sum_{id} (r_i \cdot T_{live})_{id}, \end{aligned} \quad (4.19)$$

where  $id$  identifies the valid five second interval.



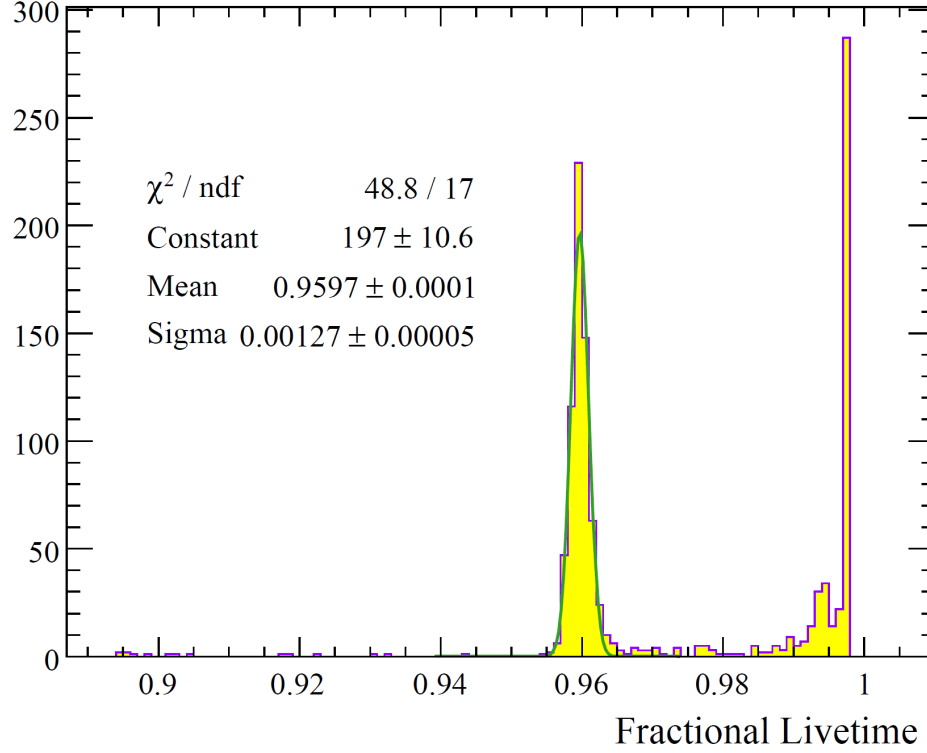


FIGURE 4.15: A typical distribution of the  $R_{live-time}$  in a run. The  $R_{live-time}$  is calculated for every five second interval. The fractional live-time for most of the events are centered around 0.96, some has a fractional live-time near one when the beam current is dropped, and very few has a fractional live-time smaller than 0.95 when the beam current is increased abruptly.

## 4.5 Event Selection

In the PrimEx-II experiment, the DAQ system was triggered when either a MOR signal or a HYCAL trigger signal was received. This is an improvement over the PrimEx-I experiment, which used a hardware coincidence to trigger the DAQ. In the  $\pi^0$  analysis of the PrimEx-II experiment, the event selection is based on the software coincidence of the MOR and the HYCAL trigger. A Tdiff cut is applied to ensure this coincidence. The calculation of the Tdiff follows the method described in section 4.3.5. The Tdiff distribution is shown in Fig. 4.11. The window of the Tdiff cut applied in the analysis is  $[-7, 7]$  ns, which is about  $\pm 5\sigma$ . An event is discarded

if there is no tagged photon within this window. In some events there are multiple tagged photons within the Tdiff window. The tagged photon multiplicity is shown in Fig. 4.16. For all the events with tagged photons, about 34% show multiplicity. For the events showing tagged photon multiplicity, there are two methods for the beam photon selection. The first method is the so called “all Tdiff” method. This method considers all the tagged photons as beam photon candidates, leaving them to be excluded at later stages. The second method only selects the tagged photon whose value of the Tdiff is the closest to the peak position in Fig. 4.11. This method is the so called “best Tdiff” method. The  $\gamma\gamma$  invariant mass  $m_{\gamma\gamma}$  distributions extracted using the “best Tdiff” method and the “all Tdiff” method are drawn together in Fig. 4.17. The  $m_{\gamma\gamma}$  signal peaks from the “best Tdiff” method and the “all Tdiff” method are almost the same, indicating that most of the extra photons selected by the “all Tdiff” method are accidentals. Therefore, in this analysis the “best Tdiff” method will be used. The “best Tdiff” method may select the wrong beam candidate. The correction to this effect will be discussed in section 4.6.2.

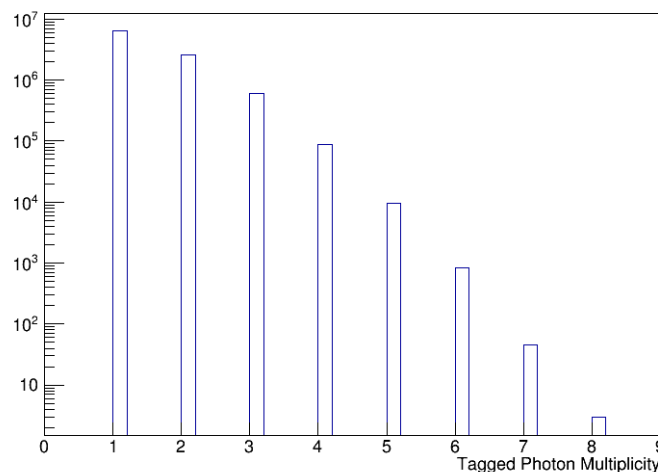


FIGURE 4.16: Tagged photon multiplicity for the silicon target. For all the events with tagged photons, about 34% show multiplicity.

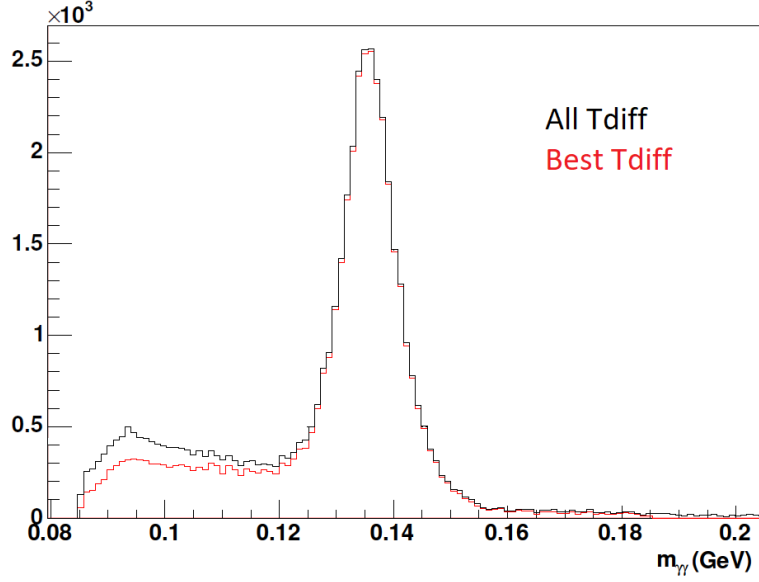


FIGURE 4.17: The  $\gamma\gamma$  invariant mass  $m_{\gamma\gamma}$  distributions extracted using the “best Tdiff” method and the “all Tdiff” method are drawn together. Although tagged photon multiplicity exists in about 34% of the events, the  $m_{\gamma\gamma}$  signal peaks from the “best Tdiff” method and the “all Tdiff” method are almost the same, indicating that most of the extra photons are accidentals.

Since we aim to obtain the cross section of the  $2\gamma$  decay channel, only events with two or more HYCAL clusters are selected, with the energy of every cluster greater than 0.5 GeV. All the clusters in one event are combined into two cluster pairs. The total energy of a single cluster pair falls within the window of  $[3, 8]$  GeV. All the pairs surviving the above cuts are considered to be decay photon pairs. There are tungsten blocks covering one layer of HYCAL module around the central hole. HYCAL clusters on these modules are excluded from the analysis. The HYCAL glass modules are also excluded from the calculation of the  $\pi^0$  decay width due to their poor energy and position resolutions. However, these modules will be included to extract the  $\pi^0$  photoproduction yield on the silicon target at large angles ( $> 2.5^\circ$ ).

The cuts introduced above are subject to systematic error studies. The selected HYCAL two cluster pairs and the beam candidate that passed these cuts are further

combined to form a  $\pi^0$  candidate. The procedure to extract the number of the elastic  $\pi^0$ s will be discussed in section 4.6.

## 4.6 Yield Extraction

### 4.6.1 The “Hybrid Mass”

Two important variables to select the elastic  $\pi^0$ s are the  $\gamma\gamma$  invariant mass  $m_{\gamma\gamma}$  and the elasticity of the  $\pi^0$  candidate. A real  $\pi^0 \rightarrow \gamma\gamma$  event has the same  $\gamma\gamma$  invariant mass as the  $\pi^0$  mass, and we are only interested in elastic events since the momentum transferred from the beam photon to the nucleus in the Primakoff process is negligible, given HYCAL’s  $\sim 100$  MeV energy resolution. Two plots in Fig. 4.18 show the  $\pi^0$  yields as a function of  $\gamma\gamma$  invariant mass and the elasticity. These two variables can be calculated following equation 4.2 and equation 4.4 respectively. The  $\gamma\gamma$  invariant mass  $m_{\gamma\gamma}$  can also be expressed by the opening angle of the two decay photons  $\theta_{12}$ :

$$\sqrt{2E_1E_2(1 - \cos(\theta_{12}))}, \quad (4.20)$$

where  $E_1$  and  $E_2$  are the HYCAL cluster energies. The opening angle  $\theta_{12}$  can be calculated by the following equation:

$$\cos \theta_{12} = \frac{x_1x_2 + y_1y_2 + z^2}{\sqrt{(x_1^2 + y_1^2 + z^2)(x_2^2 + y_2^2 + z^2)}}, \quad (4.21)$$

where  $x_1, x_2, y_1, y_2$  are the coordinates on the HYCAL surface, and  $z$  is the distance between the HYCAL crystal surface and the target, which is 702 cm silicon and 701.2 cm for carbon. The value of  $z$  for lead glass modules is 10 cm smaller than crystal modules.

Fig. 4.19 illustrates the  $\pi^0$  population on the two dimensional surface formed by  $\frac{m_{\gamma\gamma}}{m_{\pi^0}}$  and the elasticity. The  $\gamma\gamma$  invariant mass is normalized by the PDG value of the  $m_{\pi^0}$ , so that it has the same scale as the elasticity. Apparently the real  $\pi^0$ s are

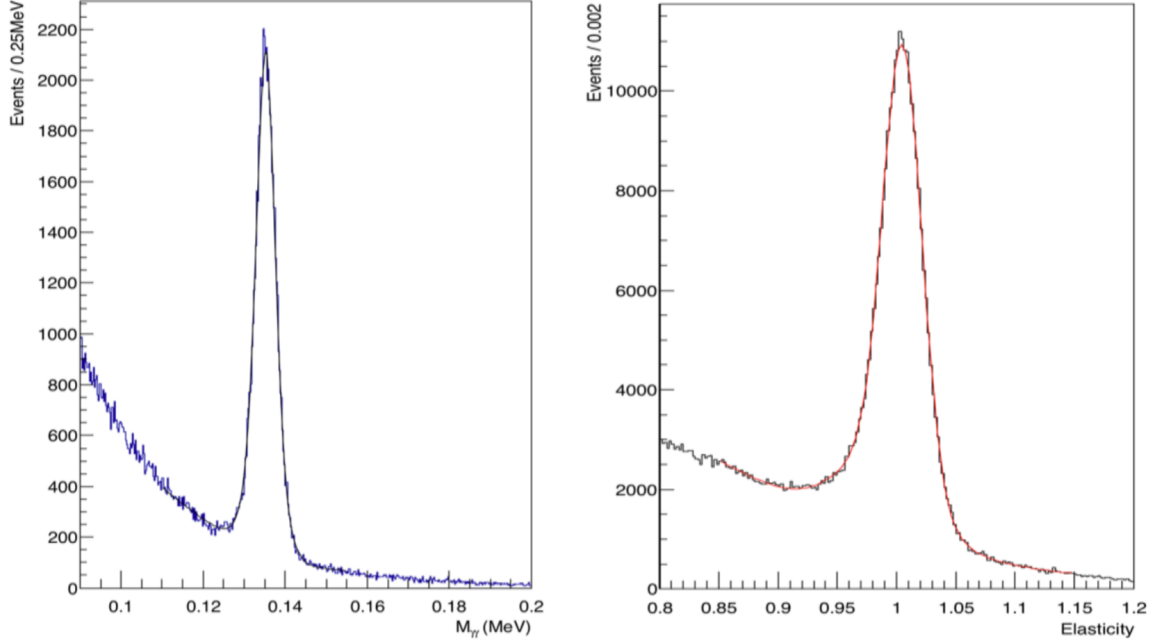


FIGURE 4.18: The distribution of  $\gamma\gamma$  invariant mass  $m_{\gamma\gamma}$  and elasticity for the silicon target.

populated inside the “ellipse” around  $\frac{m_{\gamma\gamma}}{m_{\pi^0}} = 1$  and the  $\frac{E_1+E_2}{E_{beam}} = 1$ . The  $m_{\gamma\gamma}$  and the elasticity are highly correlated. The longer axis of the “ellipse” and the horizontal axis form an angle  $\alpha$ . Assuming  $E_1$  and  $E_2$  are the real energies of the two decay  $\gamma$ s, and  $E_1 + \Delta E_1$  and  $E_2 + \Delta E_2$  are the energies detected by HYCAL, this correlation can be illustrated using the following equation:

$$\begin{aligned}
 m_{\gamma\gamma HYCAL} &= \sqrt{2(E_1 + \Delta E_1)(E_2 + \Delta E_2)(1 - \cos(\theta))} \\
 &\approx \sqrt{2E_1 E_2 (1 - \cos(\theta))} \sqrt{1 + \frac{\Delta E_1}{E_1} + \frac{\Delta E_2}{E_2}}
 \end{aligned} \tag{4.22}$$

$$\begin{aligned}
 &\approx m_{\pi^0} \left[ 1 + \frac{1}{2} \left( \frac{\Delta E_1}{E_1} + \frac{\Delta E_2}{E_2} \right) \right], \\
 Elasticity_{HYCAL} &= \frac{E_1 + \Delta E_1 + E_2 + \Delta E_2}{E_1 + E_2} \\
 &= 1 + \frac{\Delta E_1 + \Delta E_2}{E_1 + E_2}.
 \end{aligned} \tag{4.23}$$

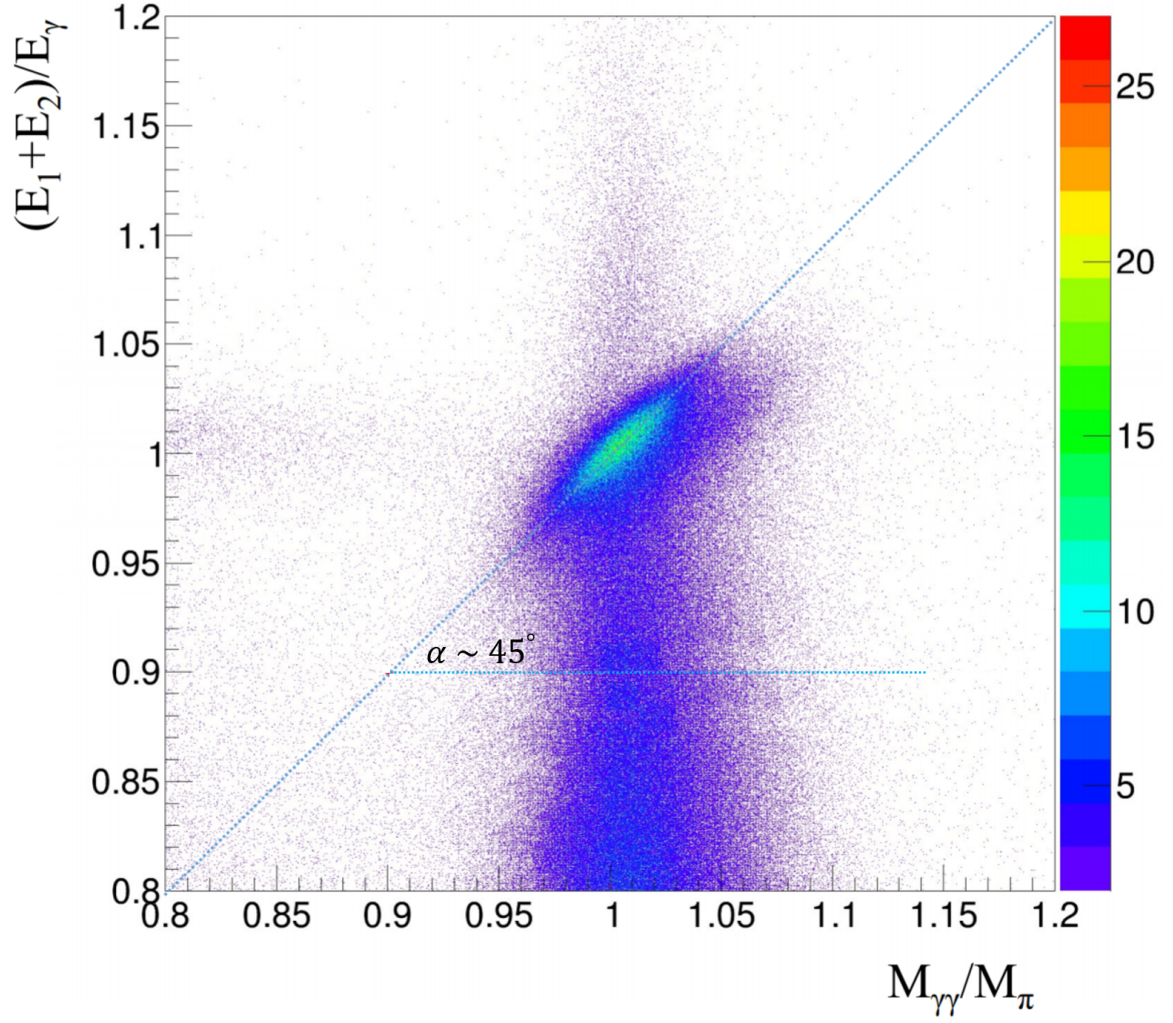


FIGURE 4.19: Elasticity vs.  $\frac{m_{\gamma\gamma}}{m_{\pi^0}}$ . Clearly the region inside the “ellipse” around  $\frac{m_{\gamma\gamma}}{m_{\pi^0}} = 1$  and the  $\frac{E_1+E_2}{E_{beam}} = 1$  is where the real  $\pi^0$ s are distributed. What’s more, the  $m_{\gamma\gamma}$  and the elasticity are highly correlated for a real  $\pi^0$ .

Considering the case when  $E_1$  equals  $E_2$ , one has  $\frac{\Delta E_1}{E_1} = \frac{\Delta E_2}{E_2} = \frac{\Delta E_1 + \Delta E_2}{E_1 + E_2}$ . Applying this relation to equation 4.22 and equation 4.23, one would have  $\frac{m_{\gamma\gamma}^{HYCAL}}{m_{\pi^0}^0} = Elasticity_{HYCAL}$ . According to Fig. 3.15, the HYCAL energy resolution increases from  $\sim 1\%$  to  $\sim 2\%$  when the deposited energy decreases from  $\sim 5$  GeV to  $\sim 1$  GeV. Simple calculations show that the difference between the values of  $Elasticity_{HYCAL}$  and  $m_{\gamma\gamma}^{HYCAL}$  are about 0.01 to 0.02. This correlation between the elasticity and the

value of  $\frac{m_{\gamma\gamma}}{m_{\pi^0}}$  explains why the elastic  $\pi^0$ s are all distributed in a long and thin “ellipse”.

As shown in Fig. 4.19, the background events are distributed mainly in two bands: the events in the horizontal band where  $\frac{E_1+E_2}{E_{beam}} = 1$ , and the vertical band where the  $m_{\gamma\gamma}/m_{\pi^0} = 1$ . These two bands join together under the “ellipse”, the signal region. The events inside the horizontal band are non  $\pi^0$  events, since the invariant masses  $m_{\gamma\gamma}$  deviates from the  $\pi^0$  mass. The events inside the vertical band are mainly timing accidental events, when another tagged photon with different energy is misidentified as the incident photon. These events can also be other physical processes producing more particles other than the two detected photons.

In order to effectively separate the real  $\pi^0$  events from the background, a line that is orthogonal to the longer axis of the “ellipse” is defined and all data is projected onto this new axis. The projected distribution is the so called “hybrid mass” and can be expressed by equation:

$$hybridmass = \frac{m_{\gamma\gamma}}{m_{\pi^0}} \cos(\alpha) - Elasticity \sin(\alpha). \quad (4.24)$$

In the analysis  $\alpha = 45^\circ$  is used since in general  $\frac{m_{\gamma\gamma}}{m_{\pi^0}} \sim Elasticity$ .

Compared to the invariant mass and the elasticity, the signal of the “hybrid mass” not only displays a much better resolution as shown in Fig. 4.20, but it also pushes the background away from the peak, which benefits the background fitting.

#### 4.6.2 Accidental Sidebands Subtraction and Tdiff Cut efficiency

As shown in Fig. 4.11, there are accidental backgrounds lying under the Tdiff peak within the Tdiff cut window. These accidentals must be carefully removed. Assuming the accidentals within the Tdiff cut window shares the same structure as the accidentals outside of the window, one can subtract the timing accidental background under the Tdiff peak using the timing sidebands to the left and the right of the Tdiff peak, as shown in Fig. 4.21. In the analysis, events with the Tdiff values

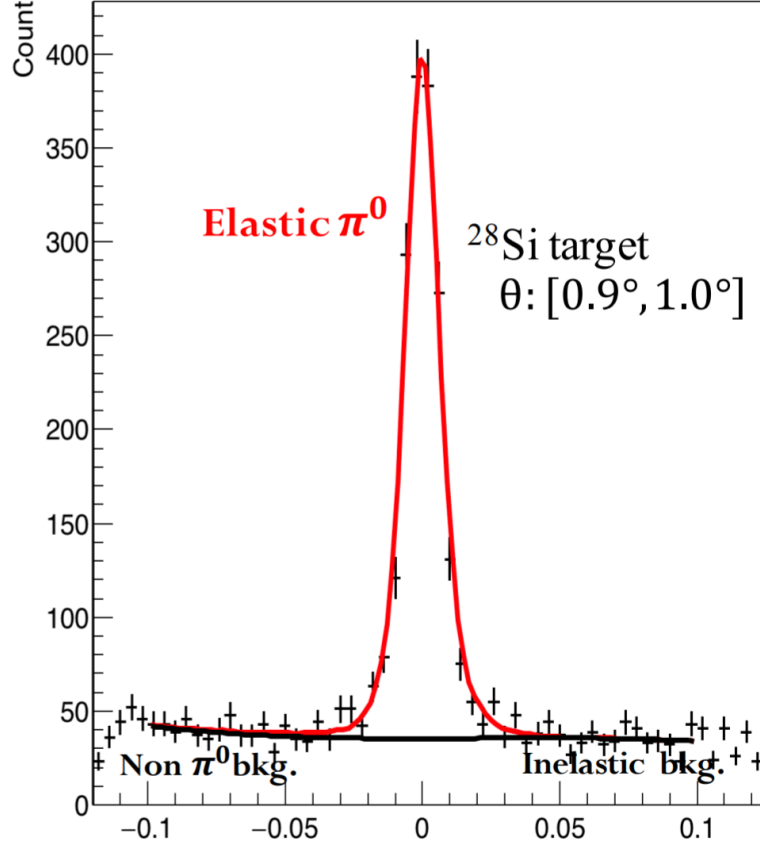


FIGURE 4.20: The “hybrid mass” distribution for the silicon target in angular bin  $[0.9^\circ, 1.0^\circ]$ .

between -12 to -7 ns and 7 to 21 ns are reconstructed and used as the timing sidebands. The Tdiff window is  $[-7, 7]$  ns in the analysis, which is about  $10\sigma$  wide. In spite of a wide coincidence window, there is still the possibility that some  $\pi^0$  events are excluded. Moreover, these excluded  $\pi^0$  events are actually in the accidental sidebands and will be subtracted. Therefore, an efficiency factor called Tdiff efficiency must be estimated. In order to calculate this number, the Tdiff spectrum is fitted by a function consisting of a double gaussian and a linear background, as shown in Fig. 4.11. Integrating the tails of the double gaussian within the sidebands, one can obtain the number of the excluded  $\pi^0$  events  $N_{\pi^0}^{excluded}$ . The number of the signal  $N_s$ , the accidental background  $N_{acc}$ , and the events in the sidebands  $N_{side}$  can also



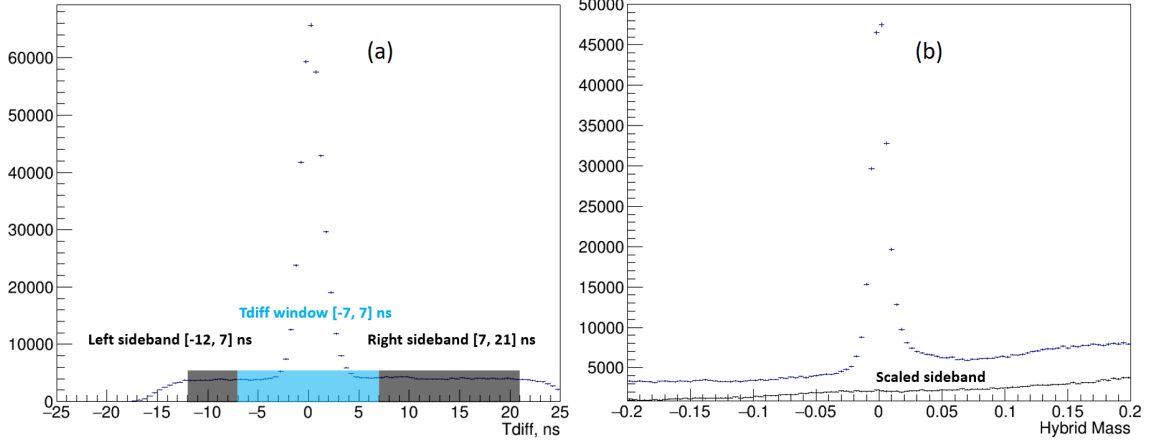


FIGURE 4.21: Left plot shows number of events as a function of Tdiff. The sidebands are inside the black box, and the Tdiff window is inside the blue box. The blue histogram in the right plot shows the number of events as a function of “hybrid mass”. The black histogram in the same plot shows the events from the sidebands. The accidentals possess no structure under the peak.

be estimated from this fitting. In order to subtract  $N_{acc}$  events using the sidebands, a scale factor  $r = \frac{N_{acc}}{N_{side} - N_{\pi^0}^{excluded}}$  must be applied to the sidebands. Therefore, the reduced number of  $\pi^0$ s due to the Tdiff cut and the sidebands subtraction is:

$$N_{reduced} = (1 + r) \cdot N_{\pi^0}^{excluded}. \quad (4.25)$$

And the Tdiff cut efficiency is  $\epsilon_{reduced} = \frac{N_{reduced}}{N_s}$ . For silicon target, the value of the tdiff cut efficiency is 0.998, and the carbon it is 0.993. A summary of all the components of the experimental efficiencies are listed in table 4.1.

#### 4.6.3 The “Hybrid Mass” Fitting and the $\pi^0$ Yields Determination

Since the  $\pi^0$  photoproduction yield over the  $\theta$  angle is needed, the data is divided into small  $\theta$  bins. For the final result  $\Delta\theta = 0.02^\circ$  binning is used, but other binning options are also studied and will be discussed in chapter 5. The “hybrid mass” distribution is populated within each bin. The signal and background were separated by fitting this distribution.

In the analysis, the shape of the signal is obtained from Monte Carlo simulation. The simulated “data” is binned in the same fashion as the real data and the “hybrid mass” distributions are generated, which provide the shape to fit the signals 4.22. For the background a piecewise function consists of a second order and a third order

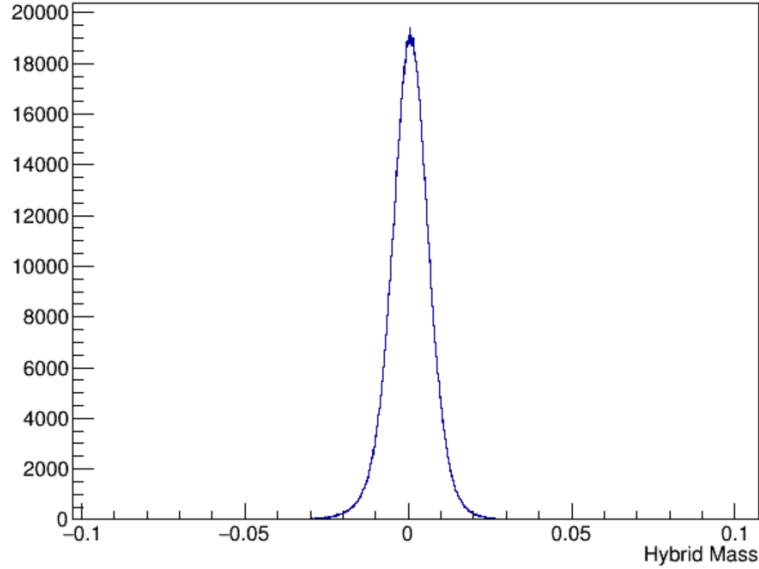


FIGURE 4.22: The number of Monte Carlo events as a function of “hybrid mass”, which provides the shape of the signal for the “hybrid mass” fitting.

polynomial is used in the fitting. Second order polynomials and third order polynomials are also tested to study the systematic errors from different fitting functions. The timing accidental background is removed by subtracting the timing sidebands, which has already been discussed in section 4.6.2. The  $\omega$  photoproduction gives rise to significant background off the “hybrid mass” peak. It mainly arises from the  $\omega \rightarrow \pi^0 \gamma$  decay, since in this channel the  $\pi^0$  may carry the most part of the initial energy. The  $\omega$  background was studied by Monte Carlo [34, 35]. The “hybrid mass” spectra of the simulated  $\omega \rightarrow \pi^0 \gamma$  decay events are subtracted to remove the  $\omega$  background. The systematic error studies due to the  $\omega$  background will be discussed in chapter 5. In summary, the fitting function of the “hybrid mass” distribution has

the form of:

$$fit = N_{\pi^0} \cdot MC_{peak} + MC_{\omega} + accidental_{sideband} + \\ accidental_{\text{"besttdiff"}} + background_{poly}, \quad (4.26)$$

where the  $N_{\pi^0}$  is the number of  $\pi^0$ s from the fitting,  $MC_{peak}$  is the unit amplitude from the Monte Carlo used to fit the signal,  $MC_{\omega}$  is scaled by flux and used for the  $\omega$  background subtraction, the  $accidental_{sideband}$  represents the sideband subtraction, the  $accidental_{\text{"besttdiff"}}$  represents the accidentals caused by “best tdiff” beam photon selection, which will be discussed in section 4.6.4, and the  $background_{poly}$  is the term for the polynomial background.

The known background sources, the timing accidental background and the  $\omega$  background are subtracted directly from the “hybrid mass” distribution.

Fig. 4.23 shows six fitting samples of the “hybrid mass” distribution. Two methods to calculate the  $\pi^0$  yields from the fitting were attempted. The first method takes the  $N_{\pi^0}$  from equation 4.26 directly. In the second method, the number of  $\pi^0$ s is calculated by subtracting the background from the total counts of the “hybrid mass” over a fixed range. In the analysis this range is  $[-0.1, 0.1]$  in “hybrid mass” unit, which is 1. The yield obtained from this procedure needs to be corrected because of the limited integration range. This correction can be estimated by using the Monte Carlo simulated distribution of the “hybrid mass”. Both methods were performed and their difference is small. The comparison of these two methods will be presented in chapter 5.

#### 4.6.4 “Best Tdiff” Correction

There is a small chance that a photon beam candidate is not the photon with the “best Tdiff”, but the photon with the second “best Tdiff”. In other words, a misidentification can happen when using the “best Tdiff” method. This is illustrated in Fig. 4.24. In this figure the  $\pi^0$ s are reconstructed with “beam photons” selected by

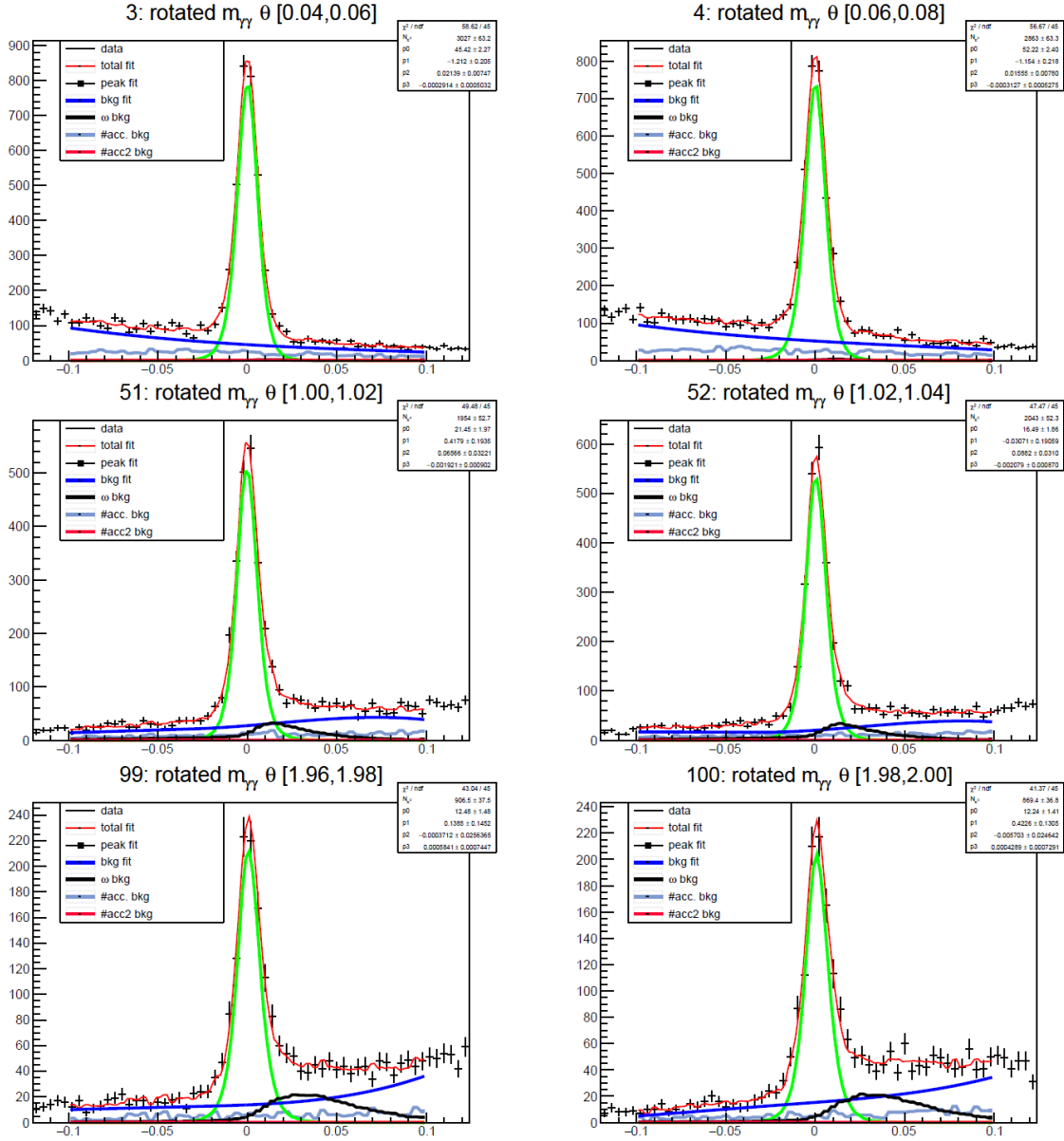


FIGURE 4.23: Six fitting samples of the “hybrid mass” distribution for the silicon target. The top figures show fittings in the Primakoff region, the middle figures show fittings in the nuclear coherent region, and the bottom figure show fittings at relatively large angles.

the second “best Tdiff”, and the  $\pi^0$  yield is plotted as a function of the “hybrid mass”. A small peak can be seen sitting on top of a much wider gaussian shape background. Clearly the  $\pi^0$  candidates under this peak are signals misidentified as

accidental background using the “best Tdiff” method. In order to obtain the correct  $\pi^0$  photoproduction yield, the number of  $\pi^0$ s excluded due to this effect needs to be estimated. In the analysis, a correction factor is calculated by taking the ratio between the counts of the  $\pi^0$ s with the second “best tdiff” and the counts with the first “best tdiff”. There are about one hundred signals shown in the third “best Tdiff” distribution. These signals can be safely ignored since they have little effect as the total number of  $\pi^0$ s exceeds  $10^6$ . They add about 0.01% to the systematic uncertainties. Another issue arises from this misidentification is that the same number of the beam photon candidates that are considered as “real” signals are actually accidental background. They need to be subtracted from the  $\pi^0$  “hybrid mass” distribution. The “hybrid mass” distribution of these accidentals takes the same shape as the accidentals shown in Fig. 4.24. They can easily be subtracted by adding their distributions as a background term in the “hybrid mass” fitting as shown in equation 4.26. Although the total number of these accidentals accounts for 1-2% of all events, the  $\sigma$ s of their distributions are so large compared with the real  $\pi^0$  peak that this subtraction gives little effect on the number of  $\pi^0$ s from the “hybrid mass” fitting. Thus, the effect of the “best tdiff” correction is adding about 1-2%  $\pi^0$ s to the  $\pi^0$  photoproduction yields. To be exact, the “best tdiff” correction increases the yields by 1.16% for the silicon target, and 1.45% for the carbon target. Instead of directly correcting the  $\pi^0$  yields, in the analysis, this number is included in the calculation of the efficiency  $\epsilon$  as in equation 4.1.

#### 4.6.5 *Extracted yields of $\pi^0 \rightarrow \gamma\gamma$ coherent photoproduction*

Using the methods discussed in the previous sections, the  $\pi^0 \rightarrow \gamma\gamma$  yields for both silicon target and the carbon target are extracted. Fig. 4.25 (a) shows the silicon yield, and (b) shows the carbon yield. Both yields are extracted with only the  $\text{PbWO}_4$  acceptance. The Primakoff peak for the silicon target is more pronounced compared

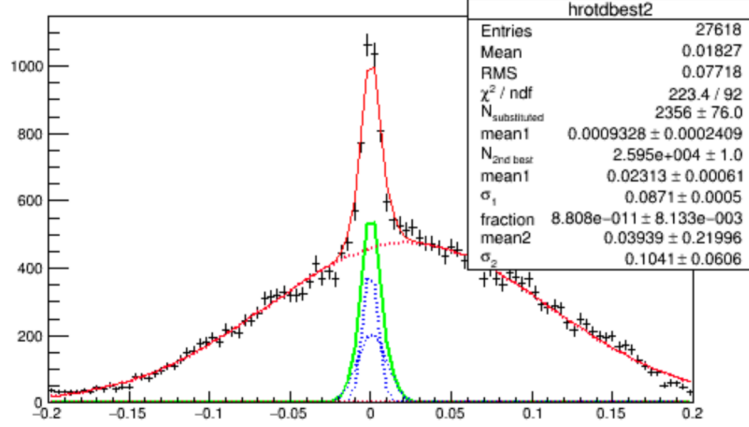


FIGURE 4.24: The “hybrid mass” distributions of the  $\pi^0$  candidates with the second “best tdiff”. A small peak can be seen sitting on top of a much wider gaussian shape background. These  $\pi^0$  candidates under this peak are signals misidentified as accidental background using the “best Tdiff” method.

to the carbon target, as already discussed in 3.5. These two yields will be fitted by the theoretical amplitudes to extract the  $\pi^0$  decay width. Fig. 4.26 shows the yields extracted with all HYCAL acceptance for the silicon target. It is interesting to see how the incoherent process rises to dominate where  $\theta_{\pi^0} > 3^\circ$ . However, due to poor energy resolution of the lead glass modules, the yield including the lead glass acceptance is not used in the  $\pi^0$  decay width analysis.

#### 4.7 Theoretical Description of Forward Photoproduction of $\pi^0$

The Primakoff method to measure the  $\pi^0$  lifetime uses the  $\pi^0$  photoproduction in the Coulomb field of a heavy nucleus. This is a coherent process, which means the nucleus is not excited or broken up

$$\gamma + A \rightarrow \pi^0 + A. \quad (4.27)$$

Another coherent process is the  $\pi^0$  photoproduction via the strong interaction between the incoming  $\gamma$  and the nucleus. The separation of this process is proved to

be the most challenging part in the Primakoff method to obtain the  $\pi^0$  lifetime as it is the major background mixed with the Primakoff peak. The full amplitude of the coherent process is the sum of the primkoff process  $T_{Pr}$ , and the strong process  $T_{NC}$ :

$$T_c = T_{Pr} + e^{i\psi} T_{NC}, \quad (4.28)$$

where  $\psi$  is the phase angle between the Primakoff and the coherent strong cross section. Adding the incoherent process  $\frac{d\sigma_{inc}}{d\Omega}$ , the total differential cross section can be written as:

$$\frac{d\sigma}{d\Omega} = |T_{Pr} + e^{i\psi} T_{NC}|^2 + \frac{d\sigma_{inc}}{d\Omega}. \quad (4.29)$$

The full differential cross section of the  $\pi^0$  photoproduction can be further expressed as:

$$\frac{d\sigma}{d\Omega} = \frac{d\sigma_{Pr}}{d\Omega} + \frac{d\sigma_{NC}}{d\Omega} + \frac{d\sigma_{inc}}{d\Omega} + 2\sqrt{\frac{d\sigma_{Pr}}{d\Omega} \cdot \frac{d\sigma_{NC}}{d\Omega}} \cos(\psi), \quad (4.30)$$

where  $\frac{d\sigma_{Pr}}{d\Omega} = |T_{Pr}|^2$ , and  $\frac{d\sigma_{NC}}{d\Omega} = |T_{NC}|^2$ .

The Primakoff cross section  $\frac{d\sigma_{Pr}}{d\Omega}$  can be written as [14]:

$$\frac{d\sigma_{Pr}}{d\Omega} = \Gamma_{\gamma\gamma} \frac{8\alpha Z^2}{m_{\pi^0}^3} \frac{\beta^3 E^4}{Q^4} |F_{e.m.}(q)|^2 \sin^2(\theta_\pi), \quad (4.31)$$

where  $\Gamma_{\gamma\gamma}$  is the  $\pi^0$  decay width,  $Z$  is the atomic number of the target atom,  $m_{\pi^0}$ ,  $\beta$ ,  $\theta_\pi$  are the mass, velocity and production angle of the  $\pi^0$ ,  $E$  is the beam photon energy,  $q$  is the momentum transfer to the nucleus, and  $F_{e.m.}(q)$  is the nuclear electromagnetic form factor of the target nucleus.

The nuclear coherent cross section and nuclear incoherent cross sections can be expressed as [14, 36]:

$$\frac{d\sigma_{NC}}{d\Omega} = C_S \cdot A^2 |F_N(q)|^2 \sin^2 \theta_\pi, \quad (4.32)$$

$$\frac{d\sigma_{NI}}{d\Omega} = C_I \cdot A^{\frac{3}{4}} \cdot (1 - G(q)), \quad (4.33)$$

where  $A$  is the nucleon number and  $F_N(q)$  is the form factor of the nuclear matter distribution in the nucleus, and  $G(q)$  is given by [36]:

$$G(q) = \left[1 + \left(\frac{q}{2\alpha}\right)^4\right] \exp\left[-\left(\frac{q}{2\alpha}\right)^2\right], \quad (4.34)$$

$$\alpha = \frac{15}{4R^2} \quad (4.35)$$

where  $R$  is nuclear radius.

By comparing the theoretical cross section expressed in equation 4.30 to the experimental outcome, one can estimate the values of the theory parameters  $\Gamma_{\gamma\gamma}$ ,  $C_S$ ,  $C_I$  and  $\psi$ . In order to perform this comparison, the theoretical cross section amplitudes need to be first convoluted with the experimental acceptance. In section 4.8, the acceptance calculation will be discussed.

## 4.8 Experimental Acceptance and Angular Resolution

In order to fit the  $\pi^0$  yields, the theoretical cross section needs to be convoluted with the experimental acceptance and the resolution matrix to obtain the  $\frac{dN_{\pi^0}}{d\theta}(\theta, \mathfrak{P})$ , where  $\mathfrak{P}$  is the set of theory parameters, *i.e.*,  $\Gamma_{\gamma\gamma}$ ,  $C_S$ ,  $C_I$  and  $\psi$ .  $\frac{dN_{\pi^0}}{d\theta}(\theta, \mathfrak{P})$  can be expressed in the form:

$$\frac{dN_{\pi^0}}{d\theta_{rec}}(\theta_{rec}, \mathfrak{P}) = N_{\gamma} \times t \times \epsilon \times \sum_{E-channel, i, \theta} \frac{d\bar{\sigma}}{d\theta}(\theta, \mathfrak{P}, i) \times \omega_{flux}(i) \times M(i, \theta, \theta_{rec}), \quad (4.36)$$

where:

$\theta_{rec}$  is the reconstructed  $\pi^0$  production angle;

$\theta$  is the actual  $\pi^0$  production angle;

$N_{\gamma}$  is the total number of tagged photons, *i.e.*, tagged photon flux (see section 4.4);

$t$  is the target thickness, *i.e.*, the number of target atoms per square unit (see section 3.5);



$\epsilon = \epsilon_1 \cdot \epsilon_2 \dots$ , includes all the relevant efficiencies and will be summarised in section 4.9;

$\frac{d\sigma}{d\theta}(\theta, \mathfrak{P}, i)$  is the  $\pi^0$  production differential cross section for the given  $\theta$  and energy for the  $i^{th}$  E-channel (see section 4.7);

$\omega_{flux}(i)$  is the fraction of tagged photon flux corresponding to the  $i^{th}$  E-channel;

$M(i, \theta, \theta_{rec})$  is the acceptance and angular resolution matrix.

All the terms except for  $M(i, \theta, \theta_{rec})$  in equation 4.36 have already been discussed. In this section the method to calculate this matrix will be described.

The experimental acceptance and angular resolution matrix  $M(i, \theta, \theta_{rec})$  is calculated based on 9.9 billion Monte Carlo events. These events are uniformly distributed between 0 to 5.5 degrees, and among 180 tagger E-channels. Since it is a Monte Carlo simulation, the actual  $\pi^0$  production angle  $\theta$  is known. The physics processes of decay photons depositing energies (pair productions, electron avalanches, etc.) into the HYCAL modules are simulated using the GEANT3 package [37], and HYCAL clusters are generated by the same island algorithm as described in section 4.3.2. The reconstructed  $\pi^0$  production angle  $\theta_{rec}$  is obtained by processing these simulated events as real data.

The actual  $\pi^0$  production angles  $\theta$  are divided into  $0.001^\circ$  angular bins, which make the average number of  $\pi^0$ s generated in one  $\theta$  bin  $\sim 1.8 \times 10^6$ . The HYCAL acceptance in the Primakoff region is roughly 50%. As a result, the statistic uncertainty from the Monte Carlo is about 0.1% per  $0.001^\circ$  for all E-channels together. In reality the  $M(i, \theta, \theta_{rec})$  will be summed into the reconstructed angle  $\theta_{rec}$  bins, therefore the 0.1% is the max possible uncertainty. The reconstructed  $\pi^0$  production angles  $\theta_{rec}$  are divided into  $0.02^\circ$  angular bins, the same as the binning used in the yield extraction. In order to study the binning effect of the  $\pi^0$  production angle,  $0.015^\circ$ ,  $0.02^\circ$  and  $0.03^\circ$  binnings of  $\theta_{rec}$  are also used (see chapter 5). The value of

$M(i, \theta, \theta_{rec})$  is calculated in this way:

$$M(i, \theta, \theta_{rec}) = \frac{N_{\pi^0}(\theta \rightarrow \theta_{rec}, i)}{N_{\pi^0}(\theta, i)}, \quad (4.37)$$

where  $N_{\pi^0}(\theta, i)$  is the number of  $\pi^0$  generated within the finer  $\theta$  bin, and  $N_{\pi^0}(\theta \rightarrow \theta_{rec}, i)$  represents the number of these  $\pi^0$ s reconstructed within the coarser  $\theta_{rec}$  bin. The energies of these  $\pi^0$ s are within the range of the  $i^{th}$  E-channel energy bin. Fig. 4.27 shows the distribution of  $M(i, \theta, \theta_{rec})$  formed by simulated  $\pi^0$ s from two different  $\theta$  bins ( $0^\circ$  and  $1.5^\circ$ ). It is worth noting that the resolution becomes better near  $0^\circ$  since the  $\theta_{rec}$  must be greater than  $0^\circ$ . This effect is observed in the fitting of the “hybrid mass” distribution. Taking the sum of  $M(i, \theta, \theta_{rec})$  over the E-channel id and  $\theta_{rec}$ , one obtains the acceptance over the actual  $\pi^0$  production angle  $\theta$ . Fig. 4.28 shows the acceptance for the HYCAL PbWO<sub>4</sub> crystal region as a function of  $\pi^0$  production angle  $\theta$ . The experimental acceptance and resolution is essentially the same for the two targets except that the corrections of the “dead” ADC’s are different during the silicon and the carbon runs. In order to save time, the Monte Carlo described in the previous paragraphs was only performed for the silicon target, and different “dead” HYCAL ADC tables were used for the silicon and the carbon target when processing the simulated events. The decay photon absorption by the target (mainly  $e^+e^-$ -pair production) is also simulated in this Monte Carlo. However since the thickness of silicon target is 10% radiation length while that of the carbon target is 8%, the probabilities of decay photon absorption are different. For the silicon target, the decay photon absorption is automatically included in the acceptance calculation. Therefore only the ratio of the carbon and silicon decay photon absorption is needed. Moreover, the beam photon can also be absorbed, but this process is not included in the Monte Carlo described above, as a result two more correction factors need to be calculated. Therefore, two fast Monte Carlo simulations were performed for

Table 4.1: The constant factors used in the fitting to the  $\pi^0$  photoproduction yields.

| Parameter or correction                                                 | Target [Sample]             | Value         | Error        |
|-------------------------------------------------------------------------|-----------------------------|---------------|--------------|
| Flux, [ $\times 10^{12}$ ]                                              | Si (all runs)               | 5.5420        | $\sim 0.8\%$ |
|                                                                         | Si (reduced set)            | 5.2821        |              |
|                                                                         | C <sup>12</sup>             | 2.41782       |              |
| Number of Atoms<br>per square unit, [barn <sup>-1</sup> ]               | Si                          | 0.049735      | 0.35%        |
|                                                                         | C <sup>12</sup>             | 0.177009      | 0.02%        |
| BR( $\pi^0 \rightarrow \gamma\gamma$ )                                  | All                         | 0.98823       | 0.00034      |
| $\gamma$ -beam absorption<br>in target                                  | Si                          | 0.9605        | 0.0008       |
|                                                                         | C <sup>12</sup>             | 0.97008       | 0.0006       |
| $\pi^0 \rightarrow \gamma\gamma$ decay products<br>absorption in target | C <sup>12</sup> vs Si ratio | 1.018         | N/A          |
| Signal fraction out<br>of  Tdif  < 7.0 ns cut                           | Si (all runs)               | 0.0014        | 0.0003       |
|                                                                         | Si (reduced set)            | 0.0020        | 0.0003       |
|                                                                         | C <sup>12</sup>             | 0.0068        | 0.0017       |
| Best-in-time correction<br>within  Tdif  < 3.5 ns window                | Si (reduced set)            | 0.0116        | 0.0014       |
|                                                                         | C <sup>12</sup>             | 0.0145        | 0.0017       |
| Events with ADC error                                                   | applied to flux             | 0.002...0.014 | <0.001       |
| HyCal energy response function                                          | All                         | 0.9956        | 0.0044       |

the silicon and carbon targets respectively to study the photon absorptions. The results will be summarised in section 4.9.

## 4.9 $\pi^0$ Yields Fitting

The  $\pi^0$  photoproduction yields obtained in section 4.6.5 can be fitted by equation 4.36. All the efficiency numbers included in the  $\epsilon$  term in equation 4.36 are listed in table 4.1. where:

BR( $\pi^0 \rightarrow \gamma\gamma$ ) is the braching ratio for the  $\pi^0 \rightarrow \gamma\gamma$  channel [7];

$\gamma$ -beam absorption and  $\pi^0 \rightarrow \gamma\gamma$  decay products absorption in target are factors to correct photon absorptions as discussed in section 4.8;

Signal fraction out of |Tdif| < 7.0 ns is the Tdiff cut efficiency;

Events with ADC error: whenever there is an ADC error, the events are not

Table 4.2:  $\pi^0$  decay width obtained from silicon and carbon targets

| Target          | $\chi^2/NDF$ | $\Gamma_{\gamma\gamma}$ (eV) |
|-----------------|--------------|------------------------------|
| Silicon         | 1.02         | $7.83 \pm 0.06$              |
| $^{12}\text{C}$ | 1.11         | $7.78 \pm 0.12$              |

counted into the  $\pi^0$  yield, therefore ADC error corrections are estimated to reduce the tagged photon flux correspondingly;

HYCAL energy response function represents the HYCAL trigger efficiency.

The fitting procedure minimizes the  $\chi^2/NDF$  by optimizing the set of theory parameters  $\mathfrak{P}$ . The fitting is performed using ROOT [38]. Fig. 4.29 (a) and (b) show the fitting of  $\pi^0$  yields up to  $2.5^\circ$  with only the HYCAL  $\text{PbWO}_4$  crystals for the silicon target and the carbon target, respectively.

The decay width obtained from these two fittings are listed in table 4.2:

The statistical uncertainty for the silicon target is less than 1%, and the decay width difference between the two targets are within 0.5%. Detailed discussion regarding the results and the study of systematic uncertainties will be presented in chapter 5.

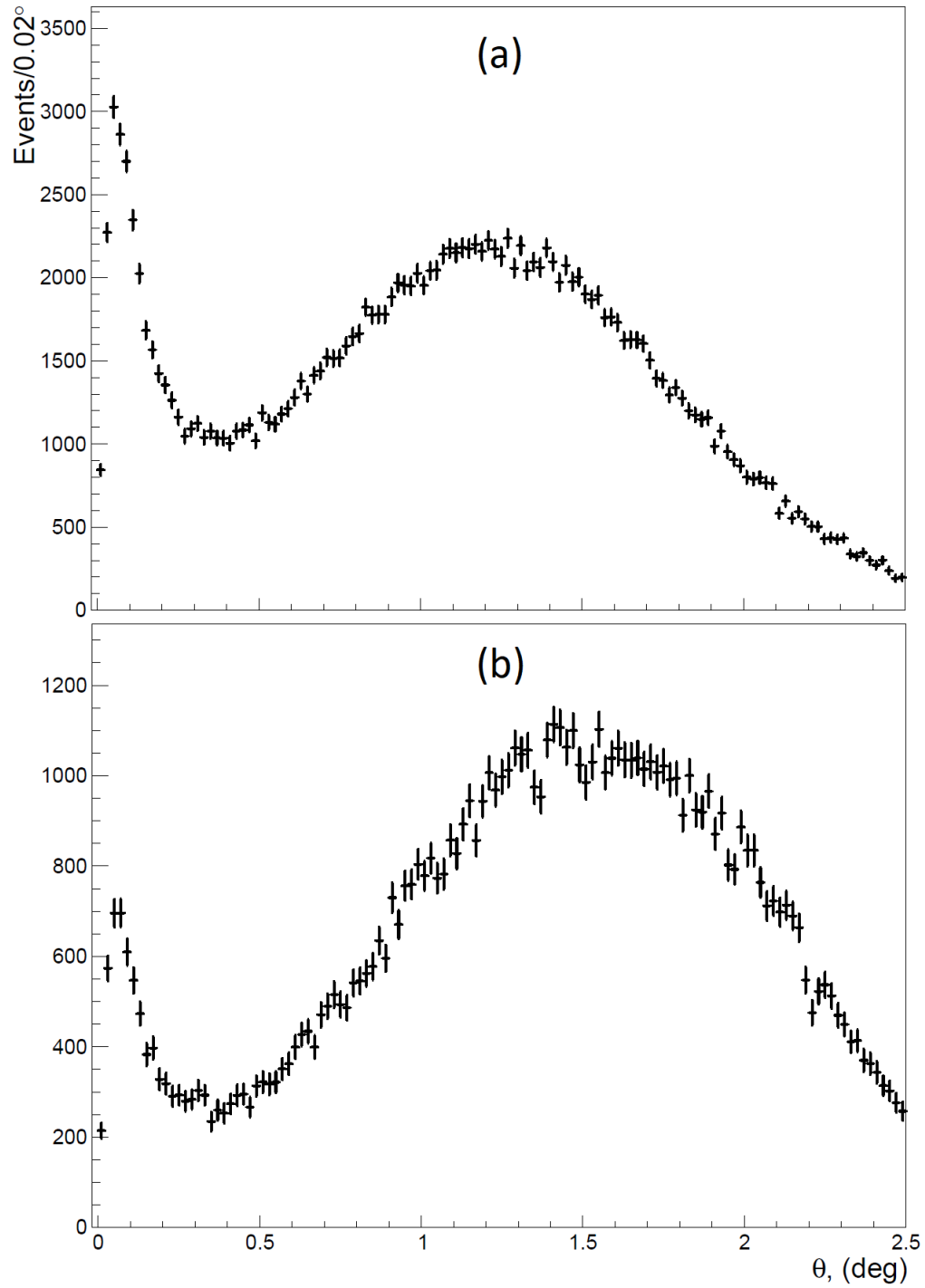


FIGURE 4.25: The  $\pi^0 \rightarrow \gamma\gamma$  yields for (a) the silicon and (b) the carbon target. Both yields are extracted with only the  $\text{PbWO}_4$  acceptance. The Primakoff peak for the silicon target is more pronounced compared to the carbon target, as already discussed in 3.5

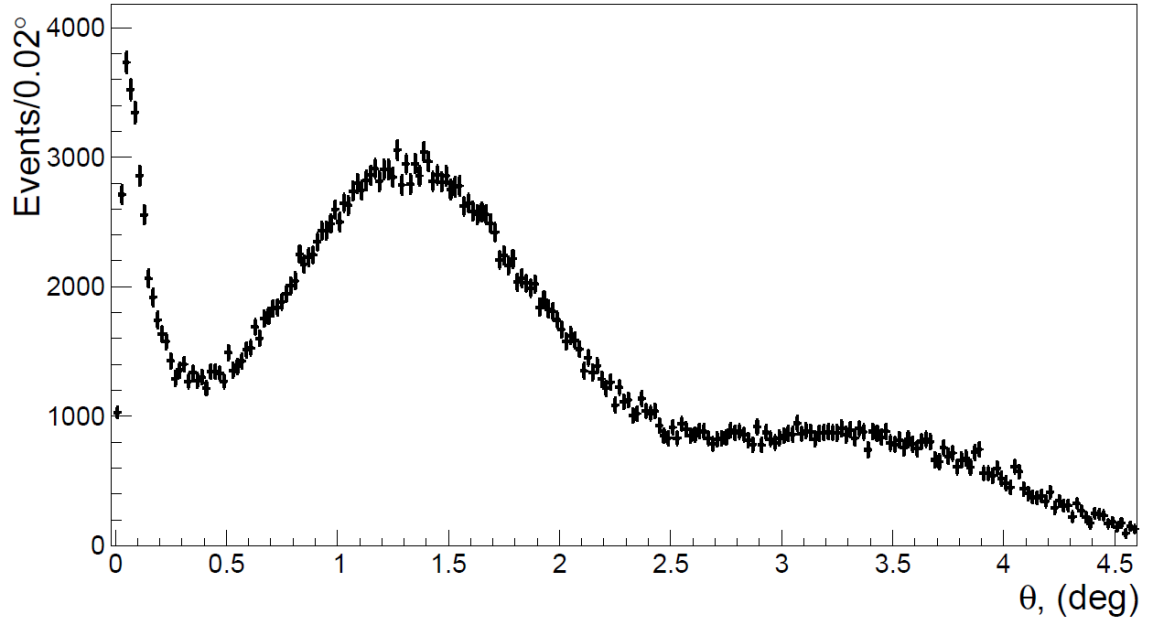


FIGURE 4.26: The  $\pi^0 \rightarrow \gamma\gamma$  yield for the silicon target with all HYCAL acceptance. However, due to poor energy resolution of the lead glass modules, the yield including the lead glass acceptance is not used in the  $\pi^0$  decay width analysis.

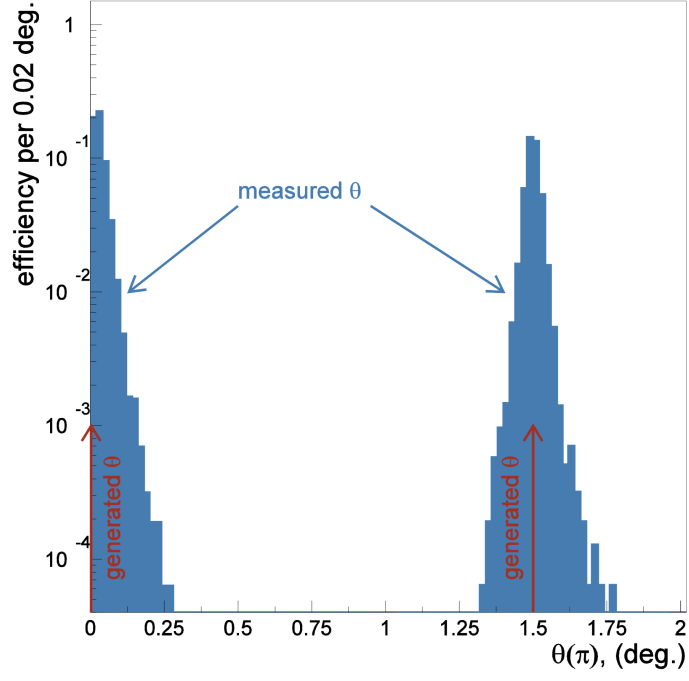


FIGURE 4.27: The distribution of  $M(i, \theta, \theta_{rec})$  formed by simulated  $\pi^0$ s from two different  $\theta$  bins ( $0^\circ$  and  $1.5^\circ$ ).

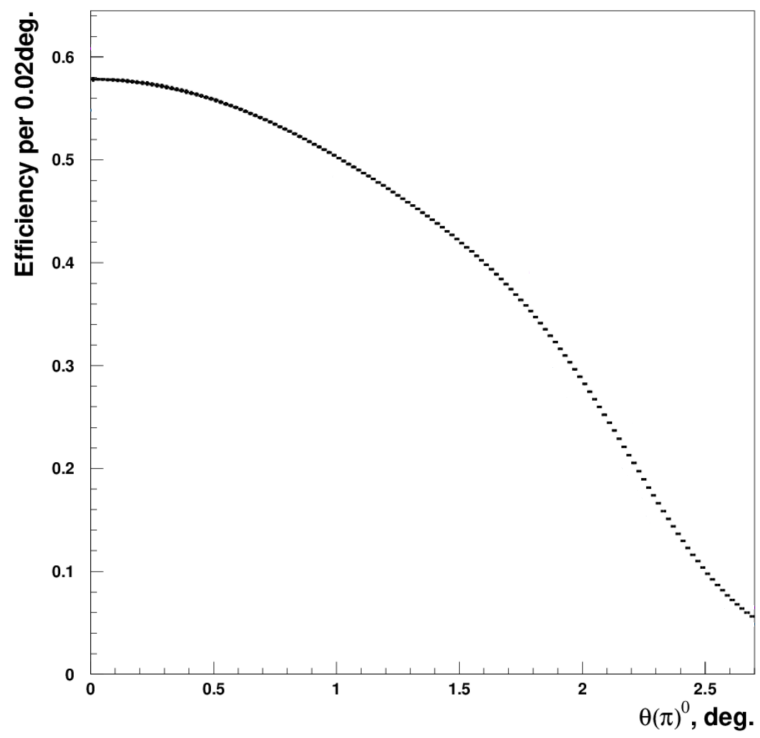


FIGURE 4.28: The HYCAL PbWO<sub>4</sub> acceptance as a function of the actual  $\pi^0$  production angle  $\theta$ .



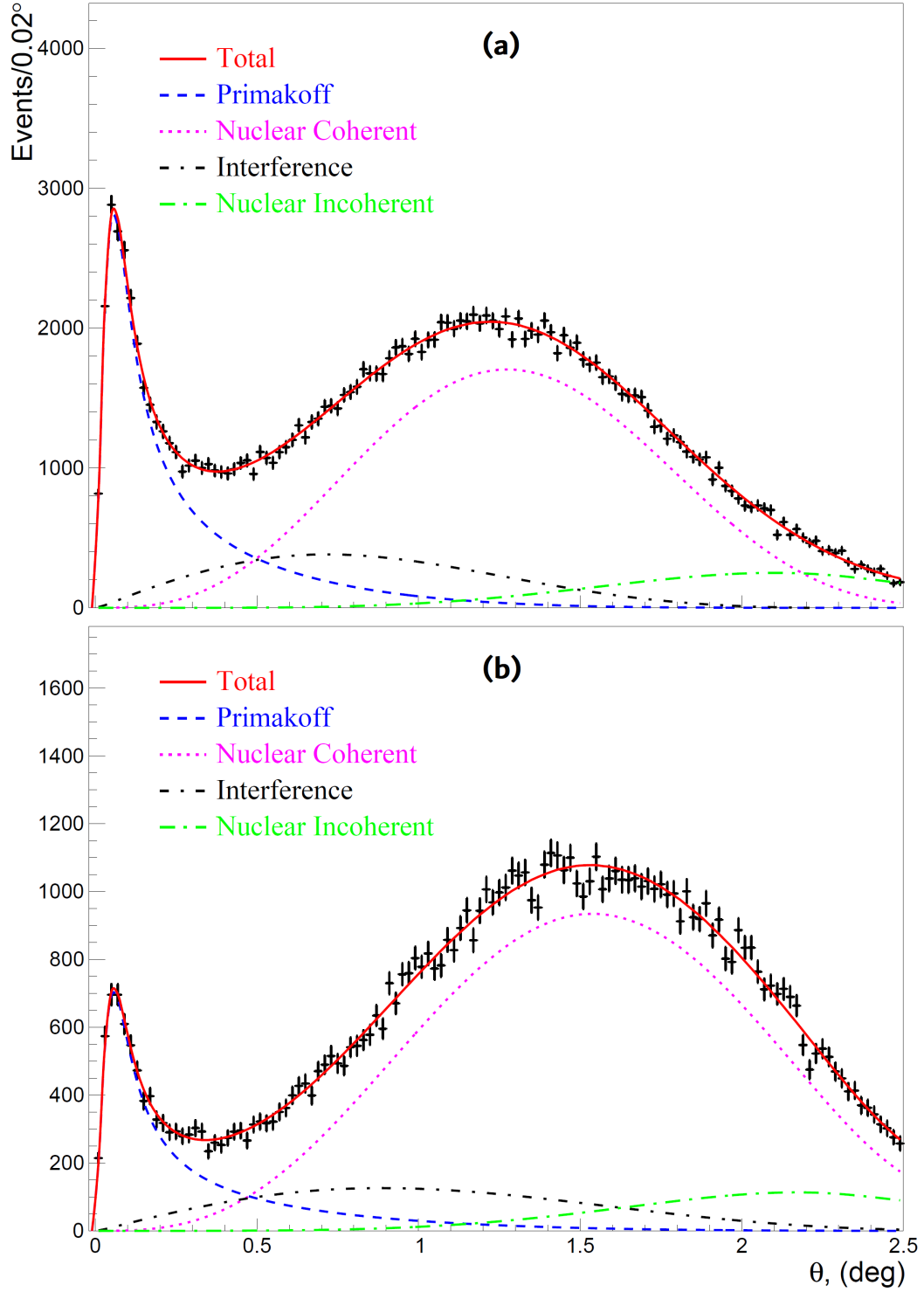


FIGURE 4.29: (a) and (b) show the fitting of  $\pi^0$  yields upto  $2.5^\circ$  with only the HYCAL  $\text{PbWO}_4$  crystals for the silicon target and the carbon target respectively. The four different physics processes are labeled.

## Results and Conclusions

In this chapter, the calculations of the systematic uncertainties will be discussed. In most sections of this chapter, the analyses and the results of the systematic uncertainties for the silicon and carbon targets are the same, and the silicon data are used. The carbon target will only be mentioned whenever the carbon uncertainty is different from that of the silicon target. The total uncertainty budget table will be summarised in the end.

### 5.1 Branching Ratio

The branching ratio of  $\pi^0 \rightarrow \gamma\gamma$  channel is [7]:

$$Br(\pi^0 \rightarrow \gamma\gamma) = (98.823 \pm 0.034)\%. \quad (5.1)$$

The uncertainty of the branching ratio is 0.034%, which will be directly propagated into the final systematic uncertainty.

## 5.2 Uncertainties from Target Measurement

The thickness of the PrimEx-II targets are measured by the UMass group [23, 24]. The measurement is discussed in section 3.5 and the results are summarised in table 3.1. For silicon, the contribution of the target measurement to the systematic uncertainty is 0.35%, and for carbon it is 0.02%.

## 5.3 Uncertainties from Yield Extraction

### 5.3.1 *Uncertainties from Single $\gamma$ Energy Cut*

In  $\pi^0$  yield extraction an energy cut of 0.5 GeV is applied to the single decay  $\gamma$ . The effect of this energy cut is studied and will be presented in this section.

In order to study the systematic uncertainty of the single  $\gamma$  energy cut, a set of cut values between 0.1 GeV to 0.7 GeV with a step of 0.02 GeV are used. The acceptance is recalculated based on these new cut values. The effect of this cut to the decay width is studied by refitting the  $\pi^0$  yields corresponding to the different values. The decay width  $\Gamma(\pi^0)$  is drawn as a function of the energy cut in Fig. 5.1, which is stable until the energy cut is increased to  $\sim 0.56$  GeV. The energy cut of 0.5 GeV is chosen in the analysis to cut off as much background as possible. The half maximum difference among these recalculated decay widths corresponding to the energy cuts smaller than 0.56 GeV is 0.0045 eV, or 0.05% of the  $\pi^0$  decay width. This number is used to estimate the systematic uncertainty of the decay width due to the single  $\gamma$  energy cut.

### 5.3.2 *Uncertainties from $\pi^0$ Energy Cut*

As discussed in section 4.1, we are only interested in the events where the total energy of the two decay  $\gamma$ 's are about the same as the beam energy. In order to reduce background, an additional cut of 3.5 GeV to the total energy of  $\pi^0$  candidates

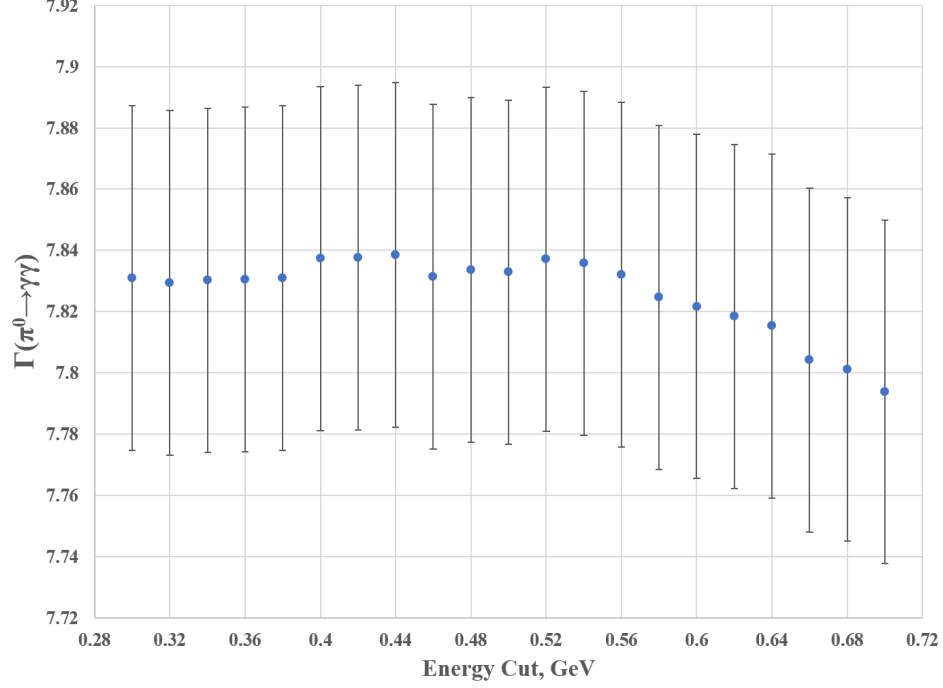


FIGURE 5.1: The  $\Gamma(\pi^0)$  is plotted as a function of the single  $\gamma$  energy cut. In order to study the effect of the energy cut on the decay width, it is varied from 0.1 GeV to 0.7 GeV with a step of 0.02 GeV. The energy cut used in the analysis is 0.5 GeV, which lies in the region where the decay width is relatively stable. The error bars shown in this figure are statistical uncertainties, and thus do not represent the variations studied in this section.

was applied in the  $\pi^0$  analysis. This cut is called the  $\pi^0$  energy cut. Similar to the single  $\gamma$  energy cut, the systematic uncertainty of this cut is studied by varying its value from 3.0 GeV to 4.6 GeV with a step of 0.1 GeV. The decay width  $\Gamma(\pi^0)$  is drawn as a function of the  $\pi^0$  energy cut in Fig. 5.2, which is stable until the  $\pi^0$  energy cut is increased to  $\sim 4.2$  GeV. The half maximum difference among the decay width's calculated with this cut between 3.0 GeV to 4.2 GeV is 0.0045 eV, or 0.05%. This value is used as the systematic uncertainty of the  $\pi^0$  energy cut.

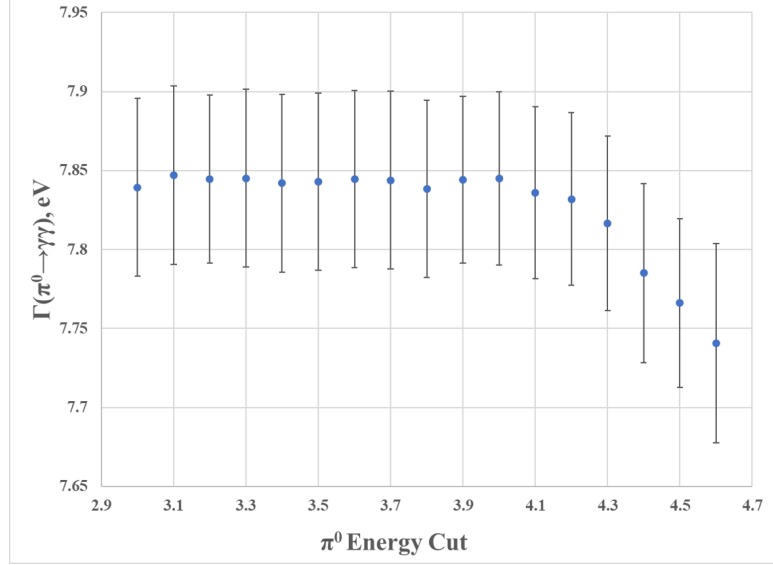


FIGURE 5.2: The  $\Gamma(\pi^0)$  is plotted as a function of the  $\pi^0$  energy cut. In order to study the effect of the energy cut on the decay width, it is varied from 3.0 GeV to 4.6 GeV with a step of 0.1 GeV. The decay width's obtained between 3.0 GeV to 4.2 GeV are stable, and the maximum difference among them is 0.009 eV. The error bars shown in this figure are statistical uncertainties, and thus do not represent the variations studied in this section.

### 5.3.3 Decay Width Sensitivity to Tdiff Cut

The Tdiff cut is used in the analysis to reject the accidental background. In order to ensure that a proper Tdiff window is used in the analysis and estimate its contribution to the systematic uncertainty, different window sizes are studied and the results will be presented in this section.

The default Tdiff cut window applied in the  $\pi^0$  yield extraction is  $[-7, 7]$  ns. To evaluate the systematic uncertainty, a set of Tdiff cut windows from  $[-2.0, 2.0]$  ns to  $[-10.0, 10.0]$  ns with a step of 0.5 ns are used. The Tdiff cut efficiency explained in 4.6.2 is also recalculated correspondingly. Fig. 5.3 shows the Tdiff cut efficiency for different windows for both silicon and carbon targets. The obtained  $\Gamma(\pi^0)$ 's are drawn as a function of the absolute value of the Tdiff cut,  $|\text{Tdiff}|$  in Fig. 5.4.

In summary, the size of the Tdiff cut window has little effect on the decay width

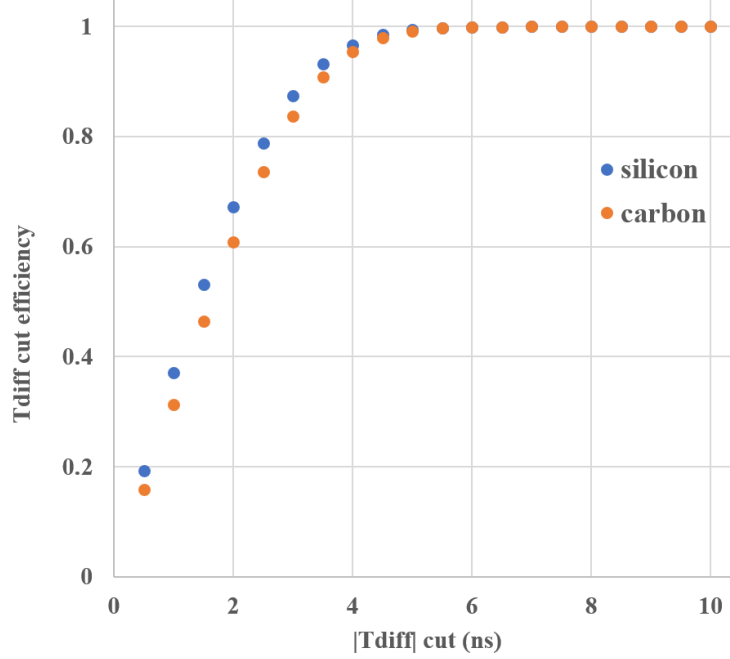


FIGURE 5.3: The efficiency of Tdiff cut as a function of the absolute value of the Tdiff cut. The efficiency reaches a plateau when  $|Tdiff| > 5$  ns. The Tdiff cut window used in the analysis is  $[-7, 7]$  ns, where the efficiency is 99.98%.

when  $|Tdiff| > 5$  ns. The half maximum difference among the decay width's calculated using different Tdiff cut window in this region is 0.00195 eV, which is 0.025% of the decay width.

#### 5.3.4 “Hybrid Mass” Fitting Uncertainties

The  $\pi^0$  yield is extracted by fitting the “hybrid mass”. This fitting procedure was discussed in section 4.6.3. A few examples of the “hybrid mass” fitting can be found in Fig. 4.23. In these examples a piecewise polynomial background function was used in this fitting. In order to investigate any systematic effects in the method of yield extraction, simple second order and third order polynomial backgrounds are also investigated. After the fitting, the  $\pi^0$  yields are obtained by calculating the number of  $\pi^0$ s under the fitted peak, in this case the Monte Carlo simulated

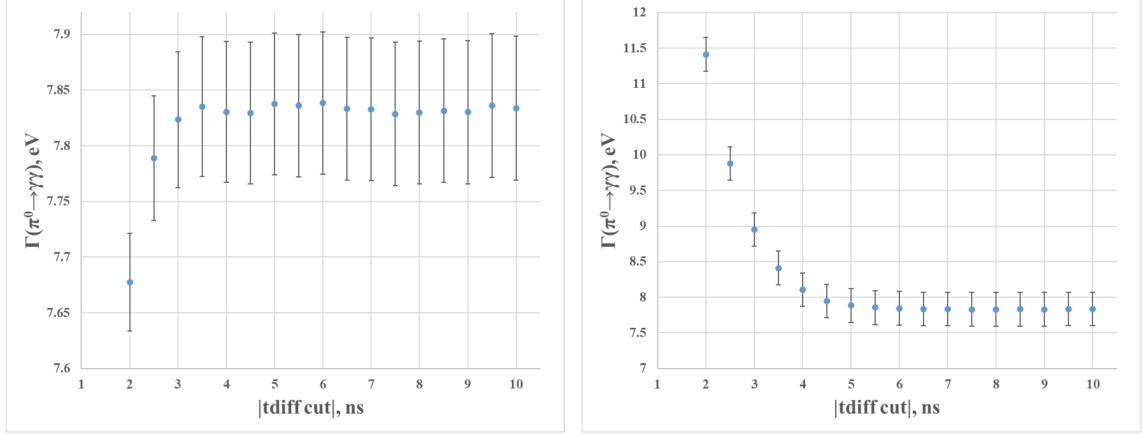


FIGURE 5.4: The  $\Gamma(\pi^0)$ s are plotted as a function of the absolute value of the Tdiff cut. The Tdiff cut efficiency is not taken into account in the left plot, but it is included in the calculation in the right plot. Both plots show the decay width reaches a plateau when  $|\text{Tdiff}| > 5$  ns. The error bars shown in these two figures are statistical uncertainties, and thus do not represent the variations studied in this section.

signal lineshape. The yield can also be obtained by subtracting the total background (accidentals,  $\omega$  background and polynomial background) from the total number of  $\pi^0$ s under the “hybrid mass” within a window, and then corrected by the cut efficiency corresponding to this window. The range of the “hybrid mass” fitting is varied between 0.07 to 0.15 to estimate the systematic uncertainties. Fig. 5.5 shows the extracted  $\Gamma(\pi^0)$  for the silicon target using different background functions, various ranges of fitting, and the aforementioned two methods to count the  $\pi^0$ s. The average value of the  $\Gamma(\pi^0)$  from this study is  $7.822 \pm 0.056$  eV, and the systematic uncertainty is taken as half of the maximum difference among the extracted  $\Gamma(\pi^0)$ s, which is 0.044 eV, or 0.56%. Fig. 5.6 shows the results for the carbon target. The average value of the  $\Gamma(\pi^0)$  for carbon is  $7.776 \pm 0.111$  eV, and the systematic uncertainty from “hybrid mass” fitting is 0.06 eV, or 0.8%.

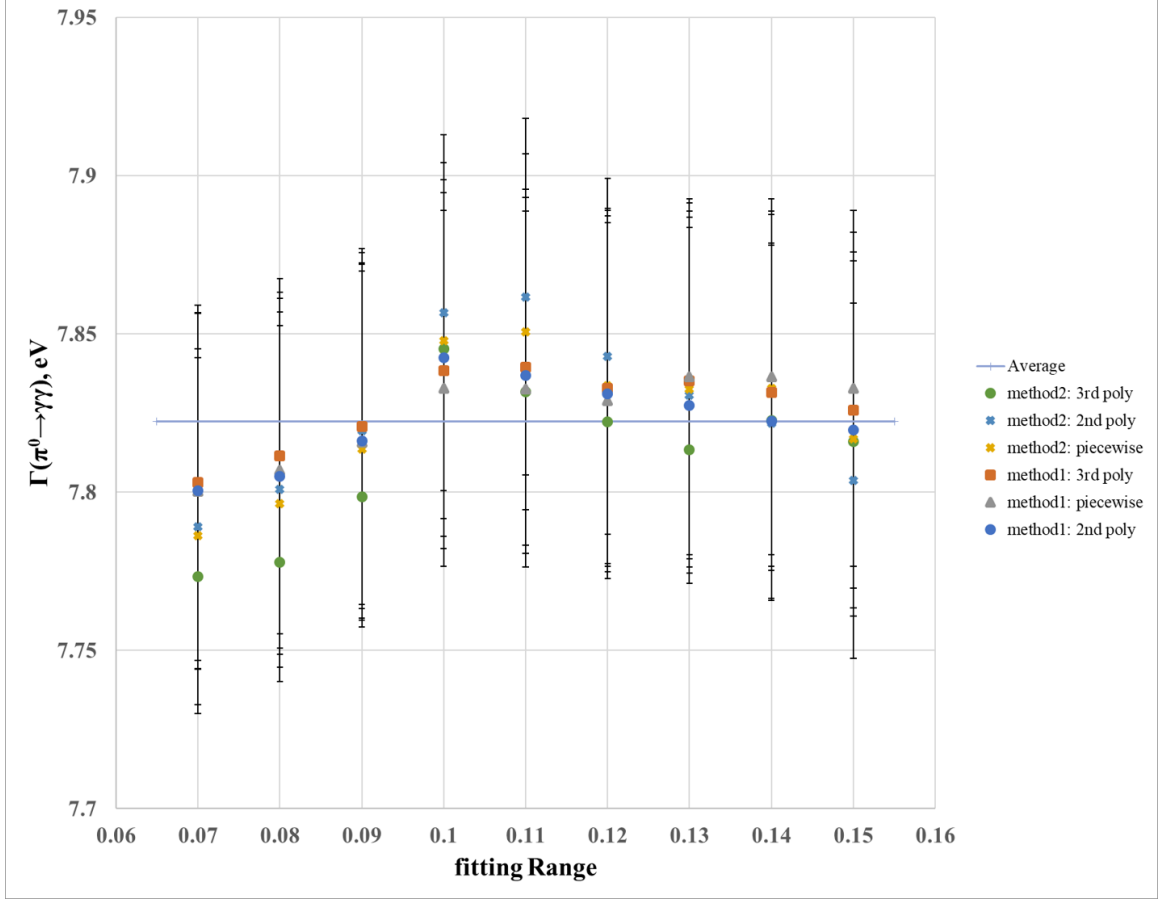


FIGURE 5.5: The  $\Gamma(\pi^0)$ s calculated using different methods for the silicon target. Three different background functions: the piecewise function, 2nd order polynomial and 3rd order polynomial, and nine fitting ranges (from 0.07 to 0.15) are investigated. To obtain the  $\pi^0$  yields, two methods are used: method1 using the number of  $\pi^0$ s under the fitted signal peak; method2 using the difference between the total number of the  $\pi^0$  under the “hybrid mass” and the background. The error bars shown in this figure are statistical uncertainties, and thus do not represent the variations studied in this section.

### 5.3.5 Comparison of Yields with Different Binnings

As discussed in 4.6.3, the  $\pi^0$  photoproduction yield is extracted using  $0.02^\circ$  angular bin. The  $0.015^\circ$  and  $0.03^\circ$  angular bins are also studied to estimate the effect of the bin size to the decay width. Fig. 5.7, Fig. 5.8 and Fig. 5.9 show the fitted  $\pi^0$  yields for silicon with  $0.015^\circ$ ,  $0.02^\circ$  and  $0.03^\circ$  angular bins respectively. And Fig. 5.10,



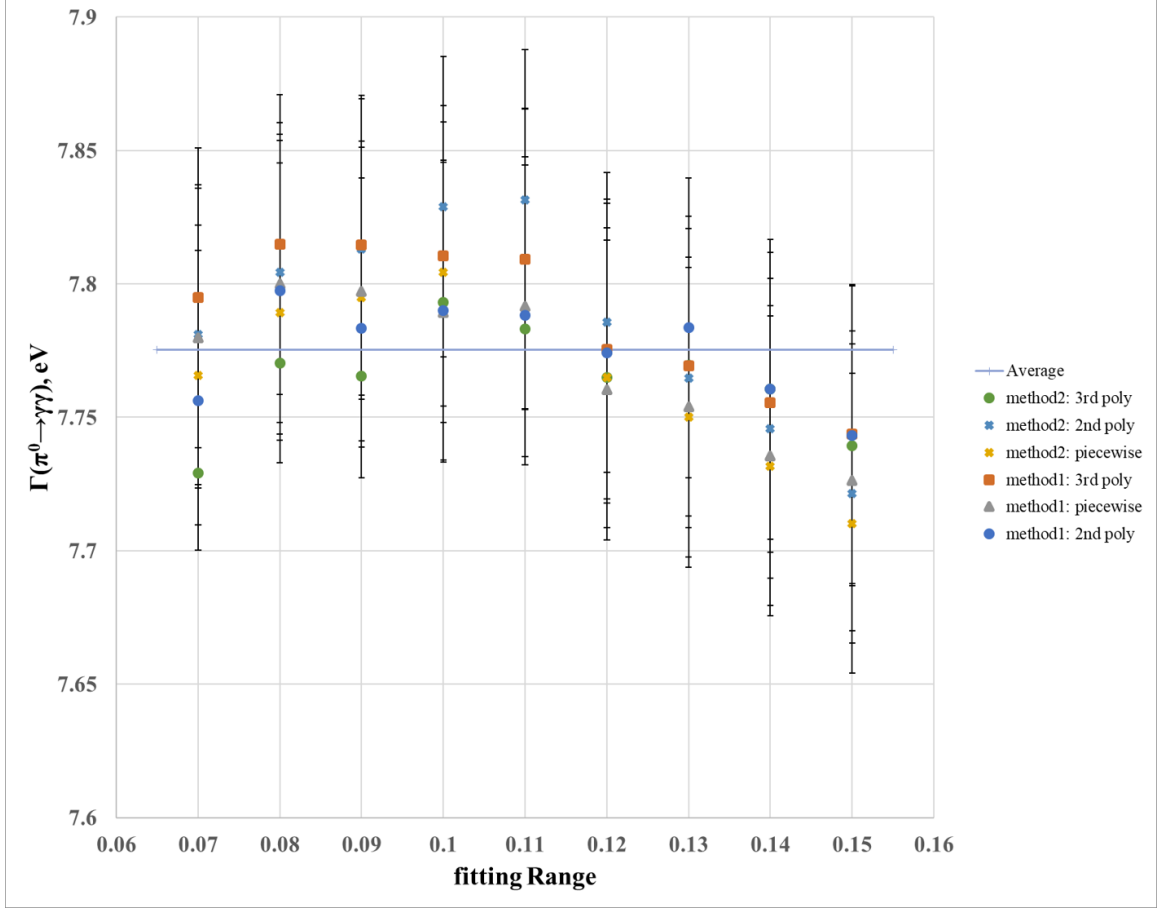


FIGURE 5.6: The  $\Gamma(\pi^0)$ s calculated using different methods for the carbon target. Three different background functions: the piecewise function, 2nd order polynomial and 3rd order polynomial, and nine fitting ranges (from 0.07 to 0.15) are investigated. To obtain the  $\pi^0$  yields, two methods are used: method1 using the number of  $\pi^0$ s under the fitted signal peak; method2 using the difference between the total number of the  $\pi^0$  under the “hybrid mass” and the background. The error bars shown in this figure are statistical uncertainties, and thus do not represent the variations studied in this section.

Fig. 5.11 and Fig. 5.12 show the fitted  $\pi^0$  yields for carbon with  $0.015^\circ$ ,  $0.02^\circ$  and  $0.03^\circ$  angular bins.

The decay width obtained based on different yield bin sizes are listed in table 5.1. The maximum difference for silicon target is 0.004 eV, or 0.05%, and for carbon it's 0.011 eV, or 0.1%.

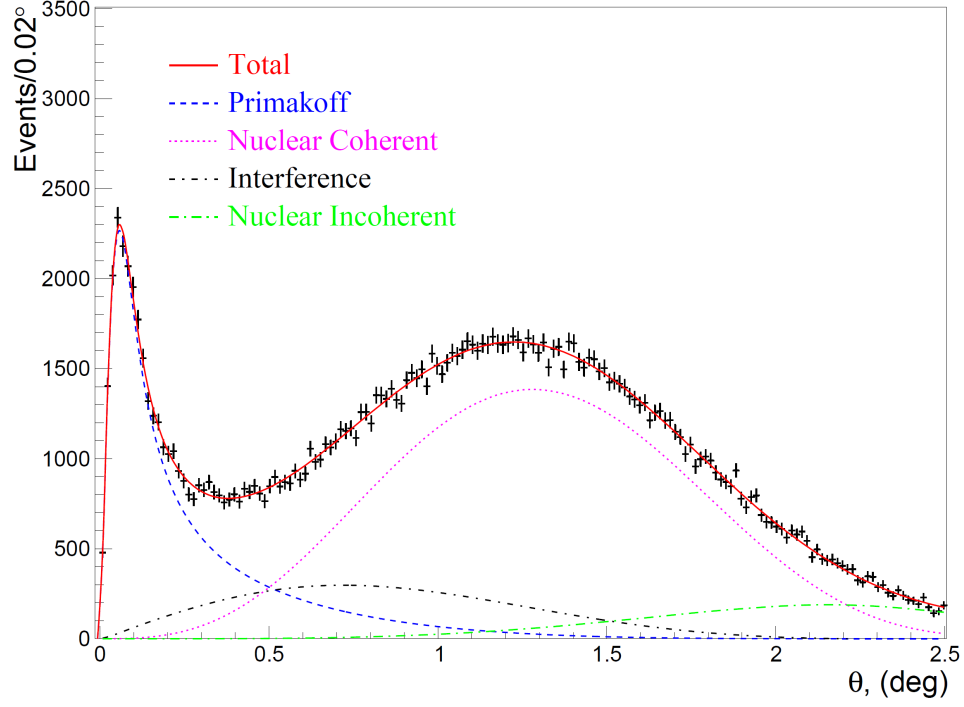


FIGURE 5.7:  $\pi^0$  yield extracted with  $0.015^\circ$  angular bin for silicon.

Table 5.1:  $\pi^0$  decay width obtained from silicon and carbon targets with different angular bins.

| Target          | $\Gamma_{\gamma\gamma}$ (eV) |                   |                   |
|-----------------|------------------------------|-------------------|-------------------|
| Silicon         | $7.834 \pm 0.057$            | $7.833 \pm 0.057$ | $7.830 \pm 0.057$ |
| $^{12}\text{C}$ | $7.773 \pm 0.116$            | $7.784 \pm 0.117$ | $7.783 \pm 0.057$ |

### 5.3.6 Realistic Monte Carlo

For both silicon target and carbon target, 500 samples of realistic Monte Carlo simulation with statistics were performed. These samples are overlaid with real background shape based on the hybrid mass fitting. The fitting results of these samples are demonstrated in Fig. 5.13. The averaged fitted decay width for silicon is 7.75 eV, and for carbon is 7.65 eV. The preset decay width is 7.70 eV. As a result, the systematic error for silicon is 0.65%, and for carbon is also 0.65%.

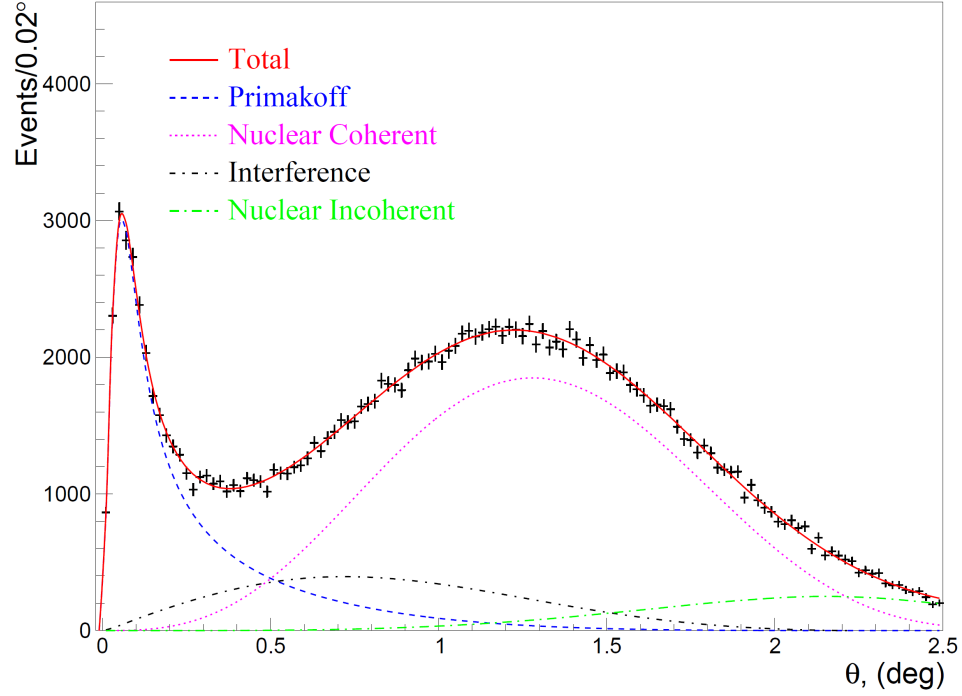


FIGURE 5.8:  $\pi^0$  yield extracted with  $0.02^\circ$  angular bin for silicon.

Table 5.2: Systematic uncertainties of  $\pi^0$  decay width due to uncertainties from the  $\omega$  background

| $\omega$ background variation | $\Gamma(\pi^0)$ shift, silicon (%) | $\Gamma(\pi^0)$ shift, carbon (%) |
|-------------------------------|------------------------------------|-----------------------------------|
| +20%                          | -0.14%                             | 0.03%                             |
| -20%                          | -0.06%                             | -0.16%                            |

#### 5.4 Decay Width Sensitivity to $\omega$ background subtraction

In PrimEx-II, the  $\omega$  background was simulated using GEANT3 package [37], and was subtracted from the signal as discussed in section 4.6.3. The  $\omega$  photoproduction cross section has about 20% uncertainty. In order to study its effect on the decay width, the  $\omega$  background was scaled up and down by 20%. The change to the extracted  $\Gamma(\pi^0)$  is listed in table 5.2.

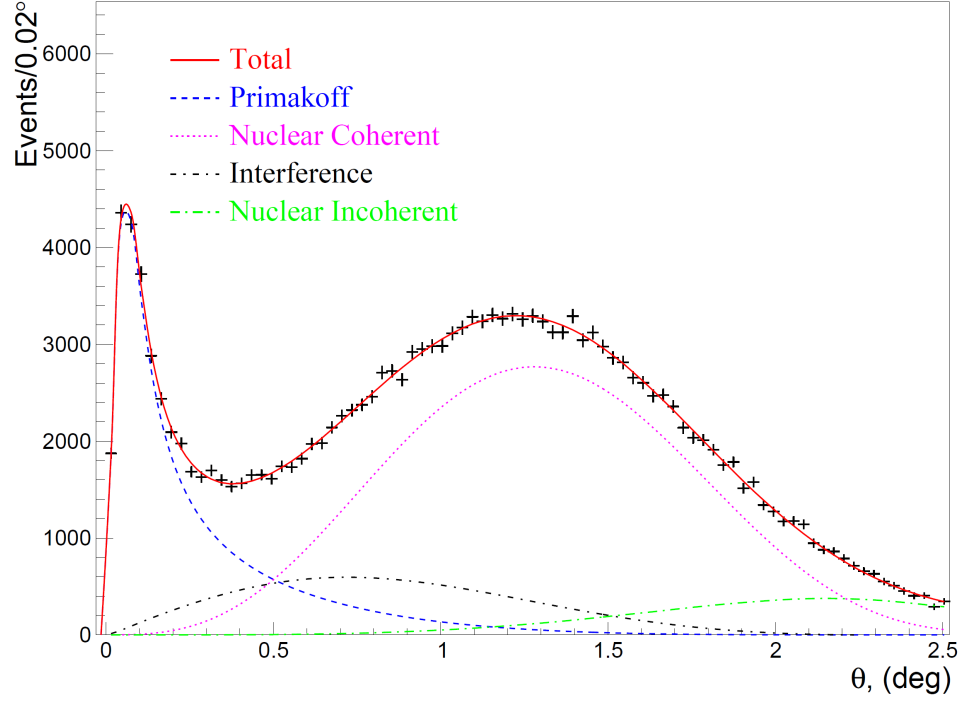


FIGURE 5.9:  $\pi^0$  yield extracted with  $0.03^\circ$  angular bin for silicon.

## 5.5 Decay Width Sensitivity to $\pi^0$ Angular Resolution

As discussed in section 4.8, the  $\pi^0$  angular resolution is determined by Monte Carlo and included in the acceptance resolution matrix. The  $\pi^0$  angular resolution is varied by 10% in order to determine its effect on the decay width. The resulted change in the decay width is only about 0.07%.

## 5.6 Uncertainties from HYCAL Acceptance

Both HYCAL coordinates misalignment and uncertainties from the HYCAL  $z$  position contribute to the uncertainties of the HYCAL acceptance calculation. The calculations of these two items are discussed in this section.

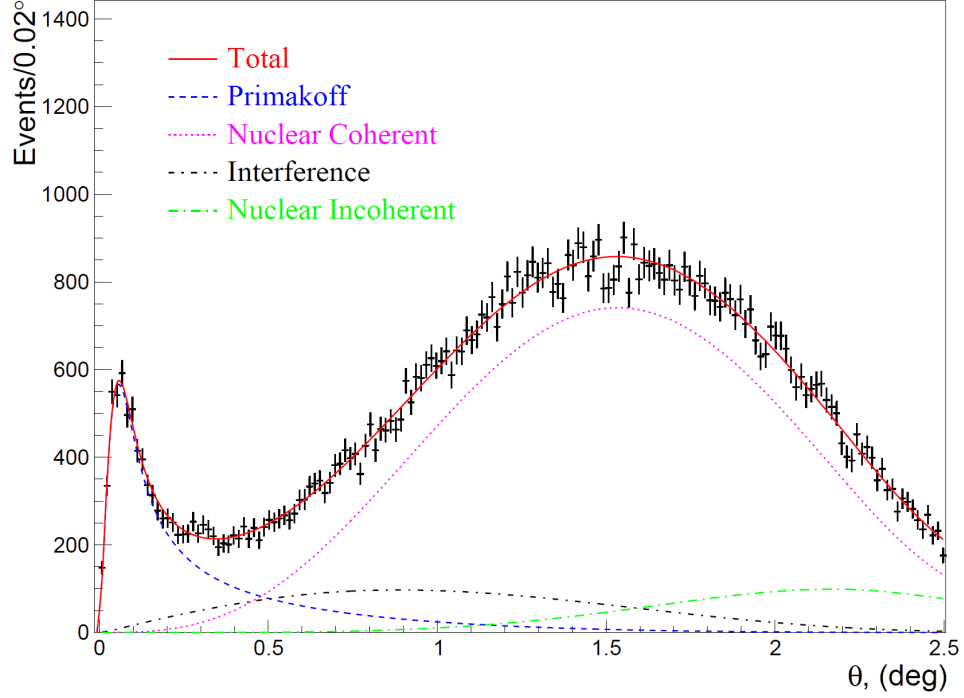


FIGURE 5.10:  $\pi^0$  yield extracted with  $0.015^\circ$  angular bin for carbon.

#### 5.6.1 Decay Width Sensitivity to HYCAL Coordinates Misalignment

The coordinates of the decay  $\gamma$ s on the HYCAL can be reconstructed with high precision. However, the values of these coordinates are based on the HYCAL coordinates reference system. The coordinates reference system was surveyed before the experiment by the JLab survey group. As discussed in section 4.3.4, the HYCAL misalignment is checked using the  $\pi^0$  production data in the analysis.

In order to study the effect of the HYCAL misalignment and estimate the systematic uncertainty, the HYCAL cluster coordinates are varied by adding a small constant  $\Delta x$  or  $\Delta y$  when reconstructing the  $\pi^0$  yield, and the decay width  $\Gamma(\pi^0)$  is recalculated based on this new yield. The  $\Delta x/\Delta y$  are varied from -10 mm to 10 mm with 1 mm step. Fig. 5.14 shows the change of the decay width over misalignment. According to the survey, the upper limit of the HYCAL misalignment is less than

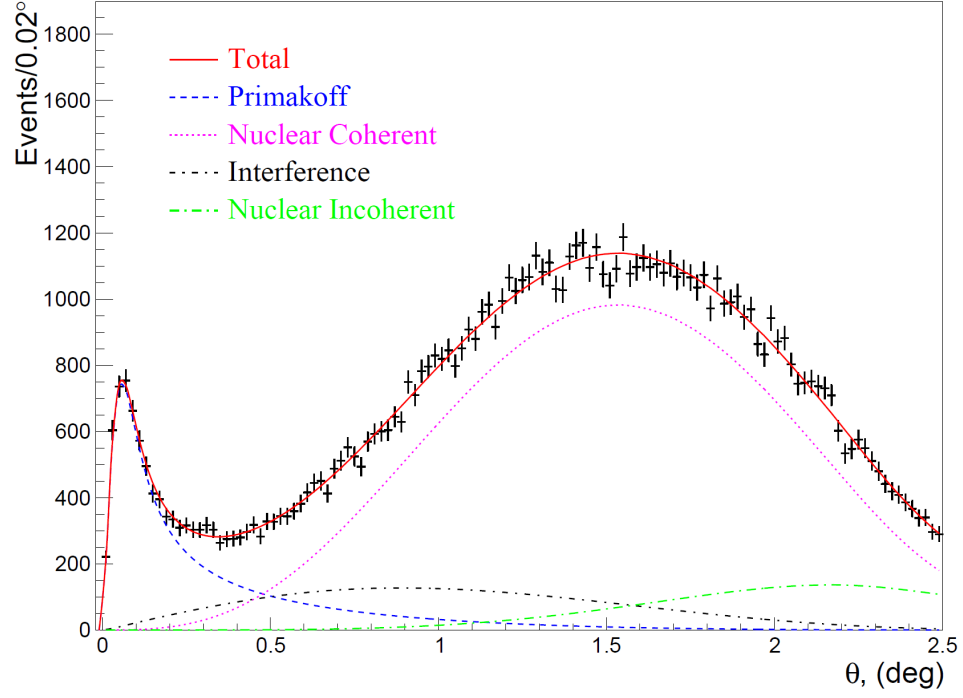


FIGURE 5.11:  $\pi^0$  yield extracted with  $0.02^\circ$  angular bin for carbon.

0.5 mm. Assuming the misalignment can vary between -2 mm to 2mm, the systematic uncertainties of decay width due to this variation can be calculated based on the curves shown in Fig. 5.14 and the results are listed in table 5.3. When there is a misalignment, the Primakoff peak of the  $\pi^0$  yield is shifted since the misalignment mainly affects the calculation of the  $\pi^0$  production angle. The fitting parameter of the  $\pi^0$  decay width is suppressed by the mismatch between the position of the reconstructed Primakoff peak and the theoretical peak position. The fact that the maximum value of the  $\pi^0$  decay width is around zero in Fig. 5.14 indicates a proper HYCAL alignment.

In summary, the systematic uncertainty due to the HYCAL misalignment in x is better than 0.29%, and in y is better than 0.31%.

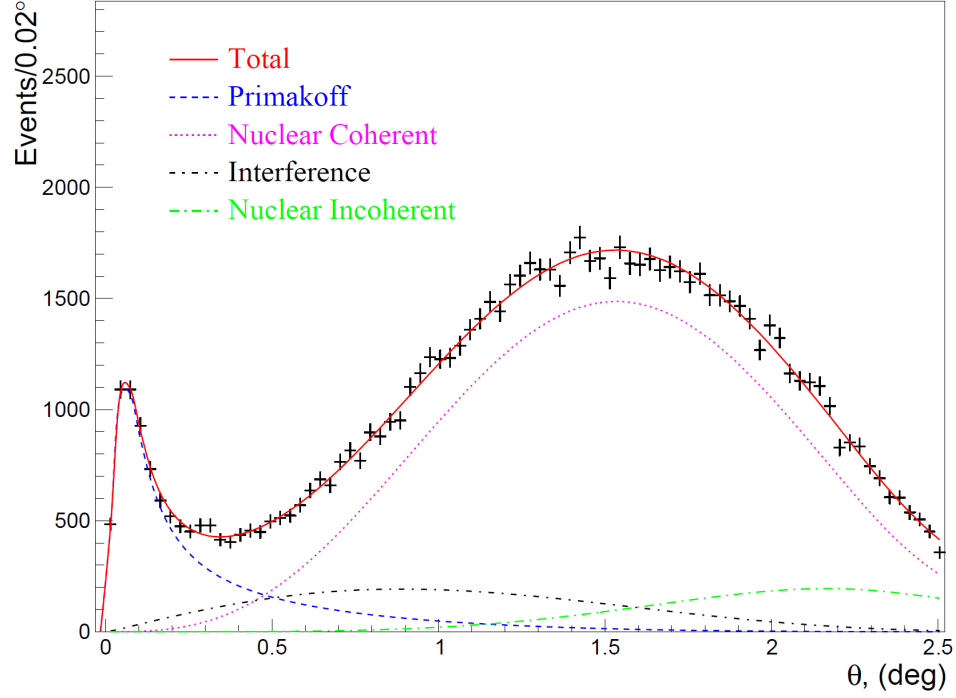


FIGURE 5.12:  $\pi^0$  yield extracted with  $0.03^\circ$  angular bin for carbon.

Table 5.3: Systematic uncertainties of  $\pi^0$  decay width due to HYCAL misalignment

| $\Delta x, \Delta y$ | $\Gamma(\pi^0)$ by $\Delta x$ (%) | $\Gamma(\pi^0)$ by $\Delta y$ (%) |
|----------------------|-----------------------------------|-----------------------------------|
| 2 mm                 | -0.29%                            | -0.26%                            |
| -2 mm                | -0.14%                            | -0.31%                            |

### 5.6.2 Decay Width Sensitivity to HYCAL $z$ Position

The distance  $z$  between the HYCAL and the target is provided by survey before the experiment, which is 702 cm for the silicon target and 701.2 cm for the carbon target. The systematic uncertainty of this measurement is 1 cm. In order to propagate this uncertainty into  $\pi^0$  decay width uncertainty budget, the relation between the decay width and the distance  $z$  must be studied.

In this section, the HYCAL  $z$  position is assumed to be a set of values from 697 cm to 706 cm with a step of 1 cm. The extracted  $\Gamma(\pi^0)$  is drawn as a function of  $z$  in

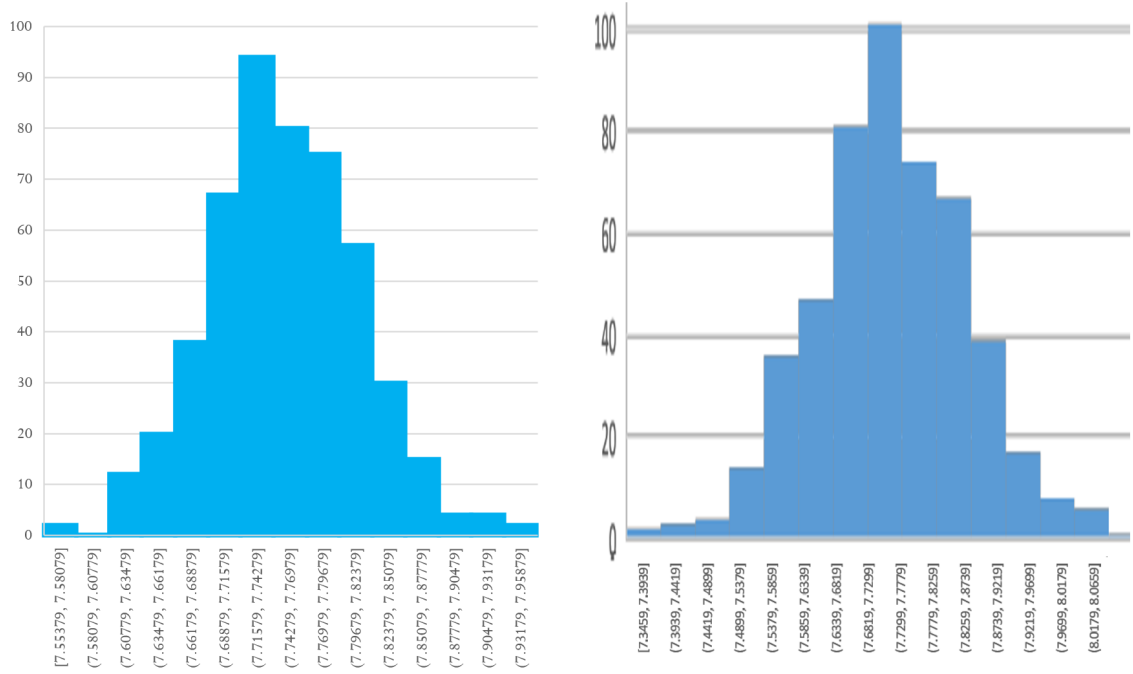


FIGURE 5.13: Left:  $\pi^0$  decay widths from silicon realistic M.C. Right:  $\pi^0$  decay widths from carbon realistic M.C.

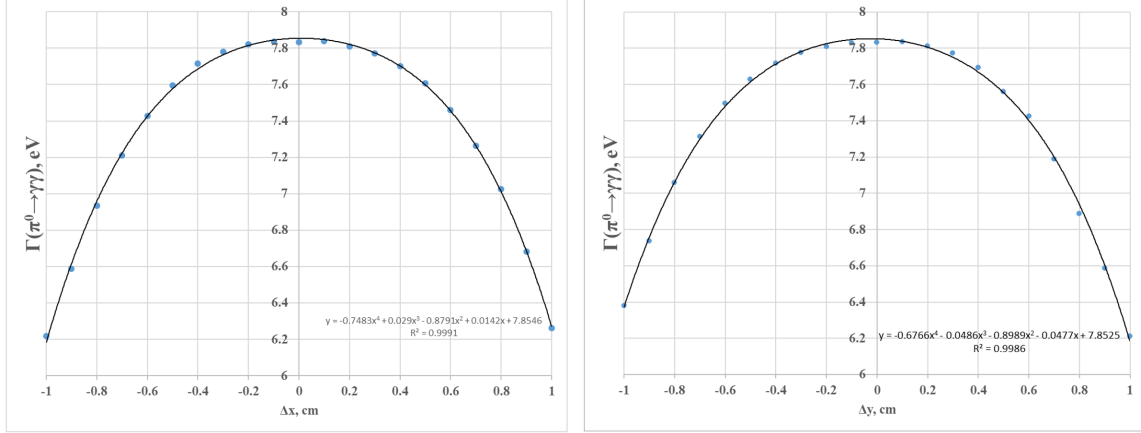


FIGURE 5.14: The  $\Gamma(\pi^0)$  is plotted as a function of HYCAL misalignment. The left plot shows the change in the decay width due to the HYCAL misalignment in  $x$ , and the right plot shows the change in  $y$ .

Fig. 5.15. Apparently the decay width changes linearly with respect to  $z$  with a fitted slope of -0.0037. As a result, the propagated systematic uncertainty is calculated to



be 0.047%.

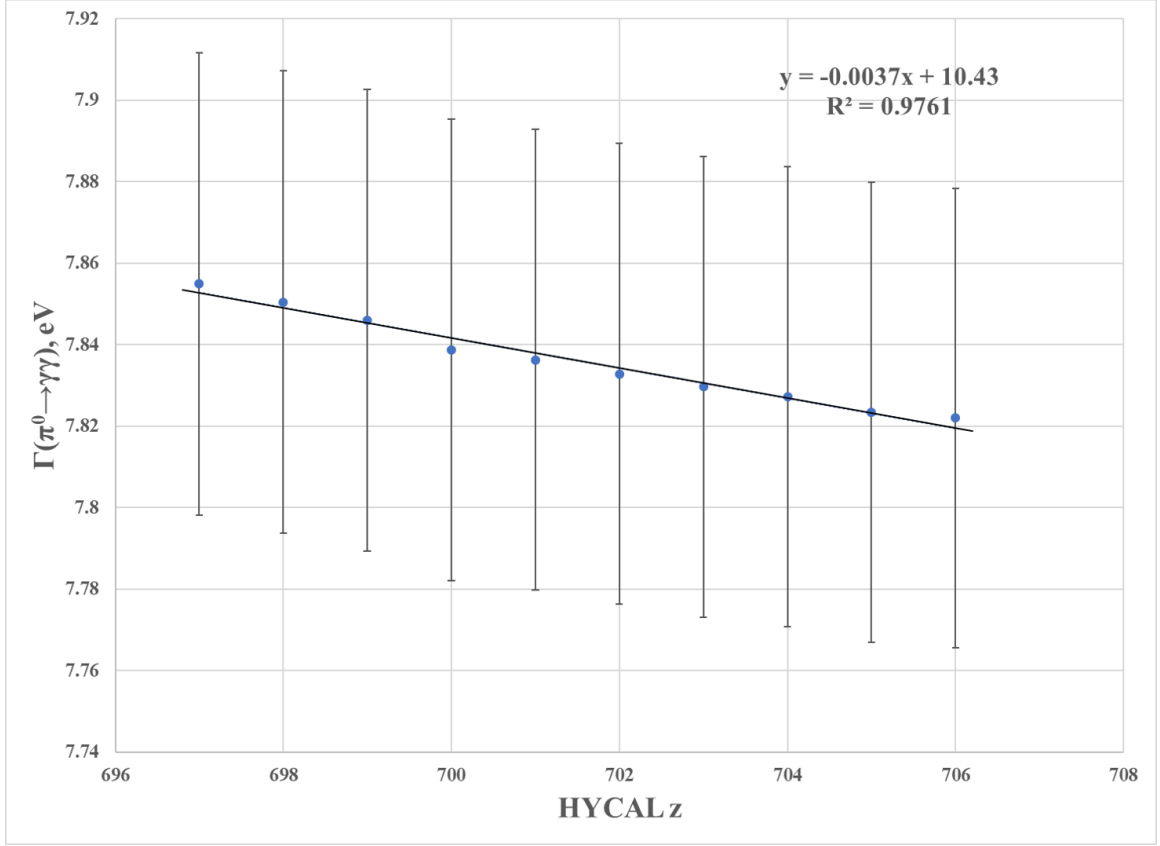


FIGURE 5.15: The  $\Gamma(\pi^0)$  as a function of the distance of HYCAL to the target center. The error bars shown in this figure are statistical uncertainties, and thus do not represent the variations studied in this section.

In summary, the total uncertainty from the HYCAL acceptance is 0.31%.

## 5.7 Systematic Uncertainties Due to Photon Beam

The uncertainties in the photon beam energy, the beam direction and the beam width will all be propagated into the final uncertainty. In this section, the calculation of these three terms are discussed.

### 5.7.1 Decay Width Sensitivity to the Photon Beam Energy

The systematic uncertainty of the photon beam energy is no worse than 0.13% [40]. An artificial shift of the beam energy by 0.5% results in a 1.05% change in the decay width. Therefore by interpolation the addition to the systematic uncertainty of the decay width due to the photon beam energy is 0.273%.

### 5.7.2 Decay Width Sensitivity to the Beam Width

The decay width sensitivity to the beam width is based on the PrimEx-I result and estimated to be 0.2%.

### 5.7.3 Decay Width Sensitivity to Beam Direction

Another type of HYCAL misalignment arises from the photon beam forming a small angle with the  $z$  axis, which affects the accuracy of the  $\pi^0$  production angle  $\theta$ . In order to study this effect, the  $\pi^0$  production angle  $\theta$  is projected onto  $\theta_x$  and  $\theta_y$  as described in equation 4.12. For example if the beam direction is systematically shifted by  $\Delta\theta_x$ , the projection of real production angle will be  $\theta_x + \Delta\theta_x$ . In the analysis the  $\Delta\theta_{x,y}$  are varied from -1 mrad to 1 mrad with a step of 0.1 mrad. The range of the variation corresponds to about 1 cm change in the HYCAL coordinates. The extracted  $\Gamma(\pi^0)$  is drawn as a function of  $\Delta\theta_{x,y}$  in Fig. 5.16. The maximum value of  $\Gamma(\pi^0)$  is around zero, indicating the beam direction shift during the experiment is negligible.

The upper limit of beam direction uncertainty is 0.1 mrad, which is consistent with the misalignment estimation of 0.5 mm. The systematic uncertainties due to the beam direction are summarised in table 5.4:

In summary, the total systematic uncertainty related to the photon beam parameters (energy, position and direction) is 0.35%.

Table 5.4: Systematic uncertainties of  $\pi^0$  decay width due to the uncertainty of the beam direction

| $\Delta\theta_x, \Delta\theta_y$ | $\Gamma(\pi^0)$ by $\Delta\theta_x$ (%) | $\Gamma(\pi^0)$ by $\Delta\theta_y$ (%) |
|----------------------------------|-----------------------------------------|-----------------------------------------|
| 0.1 mrad                         | -0.05%                                  | -0.003%                                 |
| -0.1 mrad                        | -0.006%                                 | 0.09%                                   |

## 5.8 Different Nuclear Density Models

The nuclear charge density distributions are used in the calculation of the  $\pi^0$  photo-production cross section. For many nuclei, the charge densities are readily available from electron scattering experiments [39]. Usually there are a few different types of models for each nucleus based on the same or a few different experiments. For  $^{28}\text{Si}$  ( $\sim 92\%$  abundance) and  $^{12}\text{C}$ , there are 2-parameter and 3-parameter Fermi models and Fourier-Bessel model. The 3-parameter Fermi model is able to capture more features of the charge density than the 2-parameter Fermi model. All these models are fitted from previous electron scattering experiments. The quoted uncertainties on the model parameters are about 1% for the  $^{28}\text{Si}$  models, and less than 0.5% for the  $^{12}\text{C}$  models. In this data analysis we tried two charge density models in the form factor calculation for both targets: (1) 3-parameter Fermi model; (2) Fourier-Bessel model.

The 3-parameter Fermi model takes the form of:

$$\rho(r) = \frac{\rho_0(1 + \frac{wr^2}{c^2})}{1 + \exp(\frac{r-c}{z})}, \quad (5.2)$$

where  $c$  is the radius of the target nucleus, and the normalization factor  $\rho_0$  takes the value so that the integrated charge distribution equals the nuclear charge  $Ze$ . We found for silicon target, in order to fit PrimEx-II data well, the silicon nuclear radius has to be increased by 7% compared to the value given by electron scattering experiment. Fig. 5.17 shows how silicon radius affect the fitting of the  $\pi^0$  photoproduction yields, the goodness of the fitting is represented by the value of  $\chi^2/NDF$ .

The silicon radius has a big effect on the yield fitting. There are two issues with the fitting here: (1) the best achieved  $\chi^2/NDF$  is  $\sim 1.1$ , while ideally this value is about 1 for a perfect fit and, (2) the 3-parameter Fermi model is quoted with 1% uncertainty, however we need to increase the radius by 7% in order to achieve the best fitting with the PrimEx-II data.

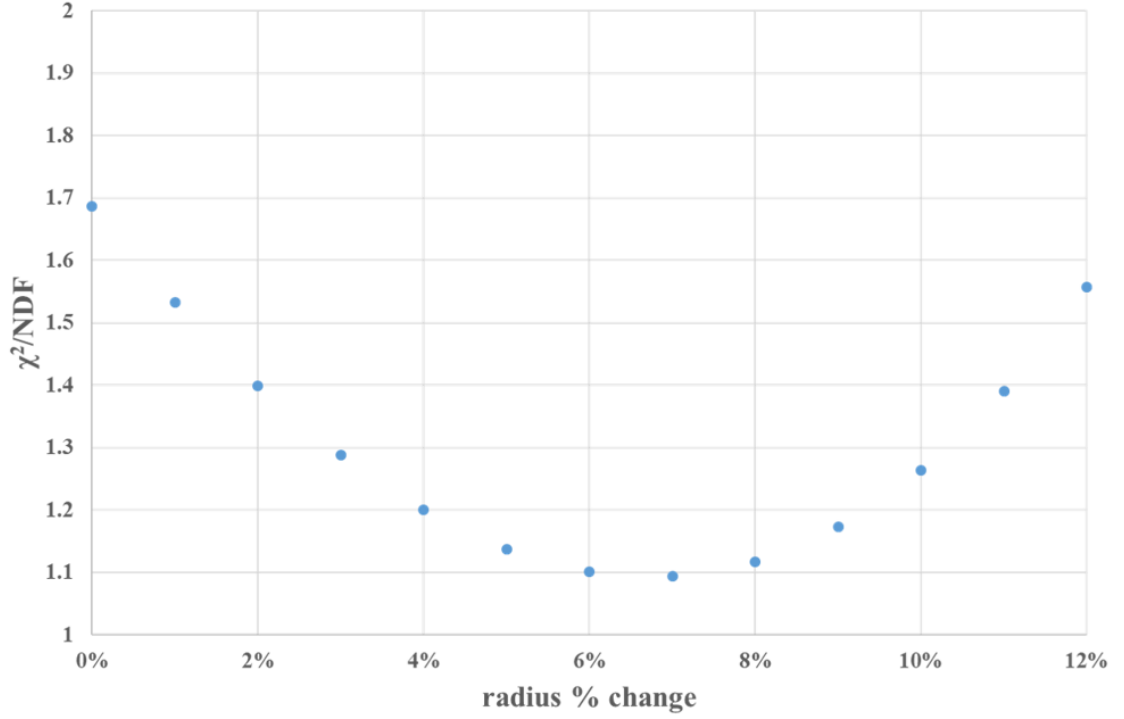


FIGURE 5.17: Goodness of fits and the decay width's using 3-parameter Fermi nuclear density model. The  $x$  axis shows the percentage change to the quoted  $^{28}\text{Si}$  nucleus radius. The best fit to the PrimEx-II data is achieved when the silicon radius is increased by about 7%.

The Fourier-Bessel model takes the form of [39]:

$$\rho(r) = \begin{cases} \sum_v a_v j_0\left(\frac{v\pi r}{R}\right) & \text{for } r \leq R \\ 0 & \text{for } r \geq R, \end{cases} \quad (5.3)$$

where  $R$  is the cutoff radius, and  $j_0(qr)$  denotes the Bessel function of order zero.

Both the radius  $R$  and the coefficients  $a_v$  are obtained from electron scattering experiments. In order to obtain the best yield fitting, we adjusted the  $R$  value in the analysis. The resulted fittings are shown in Fig. 5.18. For silicon the  $R$  value is increased by 2% when the best fitting is achieved. And the  $\chi^2/NDF$  is about 1. In conclusion, the Fourier-Bessel model is a superior model and better suited in precision measurements such as PrimEx-II.

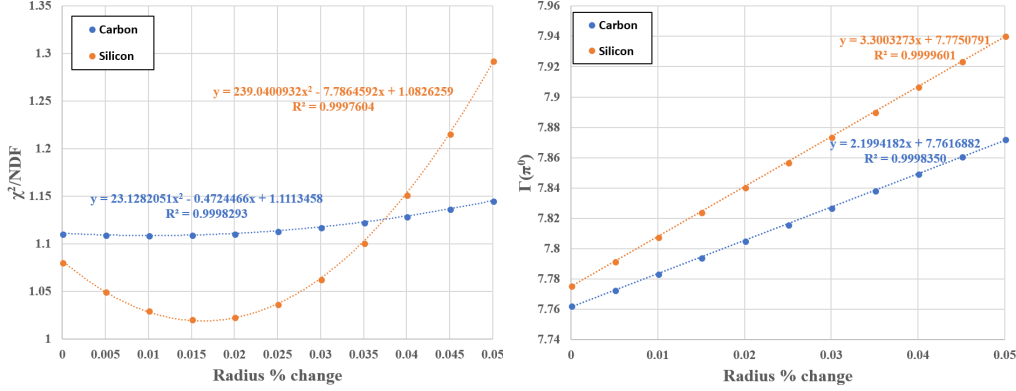


FIGURE 5.18: Goodness of fits and the decay width's using Fermi-Bessel nuclear density model. The  $x$  axis shows the percentage change to the quoted  $^{28}\text{Si}$  nucleus radius. The best fit to the PrimEx-II data is achieved when the silicon radius is increased by about 2% and when the carbon radius is increased by about 1%.

By systematic uncertainties of the decay width due to the uncertainties in the atomic radii can be determined using Fig. 5.18. Adding to the minimum  $\chi^2$  by 1, the silicon radius falls between 1.04% to 2.22% of the quoted silicon radius, and the carbon radius is between -0.869% to 2.91% of the quoted carbon radius. As a result, the systematic uncertainty of  $\pi^0$  decay width measured from the silicon target is 0.248%, while from carbon target is 0.534%.

Table 5.5: Uncertainties of  $\pi^0$  decay width.

| Item                           |                              | Silicon (%) | Carbon (%) | Common (%) | Ref.     |
|--------------------------------|------------------------------|-------------|------------|------------|----------|
| Stat. Uncertainties            |                              | 0.77        | 1.54       |            |          |
| Branching Ratio                |                              |             |            | 0.03       | [7]      |
| Photon Beam Flux               |                              |             |            | 0.83       | [25, 26] |
| Target Measurement             |                              | 0.35        | 0.02       |            | [24]     |
| Target Absorption              |                              | 0.2         | 0.2        |            |          |
| Trigger Efficiency             |                              |             |            | 0.1        |          |
| HYCAL Acceptance               |                              |             |            | 0.31       |          |
| HYCAL Energy Response Function |                              |             |            | 0.45       | [41]     |
| Beam Parameters                |                              |             |            | 0.38       |          |
| Yield Extraction               | Single $\gamma$ Energy Cut   |             |            | 0.04       |          |
|                                | $\pi^0$ Energy Cut           |             |            | 0.06       |          |
|                                | Tdiff Cut                    |             |            | 0.03       |          |
|                                | Best Tdiff Selection         | 0.1         | 0.2        |            |          |
|                                | Signal Background Separation | 0.757       | 1.015      |            |          |
|                                | $\pi^0$ yield binning        | 0.05        | 0.1        |            |          |
|                                | realistic M.C.               | 0.65        | 0.65       |            |          |
|                                | Total (Yield Extraction)     | 1.01        | 1.23       |            |          |
| $\omega$ background            |                              | 0.14        | 0.16       |            |          |
| Model Errors (theory)          |                              | 0.25        | 0.53       | 0.30       |          |
| Syst. Uncertainties            |                              | 1.58        | 1.76       |            |          |
| Total (stat. & syst.)          |                              | 1.76        | 2.34       |            |          |

## 5.9 Systematic Uncertainties

A summary of the systematic uncertainties for both the silicon and carbon targets are listed in table 5.5. The systematic uncertainties for the photon flux is preliminary and based on PrimEx-I estimations. Further study is needed on the relative tagging ratio.

### 5.10 $\pi^0$ Decay Width

The results for the  $\pi^0$  decay width from both silicon and carbon targets are listed in table 5.6. The total uncertainty for silicon is 1.76%, and for carbon is 2.34%. The  $\pi^0$  decay width combined for the two targets is  $7.821 \pm 0.054(stat.) \pm 0.124(syst.)$ . The total uncertainty is 0.135 eV, or 1.7%, which is a significant improvement from the 2.8% total uncertainty from the PrimEx-I experiment. The result is almost final except for the systematic uncertainty from photon beam flux. Fig. ?? the  $\pi^0$  decay

Table 5.6:  $\pi^0$  decay width obtained from silicon and carbon targets

| Target          | $\Gamma_{\gamma\gamma}$ (eV)              |
|-----------------|-------------------------------------------|
| Silicon         | $7.831 \pm 0.060(stat.) \pm 0.124(syst.)$ |
| $^{12}\text{C}$ | $7.783 \pm 0.120(stat.) \pm 0.137(syst.)$ |
| combined        | $7.821 \pm 0.054(stat.) \pm 0.124(syst.)$ |

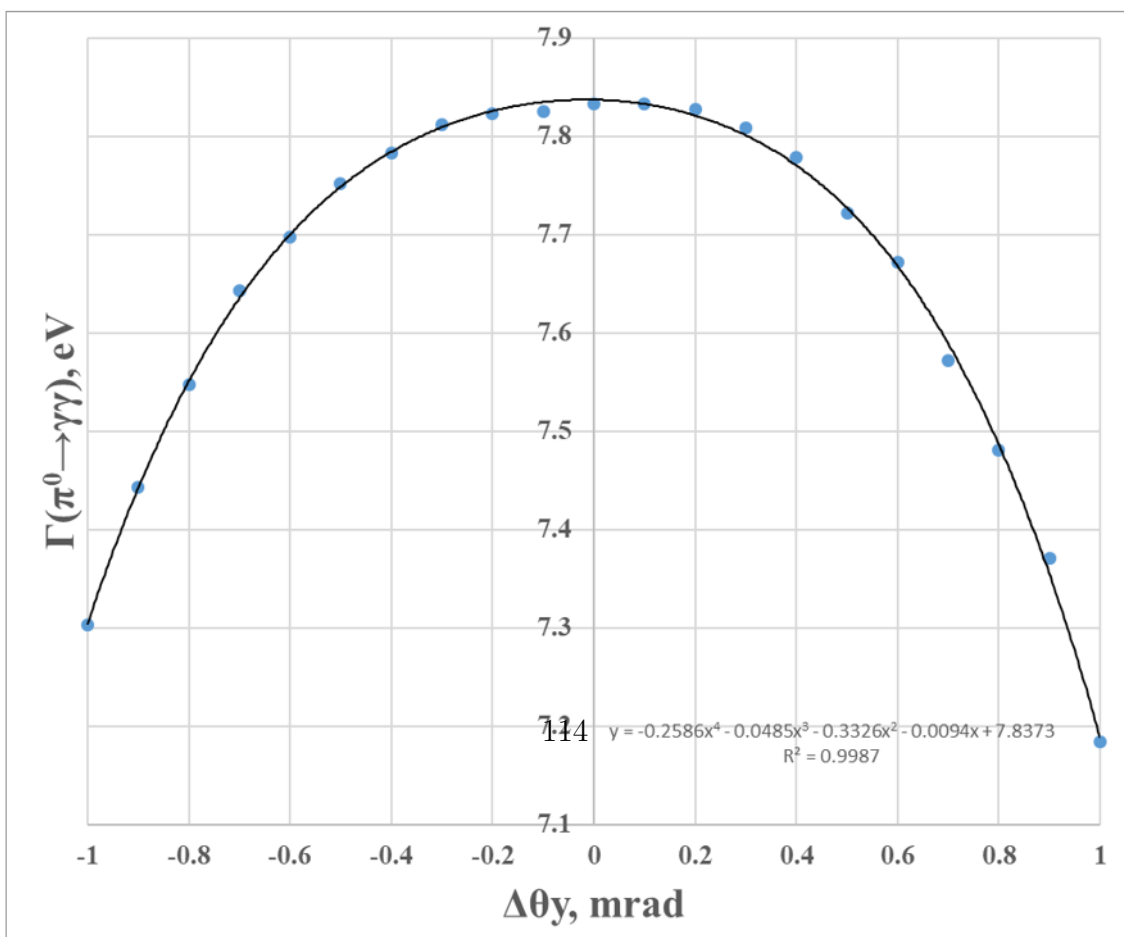
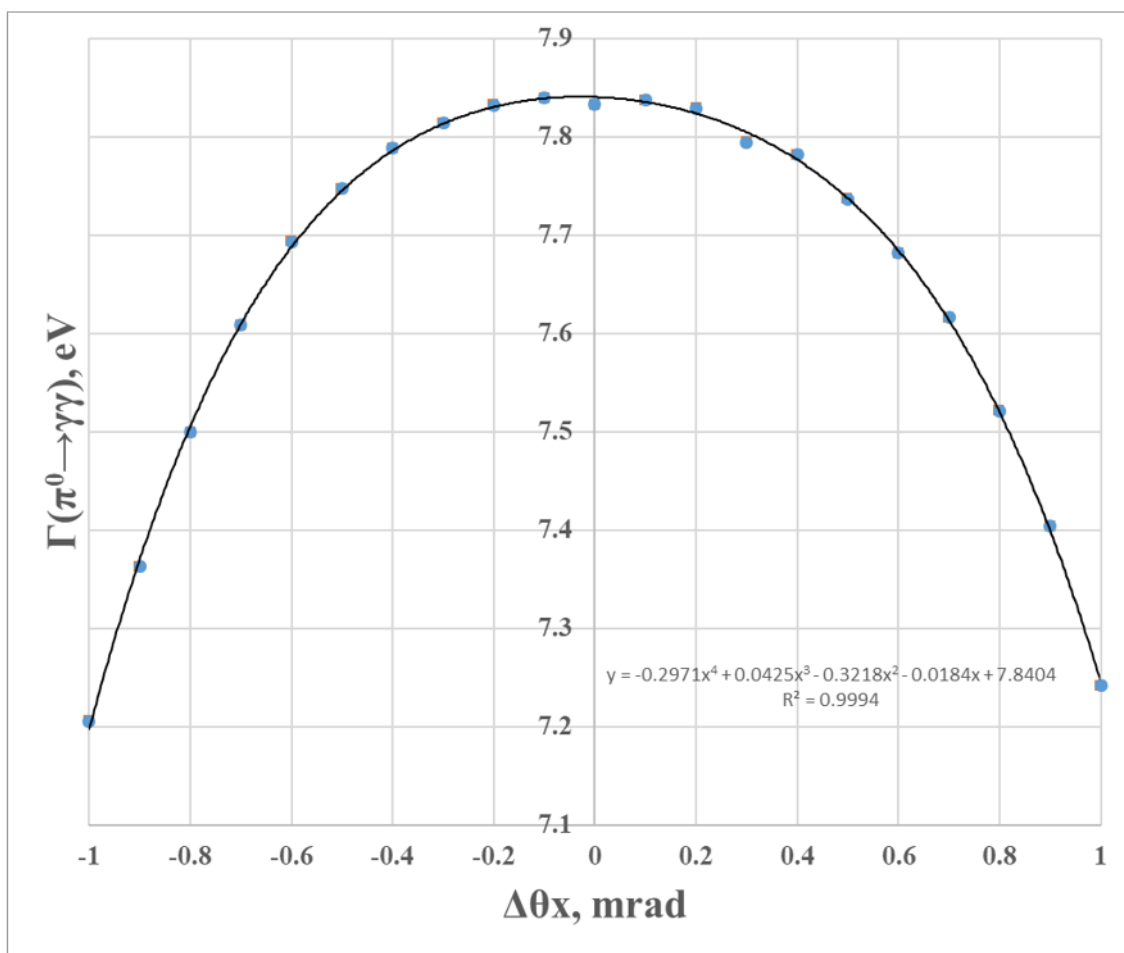
width from PrimEx-II and four other measurements [6, 8, 9, 4] from experiments included in the PDG [7]. The chiral anomaly prediction, the sum rule result [15] and ChPT predictions [2, 1, 3] are also plotted. The PrimEx-II result lies within  $0.8 \sigma$  above the chiral anomaly prediction, one  $\sigma$  below the sum rule prediction, and  $1.8 \sigma$  below the ChPT calculations. It is in better agreement with the chiral anomaly prediction.

## 5.11 Summary and Outlook

The PrimEx-II experiment successfully measured the  $\pi^0$  decay width with less than 2% precision, which is the most precise measurement up to date. In this dissertation, the details of the experiment, the data analysis process and the results are presented.

The systematic uncertainty study is ongoing and soon to be finalized. Another data analysis for the Compton process using the dedicated Compton runs during the PrimEx-II experiment is close to being finished, the uncertainty of which is expected to be around 1.5%. The Compton scattering is used to validate the systematic uncertainty of the  $\pi^0$  decay width since the cross section is well understood.

Though suffering from poor resolution, the lead glass detectors provide a much better acceptance for the nuclear incoherent process. Further studies including this part of the HYCAL can provide a better understanding of how the nuclear incoherent background affects this measurement.





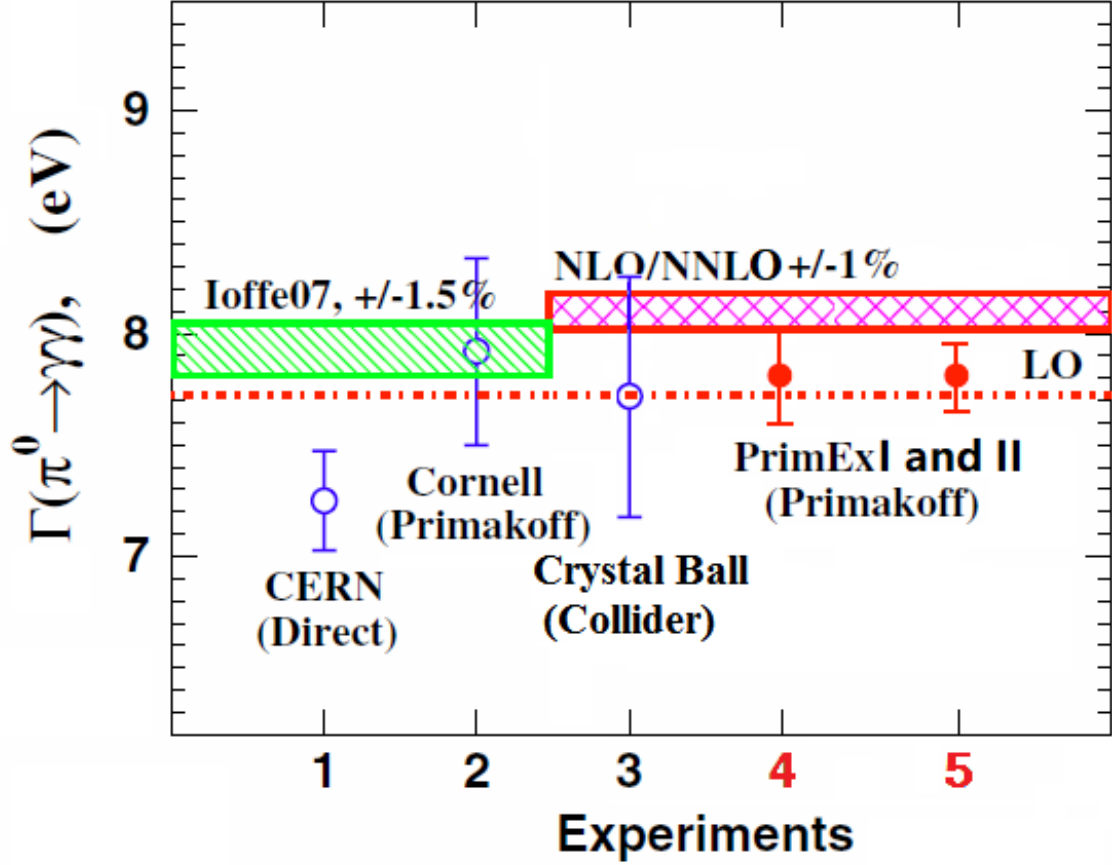


FIGURE 5.19: The experimental measurements and theoretical predictions of the  $\pi^0$  decay width. The PrimEx-II result (5) is plotted with four other experimental measurements: (1) CERN direct measurement [6]; (2) Cornell Primakoff measurement [8]; (3) Crystal Ball collider measurement [9] and (4) PrimEx-I result [4]. Except for the PrimEx-II result, all the other four experimental results are included in the current PDG value [7]. Another experiment that is in the PDG, the pion weak form factor experiment [10], is not included in this figure due to its large uncertainties in the measurement of the  $\pi^0$  decay width. The red dash line shows the chiral anomaly prediction. The green band demonstrate the sum rule calculation [15] and the red band demonstrates three ChPT NLO and NNLO calculations [2, 1, 3]. The PrimEx-II result lies within  $0.8 \sigma$  above the chiral anomaly prediction, one  $\sigma$  below the sum rule prediction, and  $1.8 \sigma$  below the ChPT calculations. It is in better agreement with the chiral anomaly prediction.

# Bibliography

- [1] B. Ananthanarayan and B. Moussallam. Electromagnetic corrections in the anomaly sector. *JHEP*, 05:052, 2002.
- [2] J.L. Goity.  $\pi^0 \rightarrow \gamma\gamma$  to NLO in ChPT. pages 611–614, 2002.
- [3] Karol Kampf and Bachir Moussallam. Chiral expansions of the  $\pi^0$  lifetime. *Phys. Rev. D*, 79:076005, Apr 2009.
- [4] I. Larin et al. A New Measurement of the  $\pi^0$  Radiative Decay Width. *Phys.Rev.Lett.*, 106:162303, 2011.
- [5] Claude Amsler et al. Review of Particle Physics. *Phys. Lett.*, B667:1–1340, 2008.
- [6] H.W. Atherton, C. Bovet, P. Coet, R. Desalvo, N. Doble, et al. DIRECT MEASUREMENT OF THE LIFETIME OF THE NEUTRAL PION. *Phys.Lett.*, B158:81–84, 1985.
- [7] C. Patrignani et al. Review of Particle Physics. *Chin. Phys.*, C40(10):100001, 2016.
- [8] A. Browman, J. DeWire, B. Gittelman, K. M. Hanson, D. Larson, E. Loh, and R. Lewis. The Decay Width of the Neutral pi Meson. *Phys. Rev. Lett.*, 33:1400, 1974.
- [9] D. Williams et al. FORMATION OF THE PSEUDOSCALARS  $\pi^0$ ,  $\eta$  AND  $\eta'$  IN THE REACTION  $\gamma\gamma \rightarrow \gamma\gamma$ . *Phys.Rev.*, D38:1365, 1988.
- [10] M. Bychkov et al. New Precise Measurement of the Pion Weak Form Factors in  $\pi^+ \rightarrow e^+ \nu \gamma$  Decay. *Phys. Rev. Lett.*, 103:051802, 2009.
- [11] A. Zee. *Quantum field theory in a nutshell*. 2003.

- [12] Stephen L. Adler. Axial vector vertex in spinor electrodynamics. *Phys.Rev.*, 177:2426–2438, 1969.
- [13] J.S. Bell and R. Jackiw. A PCAC puzzle:  $\pi^0 \rightarrow \gamma\gamma$  in the sigma model. *Nuovo Cim.*, A60:47–61, 1969.
- [14] G. Bellettini, C. Bemporad, P.L. Braccini, C. Bradaschia, L. Foa, et al. A new measurement of the  $\pi^0$  lifetime through the primakoff effect in nuclei. *Nuovo Cim.*, A66:243–252, 1970.
- [15] B.L. Ioffe and A.G. Oganesian. Axial anomaly and the precise value of the  $\pi^0 \rightarrow \gamma\gamma$  decay width. *Phys.Lett.*, B647:389–393, 2007.
- [16] H. Primakoff. Photoproduction of neutral mesons in nuclear electric fields and the mean life of the neutral meson. *Phys. Rev.*, 81:899, 1951.
- [17] G. Bellettini, C. Bemporad, P. L. Braccini, and L. Foà. Primakoff effect and  $\pi^0$  lifetime. *Il Nuovo Cimento A (1965-1970)*, 40(4):1139–1170, Dec 1965.
- [18] V.I. Kryshkin, A.G. Sterligov, and Yu.P. Usov. Measurement of lifetime of the  $\pi^0$  meson. *Zh.Eksp.Teor.Fiz.*, 57:1917–1922, 1969.
- [19] G. Von Dardel, D. Dekkers, R. Mermoud, J. D. Van Putten, M. Vivargent, G. Weber, and K. Winter. Mean life of the neutral pion. *Physics Letters*, 4:51–54, March 1963.
- [20] et al. J. Beringer. Review of particle physics. *Phys. Rev. D*, 86:010001, Jul 2012.
- [21] Jefferson Lab. 12 gev upgrade. 2016.
- [22] D. I. Sober et al. The bremsstrahlung tagged photon beam in Hall B at JLab. *Nucl. Instrum. Meth.*, A440:263–284, 2000.
- [23] R. Miskimen et al. Silicon Target used in PRIMEX II. *Tech Note, PrimEx-II, Jefferson Lab*, 2012.
- [24] R. Miskimen et al. Thickness and Density Measurements for the Graphite Target Used in PRIMEX II. *Tech Note, PrimEx-II, Jefferson Lab*, 2013.
- [25] Ilya Larin. Analysis of PrimEx-2 normalization (TAC) runs. *Tech Note, PrimEx-II, Jefferson Lab*, 2013.

- [26] Aram Teymurazyan. Photon Flux Determination for a Precision Measurement of the Neutral Pion Lifetime. *Phd dissertation, University of Kentucky*, 2008.
- [27] A. Gasparian et al. A Precision Measurement of the Neutral Pion Lifetime via the Primakoff Effect. *Proposal, Jefferson Lab*, 2002.
- [28] Victor Tarasov. Beam Quality Check with EPICS data analysis. *Tech Note, PrimEx-II, Jefferson Lab*, 2013.
- [29] Ilya Larin. PrimEx-II Log Book. *PrimEx Note*, 2010.
- [30] Lingling Ma. Tagger TDC alignment for PrimEx-II. *PrimEx Note*, 2012.
- [31] Ilya Larin. HyCal reconstruction updates for PrimEx II. *PrimEx Note*, 2012.
- [32] Victor Tarasov. HyCal Calibration Check. *PrimEx Note*, 2013.
- [33] Lingling Ma. Check Hycal position alignment. *Tech Note, PrimEx-II, Jefferson Lab*, 2014.
- [34] Ilya Larin, A. Gasparan, L. Gan, and S. Gevorkyan. PrimEx-II Log Book. *PrimEx Note*, 2010.
- [35] Ilya Larin. PrimEx-II Log Book. *PrimEx Note*, 2010.
- [36] C. A. Engelbrecht. Photoproduction of Neutral Pions from Complex Nuclei. *Phys. Rev.*, 133:B988–B1006, 1964.
- [37] R. Brun, R. Hagelberg, M. Hansroul, and J. C. Lassalle. Geant: Simulation Program for Particle Physics Experiments. User Guide and Reference Manual. 1978.
- [38] R. Brun, F. Rademakers, and S. Panacek. ROOT, an object oriented data analysis framework. *Conf. Proc.*, C000917:11–42, 2000.
- [39] H. De Vries, C. W. De Jager, and C. De Vries. Nuclear charge and magnetization density distribution parameters from elastic electron scattering. *Atom. Data Nucl. Data Tabl.*, 36:495–536, 1987.
- [40] S. Stepanyan et al. Energy calibration of the JLab bremsstrahlung tagging system. *Nucl. Instrum. Meth.*, A572:654–661, 2007.
- [41] Ilya Larin. Report on PrimEx Analysis Meeting, June 2007. *Tech Note, PrimEx-I, Jefferson Lab*, 2013.

# Biography

Yang Zhang was born in Nanyang, Henan province, China on Sep 20th, 1984. He attended University of Science and Technology of China in 2004, and graduated in 2008 with a B.S. in Physics. He attended University of Missouri, Kansas City in 2008 and graduated with a M.S. in Physics in 2010. In the summer of the same year, He began the graduate studies at Duke University and worked with Professor Haiyan Gao. He has made essential contributions to three papers and published several other papers as a collaborator.